Strål
säkerhets
myndigheten

Author: Joel Geier

Research

2011:13

Investigation of Discrete-Fracture Network Conceptual Model Uncertainty at Forsmark

SSM perspective

Background
Groundwater flow plays an important role for the safety of a final repository for spent nuclear fuel, such as the one presented by the Swedish Nuclear Fuel and Waste Management Company's (SKB). Ground water flow affects the barriers and potential radionuclide transport through the geosphere. Canister corrosion is for example related to the solute transport by groundwater to the repository. The risk of buffer erosion is connected to the flow of dilute groundwater from melting glaciers to repository depth, and radionuclides leaking from a failed canister are carried to the biosphere by the groundwater.

Objectives
In the present work a discrete fracture model has been further developed and implemented using the latest SKB site investigation data. The model can be used for analysing the fracture network and to model flow through the rock in Forsmark. The aim has been to study uncertainties in the hydrological discrete fracture network (DFN) for the repository model. More specifically the objective has been to study to which extent available data limits uncertainties in the DFN model and how data that can be obtained in future underground work can further limit these uncertainties. Moreover, the effects on deposition hole utilisation and placement have been investigated as well as the effects on the flow to deposition holes.

Results
Flow modelling using alternative assumptions regarding conceptual and parametric uncertainty in the spatial and structural relationships among fractures indicates elevated flow rates and groundwater velocities to deposition holes compared to SKB's flow modelling results. Simulated sampling of fractures in boreholes does not indicate any reason to exclude the proposed spatial and structural relationships among fractures. The number of deposition holes that need to be discarded due to intersections with fractures, according to rules proposed by SKB, are not significantly affected by the studied alternative assumptions. Simulated fracture sampling along tunnels in the proposed repository layout for the Forsmark site indicates that future underground data should be sufficient to distinguish between SKB's assumptions and the alternative ones made in this work. Whether or not the differences between different assumed spatial and structural relationships are robust with respect to non-ideal sampling situations underground is an open question.

Project information
Contact person SSM: Georg Lindgren
Reference: SSM 2010/465

Strål säkerhets myndigheten
Swedish Radiation Safety Authority

Author: Joel Geier, Clearwater Hardrock Consulting

2011:13

Investigation of Discrete-Fracture Network Conceptual Model Uncertainty at Forsmark

Content

1. Introduction

Background

The discrete-fracture network (DFN) model for the repository volume is critical for predicting flows to deposition holes (affecting geochemical stability for the buffer), risk of mechanical damage to canisters, and radionuclide transport in the near field. Key categories of uncertainty in the DFN model include:

- Parametric uncertainty in the fracture size distribution;
- Parametric uncertainty in the correlation of fracture transmissivity to fracture size;
- Conceptual and parametric uncertainty in the spatial and structural relationships among fractures.

The first two categories are recognized by SKB as being among the most significant uncertainties in the site descriptive model for Forsmark. The third category, which includes issues such as clustering, variability of fracture intensity, and correlation of fracture intensity to the larger fractures or deformation zones, has thus far not been fully recognized by SKB.

To some extent all of these uncertainties can be reduced in the repository construction stage, by use of the additional information that will come from mapping of fractures along the repository access shaft and tunnels. However, review of the license application will require a more thorough scoping of the consequences of all of these categories of uncertainties in the DFN model, than can be expected in SKB's submission.

Scope

The principal research questions addressed in this report are:

- To what extent do data obtained in surface-based site investigations limit parametric and conceptual uncertainties with regard to DFN size distributions, size-transmissivity relationships, and spatial/structural relationships among fractures, for the rock at repository depth?
- To what extent can data obtained in the repository construction phase reasonably be expected to limit these same uncertainties?
- For each of these two stages, what are realistic bounds on the consequences in terms of (a) deposition-hole utilization factors in a KBS-3V type repository, (b) likelihood of placing a canister in a hole that is intersected by an undetected, discriminating feature that poses a risk of shear failure, and (c) likelihood of flows to a deposition hole that exceed some value that could jeopardize engineered barrier performance.
- How do viable alternative DFN models compare with the DFN model used in SKB's site descriptive model in terms of flows to canister positions in a

given section of the proposed repository, and transport paths from those same positions?

As part of this project, a simplified version of SKB's Site Descriptive Model for SDM-Site was implemented. Key simplifications included reduced resolution of the geometry of the large-scale deformation zones and topographic surface, along with a reduction in the number of canister positions that are represented explicitly in the repository component of the model.

Approach

The research questions outlined above are addressed by the following steps:

- Implement a simplified version of SKB's SDM-Site model for comparison to alternative DFN conceptual models, with simplified representation of deformation zones and including deposition holes in just one section of repository. Initiate flow simulations using this model.
- Identify a set of alternative DFN conceptual models that could fit the available data from surface-based site characterization at Forsmark, but which have different properties that can be quantified in terms of termination relationships and spatial/structural correlations among fractures.
- Use simulated sampling in boreholes and steady-state flow simulations of flows to boreholes to evaluate the ability of surface-based site investigations at Forsmark to discriminate among these models.
- For a range of DFN models that are found to be viable with respect to surface-based investigations at Forsmark to date (including SKB's model), evaluate utilization percentages and probability of a canister intersecting an unidentified "discriminating" fracture (critical size fracture with >75 m radius), in a KBS-3 repository that utilizes SKB's proposed emplacement criteria.
- Complete flow simulations based on simplified version of SDM-Site model (with SKB's DFN conceptual model) and initiate particle-tracking simulation of transport.
- Use simulated sampling along tunnels based on SKB's most recently proposed repository layout to evaluate the likelihood of being able to discriminate among viable alternative DFN models during the construction phase.
- For the same range of viable models, evaluate the distribution of flows to deposition holes and compare flow and transport to simplified implementation of SKB model.

2. Data Sources

The primary data used in this analysis are taken from:

1) Extended single-hole interpretations
Data Delivery skb#09_04 (0:10)
Date: 2009-06-12
Delivered by: Veronika Linde
Delivered to: Sven Tirén, Geosigma AB
Description: Modeling p_eshi
Preliminary processing of the data consisted of converting Excel spreadsheets to pipe-separated CSV format (by hand for each file, using OpenOffice.org 3.1.1).

2) Fracture frequency data from boreholes
Data Delivery skb#09_04 (0:4)
Date: 2009-06-09
Delivered by: Veronika Linde
Delivered to: Sven Tirén, Geosigma AB
Description: Fracture data p_fract_core
Preliminary processing of the data consisted of converting Excel spreadsheets to pipe-separated CSV format (by hand for each file, using OpenOffice.org 3.1.1).

3) Fracture domain boundaries
For preliminary analysis described in Chapter 3:
Taken from Table 5-2 and estimated from Appendix 4 of Olofsson et al. (2007).
For subsequent analyses:
Data Delivery skb#09_04 (0:4)
Date: 2009-06-09
Delivered by: Veronika Linde
Delivered to: Sven Tirén, Geosigma AB
Description: FD_PFM_v22.01 basemodel_joel (file translated by Geosigma, subsequently converted to DFM panel file as described in Geier, 2010a).

4) Deformation zone geometry (double-sided)
Data Delivery skb#09_04 (0:4)
Date: 2009-06-09
Delivered by: Veronika Linde
Delivered to: Sven Tirén, Geosigma AB
Description: DZ_PFM_REG_v22.02 basemod_joel.dxf (file translated by Geosigma, then converted to DFM panel file as described in Geier, 2010a).

5) Deformation zone geometry (single-sided)
Data delivery May 2010.
Delivered to: Sven Tirén, Geosigma AB

Description: DZ_PFM_Loc_v22_01. without boundary.dxf and
DZ_PFM_REG_v22.02 without boundary.dxf (files translated by Geosigma,
then converted to DFM panel file as described in Geier, 2010a).

6) Borehole geometry
Data Delivery skb#09_04 (0:4)
Date: 2009-06-09
Delivered by: Veronika Linde
Delivered to: Sven Tirén, Geosigma AB
Description: Forsmark-BH-090610.dxf
(converted to DFM panel file using script BaseData/Boreholes/parsebhs).

7) Repository layout
Date: 2010-06-02 16:27
Delivered by: Stefan Sehlstedt
Delivered to: Sven Tirén, Geosigma AB
Description: Layout for the repository at Forsmark.

3. Exploratory identification of alternatives

This chapter describes an exploratory analysis to identify alternative conceptual models for the fracture system at the Forsmark candidate repository site. The objective was to determine whether the fractures might be spatially organized in ways that are not taken into account by SKB's conceptual model for the discrete-fracture network (DFN) portion of the SDM-Site site descriptive model (Fox et al., 2007; SKB 2008), and if so, to identify a set of alternative models that can be propagated as variants in DFM analysis.

This analysis is based on fracture data from core-drilled holes at the Forsmark site. Additional data from outcrop mapping were delivered by SKB midway through this project, and could be used as a further means to test the alternative models and calibrate their parameters, though this has not been done so far. The aim at this stage of the analysis was to identify possible alternative models, rather than to demonstrate that these are necessarily better models than those developed by SKB.

Background

In their statistical analysis of fractures in the bedrock at Forsmark, Fox et al. (2007, p. 174-181) found significant differences between portions of the rock that were recognized to be "affected by deformation zones," by which was meant the major deformation zones that are generally longer than 1 km. Fractures in these "DZ-affected" parts of the rock had similar orientation statistics, but significantly higher fracture intensity on average than rock more distant from the deformation zones. The contrast is by a factor of 3 to 4 when 6 m bins are used for averaging of the fracture intensity data, or a factor of 2 to 3 when larger, 30 m bins are used.

For this reason Fox et al. (2007) recommended separate treatment of these "DZ-affected" portions of the rock mass. However, this recommendation has not been carried forward in the site models presented by SKB thus far.

Detailed studies of fracturing adjacent to fault zones commonly suggest a decrease in fracture intensity with distance from the main fault core and secondary faults, which can be expected from the processes by which fault damage zones develop (e.g. Caine, 1999; Geier, 2005). Given that subsidiary faults to a parent fault zone form by similar processes, and given the geometric similarity of structural patterns that are seen on a wide range of scales (Kim et al., 2004), it is furthermore expected that rock adjacent to smaller-scale deformation zones ("minor deformation zones" or MDZs in SKB's nomenclature) could affect fracture intensity in the nearby rock, though on a smaller scale.

Several DFN conceptual models have been developed in the literature to represent this effect in a simple way. Examples include the "parent-daughter" model of Billaux et al. (1989), which is based on a geostatistical model for spatial correlation of "daughter" fractures to larger "parent" fractures, and the "nearest neighbor" model of Dershowitz et al. (1998) which has a simpler, exponential decay of fracture intensity with distance from the nearest "parent" fracture.

Termination relationships among fracture sets are significant for hydrogeology, because fracture systems with non-zero termination percentages are more well-connected than non-terminating systems with identical fracture intensities.

Termination relationships among fracture sets are also significant for assessment of seismic risk. SKB's method of analysis (Hedin, 2007) takes credit for the portion of a fracture over which the displacement for a given seismic event is predicted to be less than a critical value that could result in shear failure of a canister. The method is based on a theoretical elastic solution for the deformation of an idealized, disk-shaped crack with zero-slip boundaries. In a fracture system with non-zero termination percentages, the assumption of zero-displacement boundaries does not always hold, so critical levels of displacement may occur across a larger fraction of the fracture area than assumed in this method.

Analysis

Effect of deformation zones on fracture intensity

To explore the applicability of a model in which fracture intensity is a function of proximity to deformation zones, data from the core-drilled holes at drill sites BP 01-10 were plotted and examined in terms of:

- Fracture intensity vs. distance to nearest major deformation zone;
- Fracture intensity vs. distance to nearest major or minor deformation zone.

Data from later drill sites were excluded as these sites were not included in the data delivery that was used. Data processing details and preliminary plots are given in a project memorandum (Geier, 2010c).

To investigate fracture intensity as a function of distance to the nearest major deformation zone, the one-dimensional fracture intensity (P_{01}) data for 1 m intervals were sorted based on the fracture domains FFM01 through FFM06 as defined by Olofsson et al. (2007).

For each P_{01} data point belonging to a given fracture domain, the distance along the borehole from the nearest major deformation zone was then calculated based on SKB's extended single-hole interpretation (ESHI). The ESHI deformation zones are presumed to correspond to major deformation zones, with lengths of 1000 m or more.

The same data as in the preceding step were sorted further by identifying possible minor deformation zones, then calculating the distance to the nearest deformation zone (either major or minor).

Since minor deformation zones (MDZs) were not identified in the ESHI, a threshold intensity $P_{01} > 20$ m^{-1} (i.e. a mean fracture spacing of 5 cm or less) was assumed to be indicative of a MDZ. The choice of this threshold was essentially arbitrary; however the value chosen represents a value 3 times as high as the mean P_{01} in FFM02, the most intensely fractured of the domains considered. Two of the domains (FFM03 and FFM06) have no intervals with $P_{01} > 20$ m^{-1}, so are not assigned any MDZs with this choice of threshold for fracture intensity.

Exponential halo model for 1-D intensity measure

Based on inspection, a simple exponential decay model was postulated to represent an apparent decrease in the mean value of fracture intensity $\overline{P}$ as a function of the distance h from the nearest deformation zone (major or minor), of the form:

$$\overline{P}(h) = P_\infty \left[1 + ae^{-\alpha h} \right]$$

where:

h = distance to the nearest deformation zone (major or minor);
P_∞ = mean P_{01} fracture intensity of the background rock (far from the influence of any zone);
a, α = fitting parameters

The first fitting parameter a is related to the mean value of fracture intensity immediately adjacent to deformation zones:

$$\overline{P}(0) = P_\infty \left[1 + a \right]$$

$$a = \frac{\overline{P}(0)}{P_\infty} - 1$$

while the second fitting parameter α determines the exponential rate at which mean fracture intensity decays with distance h.

For a given fracture domain, values of P_∞ and a were estimated graphically and the value of α was adjusted manually to approximately minimize the squared residuals:

$$r^2 = \sum_i \left[P_{01}(x_i) - \overline{P}(h(x_i)) \right]^2$$

where:

x_i = position of the centre of the ith borehole interval (of 1 m length)
$h(x_i)$ = calculated value of h at this position.
and the sum is taken over all 1 m intervals that are within the fracture domain.

Parameter values estimated by this method are listed in Table 3.1 for FFM01, FFM02, and FFM04 & FFM05 (analysed in combination). Plots comparing the data with the fitted functions are given in in Figures 3.1 through 3.3. The data show a very wide scatter around the fitted functions. The extent to which this scatter can be attributed to stochastic variation and sampling volumes in a discrete network can best be addressed by simulation, as explored in the later sections of this report.

Of the three domains, FFM01 has the lowest background fracture intensity as represented by P_∞, but also appears to have the strongest influence of deformation zones. Since FFM01 is the main host rock for the proposed repository, this contrast may be of importance for the near-field performance.

These estimates can form the basis for an alternative fracture model that is generated sequentially, by simulating larger features (minor deformation zones) first, then smaller features with intensity based on proximity to the nearest MDZ.

The choice of the dividing point between larger and smaller features is essentially arbitrary for an analysis based entirely on borehole data, because the sizes of fractures intersecting boreholes are essentially unknown. For the purpose of scoping the potential effects of this type of model, the division is chosen at a fracture diameter of 100 m, which corresponds approximately to the scale of features that are recognized as "minor deformation zones" (MDZs) in SKB's surface-based site investigations.

Table 3.1 Parameter values for deformation-zone influenced fracture-intensity model for Forsmark fracture domains.

Fracture domain	FFM01	FFM02	FFM04 & FFM05
P_∞ [m^{-1}]	1	2	1.5
a [–]	6	3.5	5
α [m^{-1}]	0.2	0.2	0.05

Figure 3.1 Plot of fracture intensity in core-drilled holes as a function of distance from the nearest deformation zone identified by the extended single-hole interpretation, with fitted exponential-halo model in red, for Fracture Domain FFM01.

Figure 3.2 Plot of fracture intensity in core-drilled holes as a function of distance from the nearest deformation zone identified by the extended single-hole interpretation, with fitted exponential-halo model in red, for Fracture Domain FFM02.
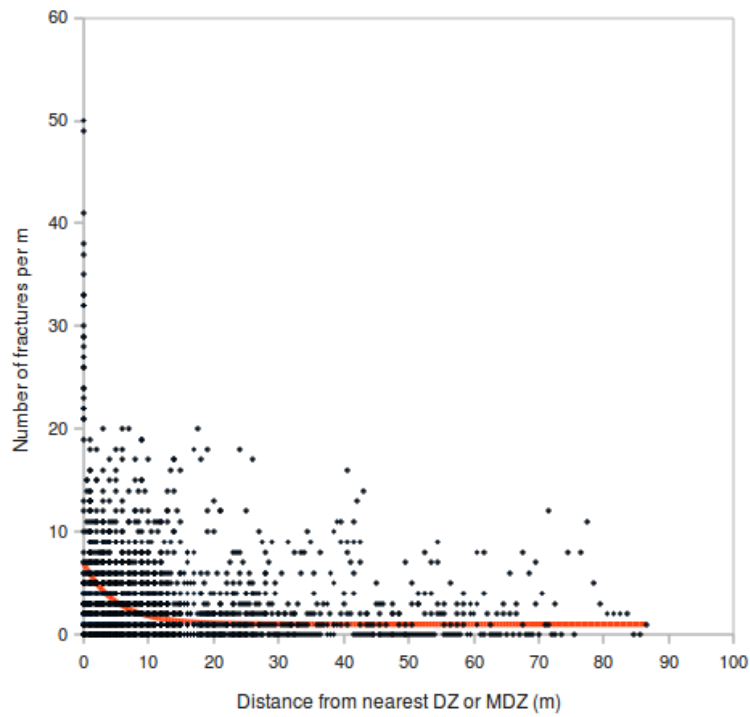
Figure 3.3 Plot of fracture intensity in core-drilled holes as a function of distance from the nearest deformation zone identified by the extended single-hole interpretation, with fitted exponential-halo model in red, for Fracture Domains FFM04 and FFM05.
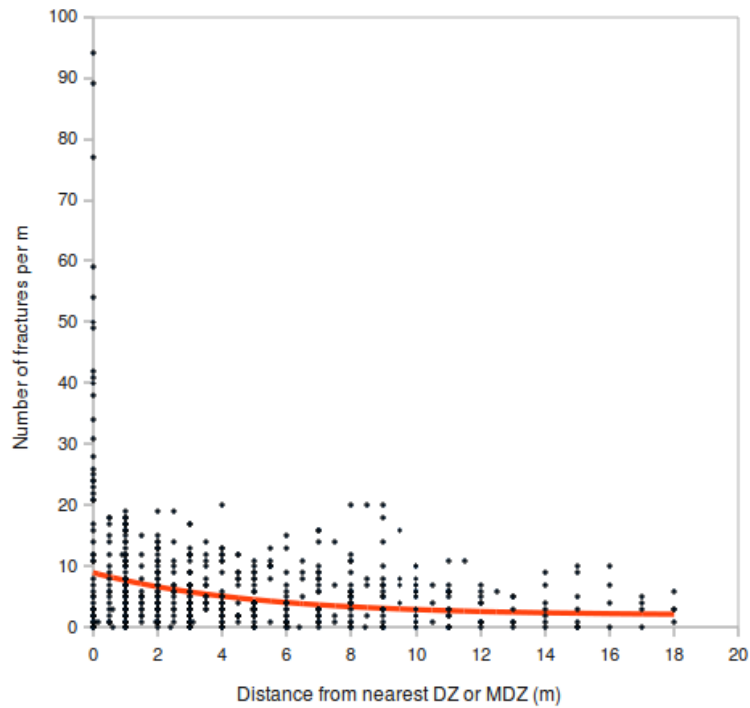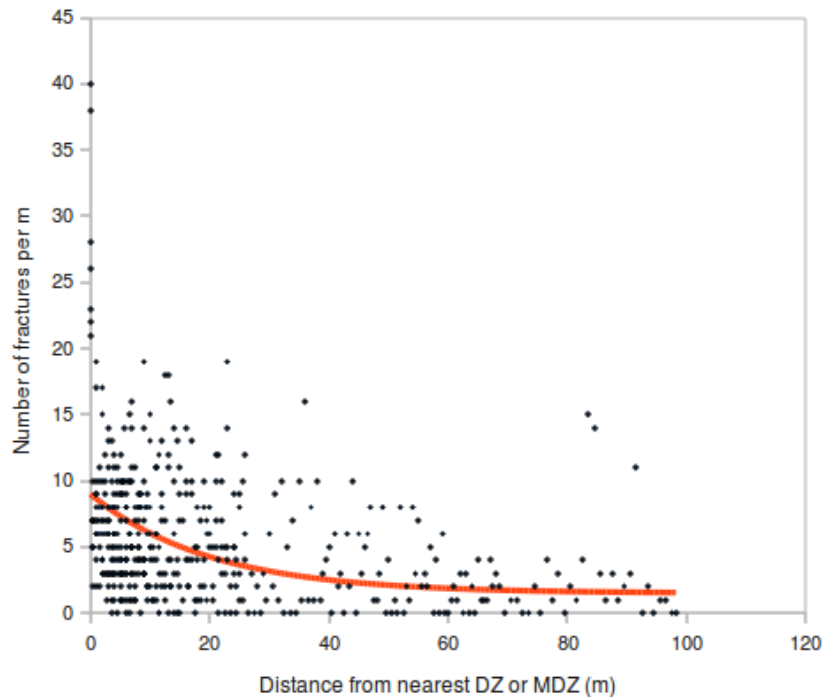
Termination relationships

Termination relationships among fracture sets were analysed by Fox et al. (2007, p. 172-173). These results are reproduced here in Tables 3.2 and 3.3 for ease of reference. Termination percentages were only for fracture domains FFM02 and FFM03, due to a lack of outcrop data to assess this characteristic for other fracture domains. The outcrop mapping methodology did not permit analysis of terminations between the sub-horizontal fracture set and the sub-vertical sets.

Termination percentages are generally over 50%, with the exception of one fracture set (the NE striking set) in domain FFM02. Thus most fractures identified from outcrops at Forsmark terminate at intersections with other fractures. The highest termination percentage evaluated is 81.9% for the ENE-striking set in FFM03. Despite these findings, termination of fractures at intersections has not been carried forward in the site modelling by SKB.

Fox et al. (2007) infer an order of set generation based on the principle that younger fracture sets will more often terminate against older sets, than vice versa. However, from Tables 3.2 and 3.3 it is evident that "older" sets frequently terminate against "younger" sets. For example, in FFM02, about

20% of the fractures in the NE-striking set terminate against the NW-striking set, despite that the latter is judged to be younger.

A possible alternative interpretation is that many of these fractures were co-eval, and formed as conjugate members of a fault array. From the structural geologic interpretation of the site (Stephens et al., 2007; Stephens et al., 2008), it is further expected that many of the fractures have been reactivated and developed further under different tectonic regimes. In such a system, termination relations will tend to reflect a hierarchy of scales, with subsidiary faults terminating at higher-order faults regardless of orientation. Differences in termination percentages among sets can help to indicate which fault orientations most frequently corresponded to the dominant shear plane orientations.

This alternative interpretation is supported by visual inspection of the outcrop maps as given in Appendix 8 of Fox et al. (2007), which show many smaller fractures terminating against longer fracture traces. Quantitative analysis of this aspect could be possible, as an extension of this project, by analysis of map data.

Table 3.2 Relative termination percentage between fracture sets and inferred order of fracture set generation for fracture domain FFM02, adapted from Table 4-80 of Fox et al., 2007.

Fracture set (inferred order)	NE (1)	NW (2)	EW (3)	NS (4)	Total % termination
NE terminates against	–	19.5%	11.1%	7.3%	38.0%
-NW terminates against	33.2%	–	11.5%	5.9%	50.7%
EW terminates against	35.1%	19.5%	–	9.4%	64.0%
NS terminates against	26.9%	18.7%	12.7%	–	58.2%

Table 3.3 Relative termination percentage between fracture sets and inferred order of fracture set generation for fracture domain FFM03, adapted from Table 4-81 of Fox et al., 2007.

Fracture set (inferred order)	NW (1)	WNW (2)	NE (3)	NS (4)	ENE (5)	Total % termination
NW terminates against	–	16.0%	19.1%	7.2%	10.9%	53.2%
WNW terminates against	24.2%	–	21.7%	4.5%	9.4%	59.8%
NE terminates against	23.1%	15.6%	–	5.0%	11.8%	55.5%
NS terminates against	25.9%	18.5%	16.7	–	3.7%	64.8%
ENE terminates against	34.0%	17.0%	23.9%	6.9	–	81.9%

Discussion

Preliminary analysis indicates that the fracture system at Forsmark is spatially organized in the sense that smaller fractures are spatially correlated to larger features (minor deformation zones), and also that smaller fractures tend to terminate against larger structures.

Scaling 3-D fracture intensity measures

The estimates in Table 3.1 can form the basis for an alternative fracture model that is generated sequentially, by simulating larger features (minor deformation zones) first, then smaller features with intensity based on proximity to the nearest MDZ.

The function $\overline{P}(h)$ above has been derived independent of fracture sets. For application this is treated as a weighting function for the 3-D intensity measures of the individual fracture sets, to yield a model in which fracture intensity varies as a function of the distance to the nearest deformation zone:

$$P_{32i}(h) \quad = \quad \frac{\overline{P}_{32i}}{C_P}\,\overline{P}(h)$$

Here $\overline{P}_{32i}$ is the mean 3-D intensity of the ith fracture set in a given fracture domain (as defined in SKB's site descriptive model, used as the base case here), and C_P is a normalization factor satisfying:

$$\int_V P_{32i}(h) \quad = \quad \overline{P}_{32i}$$

where the integral is taken over the fracture domain. This is to ensure that the fracture intensity, when averaged over the domain, is equal to that for the base-case. This condition is satisfied when:

$$C_P \quad = \quad \int_V \overline{P}(h)dV$$

In principal the normalization factor C_P can be estimated by Monte Carlo integration over the fracture domain for a given realization of MDZs. However, as a practical matter for the implementation method adopted here, determining the value of C_P is not necessary, since fractures are generated one at a time until the target value of P_{32i} is reached.

An implicit assumption in this approach is that the intensities of all fracture sets vary in a similar way as a function of h. If this assumption is relaxed so that the intensity of each fracture set varies independently of the others, the result would be a more complex model. For such a model, the analysis would need to be repeated using three-dimensional (P_{32i}) fracture intensity estimates for individual fracture sets, following the analytical correction procedure described by Fox *et al.* (2007, p. 45-46). This more complex type of model was not attempted in the present study, in favor of testing whether a simpler change in conceptual model could produce significant effects.

The estimates given in Table 3.1 are based on one-dimensional (P_{01}) fracture intensity data from along boreholes, which have not been corrected for orientation bias. The parameter estimates could also be made more exact by non-linear least-squares fitting (*e.g.* using the Levenberg-Marquardt algorithm rather than manual adjustment). These refinements are desirable but would likely only result in minor changes, compared to the main effect of introducing this spatially heterogeneous model in place of SKB's more homogeneous model.

Two alternative DFN conceptual model variants are suggested to investigate the consequences of this spatial organization for a repository at Forsmark. Both make use of the same fracture set definitions as defined by SKB, including the fitted probability distributions for fracture orientation, size, and transmissivity. The only differences are as follows:

(1) **Spatially correlated variant:** Fractures in different size classes are simulated sequentially, starting with the largest class of features. Intensity for smaller classes of fractures scales with distance from the nearest larger-scale feature (DZ or MDZ), according to the inverse exponential relationship with parameters as defined in Section 3.1.

(2) **Spatially correlated variant with hierarchical termination:** As for the preceding variant, but with probabilistic termination of smaller fractures at intersections with larger fractures to match (approximately) the observed termination percentages as listed in Tables 3.2 and 3.3.

Priority was given to the first of these variants, which was expected to be more significant than the second.

The second variant (with terminations) is expected to be significant only very close to the repository, where it can affect the discrete connectivity of pathways from deposition holes to larger features. With the method used to calculate equivalent hydraulic conductivity values for assignment to grid features farther from the deposition holes, this level of detail will have no influence.

4. Implementation of alternative exponential halo model

Mathematical development and implementation

The exponential halo model was implemented as a new option in the *fracgen* module of the DFM package, Version 2.3.4.

This required development of a method for stochastic simulation of fracture locations in a non-uniform intensity field of the specified form, rather than as a uniform Poisson process. Three different types of algorithms were considered:

1) Acceptance-rejection method (generating random points by a uniform Poisson process, then thinning these depending on comparison to a test function based on the exponential-halo model);
2) Spatial binning using an adaptation of the bubble-cover algorithm as described in the DFM user documentation (Geier, 2010h), in which the mean intensity within each bubble is calculated based on Monte Carlo integration of the function $P(h)$ within the bubble volume; and
3) Spatial transformation method in which points simulated by a uniform Poisson point process are shifted toward the nearest larger feature.

The first type of algorithm was rejected as it would require generation and testing of close to $(a+1)$ times as many points as are needed, in each case finding the distance to the closest parent feature, and then calculating the test function.

The second approach might well be the fastest (particularly for simulating a large number of fracture centres), but its accuracy would depend on the coarseness of the bubble cover, as well as the convergence of the Monte Carlo integration.

The spatial transformation approach was therefore chosen for development at this stage of the project, as it produces one fracture per simulated point, and does not depend on the degree of refinement as would be the case for the bubble-cover algorithm.

The steps in the spatial transformation algorithm (derived as part of this project) are:
1. Generate a point x within a given domain based on a uniform Poisson process.
2. Calculate the distance H to the nearest point on the closest parent feature F.

3. Calculate the expected number of points $N(H)$ that would lie within distance H of F, for a Poisson process of uniform average density.
4. Find the rescaled distance h such that the corresponding expected number of points $n(h)$ within distance h of F for the exponential halo model $P(h|P_\infty, a, \alpha)$ is equal to $N(H)$.
5. Shift the point x toward F so that the transformed point x' is at distance h.

Fractures in the child sets are generated by this algorithm one at a time, but each fracture in a child set is independent of each other fracture in the child sets, so in principle this is independent of the sequence. The halo model is created with respect to all of the deformation zones, but the point field intensity at a given point x is defined only with respect to the nearest deformation zone (parent feature) F.

The mathematical development of the algorithm makes use of the following geometrical formulae:

Area of 3-D surface within distance η of a disc of radius r

$$A(\eta) \;=\; 2\pi\!\left(r^2 + \pi r\eta + 2\eta^2\right)$$

Volume within distance η of a disc of radius r

$$V(\eta) \;=\; \pi\eta\!\left(2r^2 + \pi r\eta + \frac{4}{3}\eta^2\right)$$

Expected number of Poisson points within distance H of a disc of radius r

$$N(H) \;=\; P_{avg}V(H) \;=\; P_{avg}\pi H\!\left(2r^2 + \pi rH + \frac{4}{3}H^2\right)$$

where P_{avg} is the average intensity of the Poisson process (points per unit volume).

Expected number of exponential halo points within distance h of a disc of radius r

$$n(h) \;=\; \int_0^h \overline{P}(\eta)A(\eta)d\eta \;=\; P_\infty\int_0^h \left(1 + ae^{-\alpha\eta}\right)A(\eta)d\eta$$

$$n(h) = 2\pi P_\infty\left\{r^2h + \frac{\pi}{2}rh^2 + \frac{2}{3}h^3 + b\left(1 - e^{-\alpha h}\right) - \frac{a}{\alpha}\!\left(\pi r + \frac{4}{\alpha} + 2h\right)he^{-\alpha h}\right\}$$

where:

$$b = \frac{a}{\alpha}\!\left(r^2 + \frac{\pi}{\alpha}r + \frac{4}{\alpha^2}\right)$$

Setting $n(h)$ equal to $N(H)$ and dividing both sides by P_∞ leads to the non-linear equation:

$$\frac{n(h)}{P_\infty} = \frac{P_{avg}}{P_\infty}V(H)$$

The value of P_{avg}, the average intensity of the Poisson point process which is required to achieve a given volumetric fracture intensity P_{32} is generally not known *a priori*. P_{avg} is related to P_{32} by a factor which is a function of the fracture size and orientation distributions for a given fracture domain geometry. In principle this factor could be estimated by Monte Carlo integration over the domain, for each fracture set.

However, since the method of application will be to generate fractures in each set iteratively until a target value of P_{32} is reached, and considering that for a sufficiently large domain P_{avg} approaches P_∞ (though is always slightly larger), here the simplification $P_{avg}/P_\infty \approx 1$ is introduced, to yield:

$$\frac{n(h)}{P_\infty} \approx V(H)$$

The function $n(h)/P_\infty$ increases monotonically with a continuous derivative over all values of $h > 0$, so for a given function value the corresponding value of h is readily obtained by the Newton-Raphson method.

The location of the transformed point is then calculated as:

$$x' = p + \frac{h}{H}(x - p)$$

where p is the closest point on the parent feature F, in relation to the Poisson point x.

5. Evaluation of alternatives using borehole data

Analysis

Fracture statistical models

Fracture populations simulated with the alternative (exponential-halo) model were compared with simulations of SKB's GeoDFN model as used by Munier (2010). The GeoDFN model was used for this comparison rather than the HydroDFN model, as non-transmissive fractures contribute to fracture frequency and fracture spacing measures.

Munier (2010) considers three variants of the GeoDFN model for Forsmark, all of which are based on a Poisson process for fracture locations, but which differ in assumptions regarding the fracture size distribution. Here as a base case for reference, we compare with the r_0-fixed case, which produces the highest degree of utilization according to the calculations by Munier (2010). Calculations are performed only for fracture domain FFM01, which is the main fracture domain that intersects the planned locations of the repository tunnels; the other fracture domain of concern, FFM06, yields similar utilization factors according to Munier (2010).

The fracture set definitions used as *fracgen* input for this base case are listed in Table 5.1. Note that the statistical models for fracture hydraulic properties (transmissivity, storativity, and aperture) are arbitrary and should be disregarded, as these are not defined for the GeoDFN model (the statistical models used apply to the HydroDFN model, but the GeoDFN contains many additional fractures that are regarded as non-transmissive, so these are not correctly represented here).

The exponential-halo model uses the same statistics, but treats GeoDFN fractures with $r > 100$ m as parent features for the smaller fractures. The choice of $r = 100$ m as the dividing point corresponds approximately to the scale of features that tend to be interpreted as minor deformation zones (MDZs) in SKB's site descriptive model. The method of implementation for the exponential halo model in *fracgen* is to split each fracture set into two parts depending on fracture radius: $r > 100$ m (simulated first, for all nine sets defined in the GeoDFN), and $r < 100$ m (simulated afterwards). Major deformation zones defined by SKB's site investigations also serve as parent features for the child fractures; these are loaded in as deterministic surfaces prior to generating the fractures.

The fracture set definitions used as *fracgen* input for the alternative (exponential-halo) model are listed in Table 5.2. Again, the statistical models for fracture hydraulic properties (transmissivity, storativity, and aperture) are

arbitrary and should be disregarded, as these are not defined for the GeoDFN model.

The parameterizations of the parent and child sets are arbitrarily assumed to be equal, apart from the size range limits for each set. Independent parameterizations of parent and child sets could be considered as a more complex alternative model, but would be difficult to justify with the present data, and would lead to a more complicated comparison with SKB's GeoDFN model.

Sampling along boreholes

The simulated-sampling feature of *fracgen* was then used to produce and compare synthetic fracture logs for the base-case (r_0-fixed) and alternative (exponential-halo) models. Borehole geometries were taken from data deliveries as documented in Chapter 2. Fracture intersections generated from both the base-case (Poisson) model and the exponential halo model were printed to the *fracgen* log file, then sorted to yield simulated borehole fracture logs.

Fracture intersections generated from both the base-case (Poisson) model and the exponential halo model were printed to the *fracgen* log file, then sorted to yield simulated borehole fracture logs as excerpted in Table 5.3. These results are plotted for an illustrative selection of the deep core-drilled boreholes, in Figures 5.1 through 5.3.

Fracture spacing in actual boreholes

For comparison with the simulations, fracture spacings were also evaluated from Forsmark core logging data. Source data were taken from the SKB-delivered data file p_fract_core_KFM.xls, along with the limits of fracture domain FFM01 in boreholes as shown in Appendix 4 of Olofsson et al. (2007).

The data file was converted to a csv-format file named p_fract_core_KFM.csv, then processed with an AWK-language script (get_p_fract_core_eshi_FFM01.awk) to extract the data records for fractures inside FFM01. The extracted data were stored as a smaller data file p_fract_core_eshi_FFM01.csv.

Fracture spacing values were then calculated from the extracted data, simply by sorting the records in this last file by borehole name and borehole position (using the adjusted position ADJUSTEDSECUP), and calculating the distance between each neighbouring pair of fractures in a given borehole.

Table 5.1 Fracture set definitions for implementation of base case model, Forsmark fracture domain FFM01, deep sub-domain (continued on next page).

```
# Forsmark-SDM Site
# GeoDFN fracture sets for FFM01 (z < -400 m) based on:
# SKB TR-10-21 Table A3-1 (Munier, 2010), fixed r0 alternative
#
# Arbitrarily:
#  (semi-correlated model for transmissivity vs. r) is from Follin 2008.
#
Set 1   # NE
Transmissivity Loglinear r 0.5 5.3e-11 1.0 limits -2 2
Storativity    Constant  1e-8
Aperture       CubicLaw
Radius         Powerlaw  3.718 0.039  limits 2.8843 564.2
Location       Poisson
Orientation    Fisher    trend 314.90  plunge 1.30  kappa 20.94
Intensity      P32       1.733 unscaled
Set 2   # NS
Transmissivity Loglinear r 0.5 5.3e-11 1.0 limits -2 2
Storativity    Constant  1e-8
Aperture       CubicLaw
Radius         Powerlaw  3.745 0.039  limits 2.8843 564.2
Location       Poisson
Orientation    Fisher    trend 270.10  plunge 5.30  kappa 21.34
Intensity      P32       1.292 unscaled
Set 3   # NW
Transmissivity Loglinear r 0.5 5.3e-11 1.0 limits -2 2
Storativity    Constant  1e-8
Aperture       CubicLaw
Radius         Powerlaw  3.607 0.039  limits 2.8843 564.2
Location       Poisson
Orientation    Fisher    trend 230.10  plunge 4.60  kappa 15.70
Intensity      P32       0.948 unscaled
Set 4   # SH
Transmissivity Loglinear r 0.5 5.3e-11 1.0 limits -2 2
Storativity    Constant  1e-8
Aperture       CubicLaw
Radius         Powerlaw  3.579 0.039  limits 2.8843 564.2
Location       Poisson
Orientation    Fisher    trend  0.80  plunge 87.30  kappa 17.42
Intensity      P32       0.624 unscaled
Set 5   # ENE
Transmissivity Loglinear r 0.5 5.3e-11 1.0 limits -2 2
Storativity    Constant  1e-8
Aperture       CubicLaw
Radius         Powerlaw  3.972 0.039  limits 2.8843 564.2
Location       Poisson
Orientation    Fisher    trend 157.50  plunge 3.10  kappa 34.11
Intensity      P32       0.256 unscaled
```

Table 5.1 (ctd) Fracture set definitions for implementation of base case model, Forsmark fracture domain
FFM01, deep sub-domain.

Set 6   # EW
Transmissivity Loglinear r 0.5 5.3e-11 1.0 limits -2 2
Storativity   Constant 1e-8
Aperture   CubicLaw
Radius   Powerlaw 3.930 0.039 limits 2.8843 564.2
Location   Poisson
Orientation   Fisher   trend 0.40 plunge 11.90 kappa 13.89
Intensity   P32   0.169 unscaled
Set 7   # NNE
Transmissivity Loglinear r 0.5 5.3e-11 1.0 limits -2 2
Storativity   Constant 1e-8
Aperture   CubicLaw
Radius   Powerlaw 4.000 0.039 limits 2.8843 564.2
Location   Poisson
Orientation   Fisher   trend 293.80 plunge 0.00 kappa 21.79
Intensity   P32   0.658 unscaled
Set 8   # SH2
Transmissivity Loglinear r 0.5 5.3e-11 1.0 limits -2 2
Storativity   Constant 1e-8
Aperture   CubicLaw
Radius   Powerlaw 3.610 0.039 limits 2.8843 564.2
Location   Poisson
Orientation   Fisher   trend 164.00 plunge 52.60 kappa 35.43
Intensity   P32   0.081 unscaled
Set 9   # SH3
Transmissivity Loglinear r 0.5 5.3e-11 1.0 limits -2 2
Storativity   Constant 1e-8
Aperture   CubicLaw
Radius   Powerlaw 3.610 0.039 limits 2.8843 564.2
Location   Poisson
Orientation   Fisher   trend 337.90 plunge 52.90 kappa 17.08
Intensity   P32   0.067 unscaled

Table 5.2 Fracture set definitions for implementation of halo model, Forsmark fracture domain FFM01, deep sub-domain (continued on following pages).

```
# Forsmark-SDM Site
# GeoDFN fracture sets for FFM01 (z < -400 m) based on:
# SKB TR-10-21 Table 5-1 (Munier, 2010)
#
# Arbitrarily:
# (semi-correlated model for transmissivity vs. r) is from Follin 2008.
#
Set 1  # NE
Transmissivity Loglinear r 0.5 5.3e-11 1.0 limits -2 2
Storativity   Constant  1e-8
Aperture      CubicLaw
Radius        Powerlaw  3.718 0.039  limits 100 564.2
Location      Poisson
Orientation   Fisher   trend 314.90  plunge 1.30  kappa 20.94
Intensity     P32       1.733 unscaled
Set 2  # NS
Transmissivity Loglinear r 0.5 5.3e-11 1.0 limits -2 2
Storativity   Constant  1e-8
Aperture      CubicLaw
Radius        Powerlaw  3.745 0.039  limits 100 564.2
Location      Poisson
Orientation   Fisher   trend 270.10  plunge 5.30  kappa 21.34
Intensity     P32       1.292 unscaled
Set 3  # NW
Transmissivity Loglinear r 0.5 5.3e-11 1.0 limits -2 2
Storativity   Constant  1e-8
Aperture      CubicLaw
Radius        Powerlaw  3.607 0.039  limits 100 564.2
Location      Poisson
Orientation   Fisher   trend 230.10  plunge 4.60  kappa 15.70
Intensity     P32       0.948 unscaled
Set 4  # SH
Transmissivity Loglinear r 0.5 5.3e-11 1.0 limits -2 2
Storativity   Constant  1e-8
Aperture      CubicLaw
Radius        Powerlaw  3.579 0.039  limits 100 564.2
Location      Poisson
Orientation   Fisher   trend  0.80  plunge 87.30  kappa 17.42
Intensity     P32       0.624 unscaled
Set 5  # ENE
Transmissivity Loglinear r 0.5 5.3e-11 1.0 limits -2 2
Storativity   Constant  1e-8
Aperture      CubicLaw
Radius        Powerlaw  3.972 0.039  limits 100 564.2
Location      Poisson
Orientation   Fisher   trend 157.50  plunge 3.10  kappa 34.11
Intensity     P32       0.256 unscaled
```

Table 5.2 (ctd) Fracture set definitions for implementation of halo model, Forsmark fracture domain FFM01, deep sub-domain.

```
Set 6   # EW
Transmissivity Loglinear r 0.5 5.3e-11 1.0 limits -2 2
Storativity   Constant 1e-8
Aperture      CubicLaw
Radius        Powerlaw  3.930 0.039  limits 100 564.2
Location      Poisson
Orientation   Fisher   trend  0.40  plunge 11.90  kappa 13.89
Intensity     P32        0.169 unscaled
Set 7   # NNE
Transmissivity Loglinear r 0.5 5.3e-11 1.0 limits -2 2
Storativity   Constant 1e-8
Aperture      CubicLaw
Radius        Powerlaw  4.000 0.039  limits 100 564.2
Location      Poisson
Orientation   Fisher   trend 293.80  plunge  0.00  kappa 21.79
Intensity     P32        0.658 unscaled
Set 8   # SH2
Transmissivity Loglinear r 0.5 5.3e-11 1.0 limits -2 2
Storativity   Constant 1e-8
Aperture      CubicLaw
Radius        Powerlaw  3.610 0.039  limits 100 564.2
Location      Poisson
Orientation   Fisher   trend 164.00  plunge 52.60  kappa 35.43
Intensity     P32        0.081 unscaled
Set 9   # SH3
Transmissivity Loglinear r 0.5 5.3e-11 1.0 limits -2 2
Storativity   Constant 1e-8
Aperture      CubicLaw
Radius        Powerlaw  3.610 0.039  limits 100 564.2
Location      Poisson
Orientation   Fisher   trend 337.90  plunge 52.90  kappa 17.08
Intensity     P32        0.067 unscaled
Set 10  # NE child
Transmissivity Loglinear r 0.5 5.3e-11 1.0 limits -2 2
Storativity   Constant 1e-8
Aperture      CubicLaw
Radius        Powerlaw  3.718 0.039  limits 2.8843 100
Location      Halo     P 1 a 6 alpha 0.2 parents 0 1 2 3 4 5 6 7 8 9
Orientation   Fisher   trend 314.90  plunge  1.30  kappa 20.94
Intensity     P32        1.733 unscaled
Set 11  # NS child
Transmissivity Loglinear r 0.5 5.3e-11 1.0 limits -2 2
Storativity   Constant 1e-8
Aperture      CubicLaw
Radius        Powerlaw  3.745 0.039  limits 2.8843 100
Location      Halo     P 1 a 6 alpha 0.2 parents 0 1 2 3 4 5 6 7 8 9
Orientation   Fisher   trend 270.10  plunge  5.30  kappa 21.34
Intensity     P32        1.292 unscaled
```

Table 5.2 (ctd) Fracture set definitions for implementation of halo model, Forsmark fracture domain FFM01, deep sub domain.

```
Set 12  # NW child
Transmissivity Loglinear r 0.5 5.3e-11 1.0 limits -2 2
Storativity    Constant  1e-8
Aperture       CubicLaw
Radius         Powerlaw  3.607 0.039  limits 2.8843 100
Location       Halo     P 1 a 6 alpha 0.2 parents 0 1 2 3 4 5 6 7 8 9
Orientation    Fisher   trend 230.10  plunge  4.60  kappa 15.70
Intensity      P32       0.948 unscaled
Set 13  # SH child
Transmissivity Loglinear r 0.5 5.3e-11 1.0 limits -2 2
Storativity    Constant  1e-8
Aperture       CubicLaw
Radius         Powerlaw  3.579 0.039  limits 2.8843 100
Location       Halo     P 1 a 6 alpha 0.2 parents 0 1 2 3 4 5 6 7 8 9
Orientation    Fisher   trend  0.80  plunge 87.30  kappa 17.42
Intensity      P32       0.624 unscaled
Set 14  # ENE child
Transmissivity Loglinear r 0.5 5.3e-11 1.0 limits -2 2
Storativity    Constant  1e-8
Aperture       CubicLaw
Radius         Powerlaw  3.972 0.039  limits 2.8843 100
Location       Halo     P 1 a 6 alpha 0.2 parents 0 1 2 3 4 5 6 7 8 9
Orientation    Fisher   trend 157.50  plunge  3.10  kappa 34.11
Intensity      P32       0.256 unscaled
Set 15  # EW child
Transmissivity Loglinear r 0.5 5.3e-11 1.0 limits -2 2
Storativity    Constant  1e-8
Aperture       CubicLaw
Radius         Powerlaw  3.930 0.039  limits 2.8843 100
Location       Halo     P 1 a 6 alpha 0.2 parents 0 1 2 3 4 5 6 7 8 9
Orientation    Fisher   trend  0.40  plunge 11.90  kappa 13.89
Intensity      P32       0.169 unscaled
Set 16  # NNE child
Transmissivity Loglinear r 0.5 5.3e-11 1.0 limits -2 2
Storativity    Constant  1e-8
Aperture       CubicLaw
Radius         Powerlaw  4.000 0.039  limits 2.8843 100
Location       Halo     P 1 a 6 alpha 0.2 parents 0 1 2 3 4 5 6 7 8 9
Orientation    Fisher   trend 293.80  plunge  0.00  kappa 21.79
Intensity      P32       0.658 unscaled
Set 17  # SH2 child
Transmissivity Loglinear r 0.5 5.3e-11 1.0 limits -2 2
Storativity    Constant  1e-8
Aperture       CubicLaw
Radius         Powerlaw  3.610 0.039  limits 2.8843 100
Location       Halo     P 1 a 6 alpha 0.2 parents 0 1 2 3 4 5 6 7 8 9
Orientation    Fisher   trend 164.00  plunge 52.60  kappa 35.43
Intensity      P32       0.081 unscaled
```

Table 5.2 (ctd) Fracture set definitions for implementation of halo model, Forsmark fracture domain FFM01, deep sub-domain.

```
Set 18  # SH3 child
Transmissivity Loglinear r 0.5 5.3e-11 1.0 limits -2 2
Storativity   Constant  1e-8
Aperture      CubicLaw
Radius        Powerlaw  3.610 0.039  limits 2.8843 100
Location      Halo      P 1 a 6 alpha 0.2 parents 0 1 2 3 4 5 6 7 8 9
Orientation   Fisher    trend 337.90  plunge 52.90  kappa 17.08
Intensity     P32       0.067 unscaled
```

Table 5.3. Excerpt of a simulated fracture log for multiple boreholes. L is distance along the borehole to the given fracture intersection, strike & dip of the fracture are given in degrees following the usual right-hand convention for dip, T is fracture transmissivity, (X,Y,Z) are the global coordinates of the fracture's intersection with the centre line of a given borehole segment, and (nx, ny, nz) are the components of the fracture normal vector.

Borehole	L (m)	Strike	Dip	$T(\mathrm{m}^2/\mathrm{s})$	X (m)	Y (m)	Z (m)	n_x	n_y	n_z
HFM01	140.31	358.9	8.2	3.76e-06	1631499.98	6699621.85	-136.64	-0.003	0.142	0.990
HFM01	147.99	19.0	1.2	3.63e-08	1631501.07	6699622.59	-144.21	0.007	0.019	1.000
HFM01	168.92	180.2	10.6	2.99e-05	1631504.23	6699624.80	-164.77	-0.001	-0.183	0.983
HFM01	172.31	213.1	8.8	1.16e-05	1631504.77	6699625.19	-168.10	-0.083	-0.128	0.988
HFM01	187.54	72.8	27.3	9.03e-06	1631507.31	6699627.04	-182.99	0.439	0.136	0.888
HFM01	192.48	247.8	10.0	6.07e-07	1631508.17	6699627.67	-187.82	-0.160	-0.065	0.985
HFM01	194.06	270.0	36.5	9.44e-07	1631508.44	6699627.88	-189.36	-0.595	0.001	0.804
HFM01	194.41	281.0	46.9	8.07e-06	1631508.51	6699627.92	-189.71	-0.717	0.139	0.683
HFM16	118.94	148.5	21.6	4.17e-08	1632468.43	6699717.95	-115.25	0.193	-0.314	0.930
HFM16	122.74	20.2	17.8	9.34e-06	1632469.00	6699717.52	-118.99	0.106	0.287	0.952
HFM16	128.23	140.5	15.1	7.37e-08	1632469.90	6699716.85	-124.36	0.165	-0.201	0.966
HFM16	129.08	63.6	30.4	8.80e-05	1632470.04	6699716.75	-125.19	0.454	0.225	0.862
HFM17	108.95	338.2	35.8	5.28e-08	1633263.24	6699471.67	-104.53	-0.217	0.543	0.811
HFM20	100.75	355.5	20.6	1.53e-05	1630776.53	6700193.17	-97.59	-0.028	0.350	0.936
HFM20	111.34	36.4	49.0	2.10e-06	1630776.43	6700193.38	-108.18	0.448	0.607	0.656
HFM20	114.94	190.2	25.9	1.77e-04	1630776.37	6700193.43	-111.78	-0.077	-0.430	0.899
HFM20	118.39	161.9	32.6	7.29e-05	1630776.31	6700193.46	-115.23	0.168	-0.513	0.842
HFM20	128.50	37.8	5.1	6.24e-06	1630776.09	6700193.45	-125.34	0.055	0.070	0.996
HFM20	135.59	57.0	11.4	1.55e-06	1630775.90	6700193.41	-132.42	0.166	0.108	0.980
HFM20	136.13	134.1	46.1	7.88e-07	1630775.89	6700193.40	-132.96	0.517	-0.501	0.694
HFM20	140.03	95.1	23.8	2.57e-07	1630775.77	6700193.37	-136.86	0.403	-0.036	0.915
HFM20	142.28	331.0	54.0	1.86e-07	1630775.70	6700193.34	-139.11	-0.392	0.708	0.588

...

Results

The results are plotted for an illustrative selection of the deep core-drilled boreholes, in Figures 5.1 through 5.3. Results are plotted as fracture spacing versus depth (rather than as interval transmissivity vs. depth as in the preceding memorandum, Geier 2010d, since the statistical model for fracture transmissivity is arbitrary as discussed above).

A noticeable difference between the two models, when plotted in this way, is that fracture spacing values appear to be spatially correlated with respect to distance along the boreholes. The exponential-halo model tends to produce long intervals with very few fractures (most strikingly, the interval from 760 m to 880 m depth in KFM05A, in realization 1).

As seen from Table 5.4, the total number of fractures that intersect the boreholes in fracture domain FFM01, is similar for two realizations of the base-case model, and one realization of the exponential-halo model. The other realization of the exponential-halo model yields about 20% more intersections with boreholes. Similar results are obtained for mean fracture frequency. This is apparently due to chance location of a few stochastic "parent" fractures in the second realization of the exponential-halo model, which leads to more clusters of "child" fractures that intersect the boreholes.

The median fracture spacings for these two realizations of the exponential-halo model are lower by 15% to 22% than for the realization of the base-case model that produced the lowest median fracture spacing. However due to the substantial variability in this measure between realizations (+/- 6% for the base-case and +/- 5% for the halo model), additional realizations may be needed to determine if median fracture spacing is a robust statistic for comparison between models.

Table 5.4 Statistical summary of results from simulations of borehole sampling comparing two different models of the fracture population in Fracture Domain FFM01 at Forsmark. Results are combined for all 17 boreholes that penetrated FFM01 (at the time of the data freeze for the data delivery used as the basis for these calculations), for two different realizations of each model.

Calculation case	Poisson (SDM-Site r_0-fixed variant)		Exponential Halo	
Realization	1	2	1	2
Number of borehole intersections	630	651	634	757
Mean fracture frequency in boreholes (per m)	0.17	0.17	0.17	0.2
Median fracture spacing	4.54	4.02	3.43	3.14

**Poisson Model
Realization 01**

Borehole KFM01A

**Poisson Model
Realization 02**

Borehole KFM01A

**Exponential Halo Model
Realization 01**

Borehole KFM01A

**Exponential Halo Model
Realization 02**
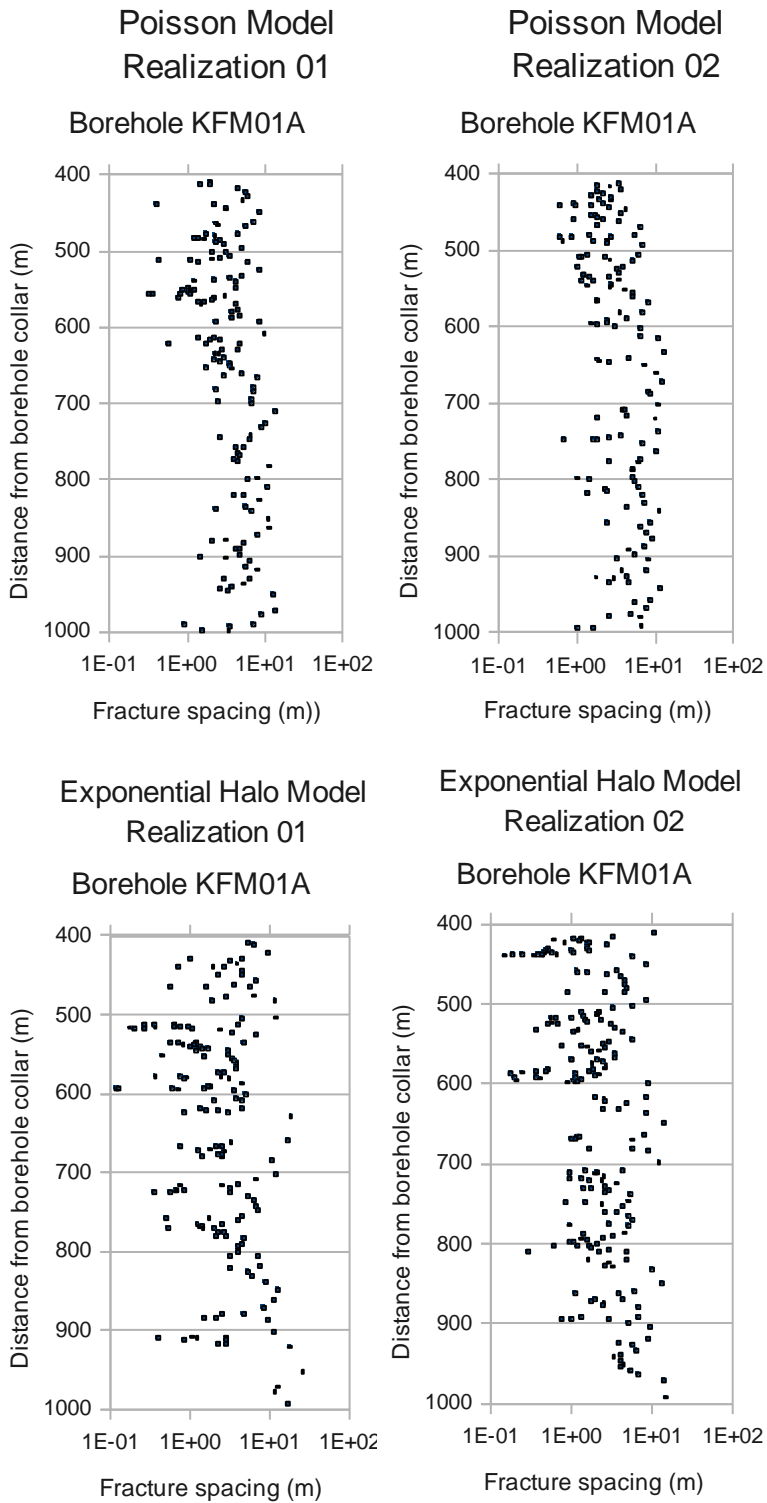
Borehole KFM01A

Figure 5.1 Simulated fracture logs for Fracture Domain FFM01, Borehole KFM01A.

Poisson Model
Realization 01

Borehole KFM05A

Poisson Model
Realization 02

Borehole KFM05A

Exponential Halo Model
Realization 01

Borehole KFM05A

Exponential Halo Model
Realization 02
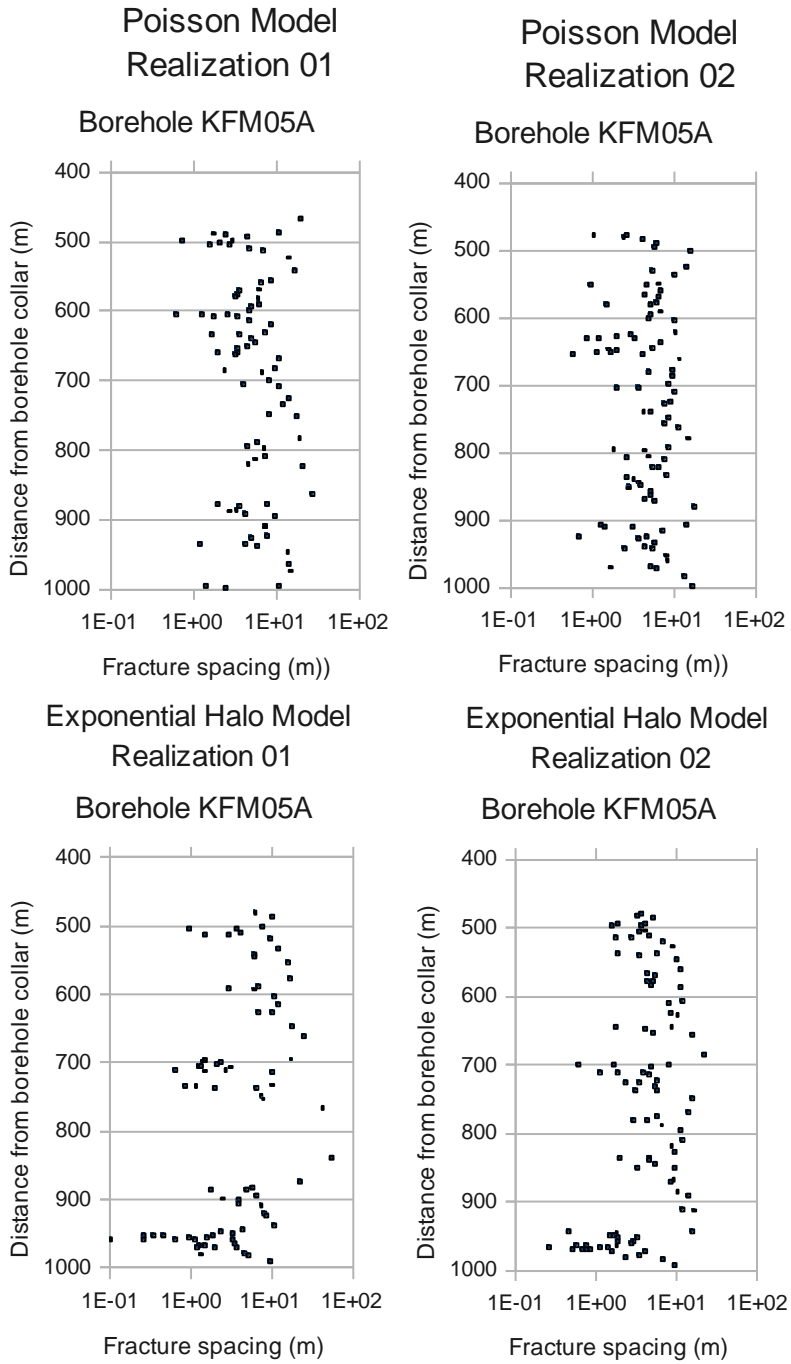
Borehole KFM05A

Figure 5.2 Simulated fracture logs for Fracture Domain FFM01, Borehole KFM05A.
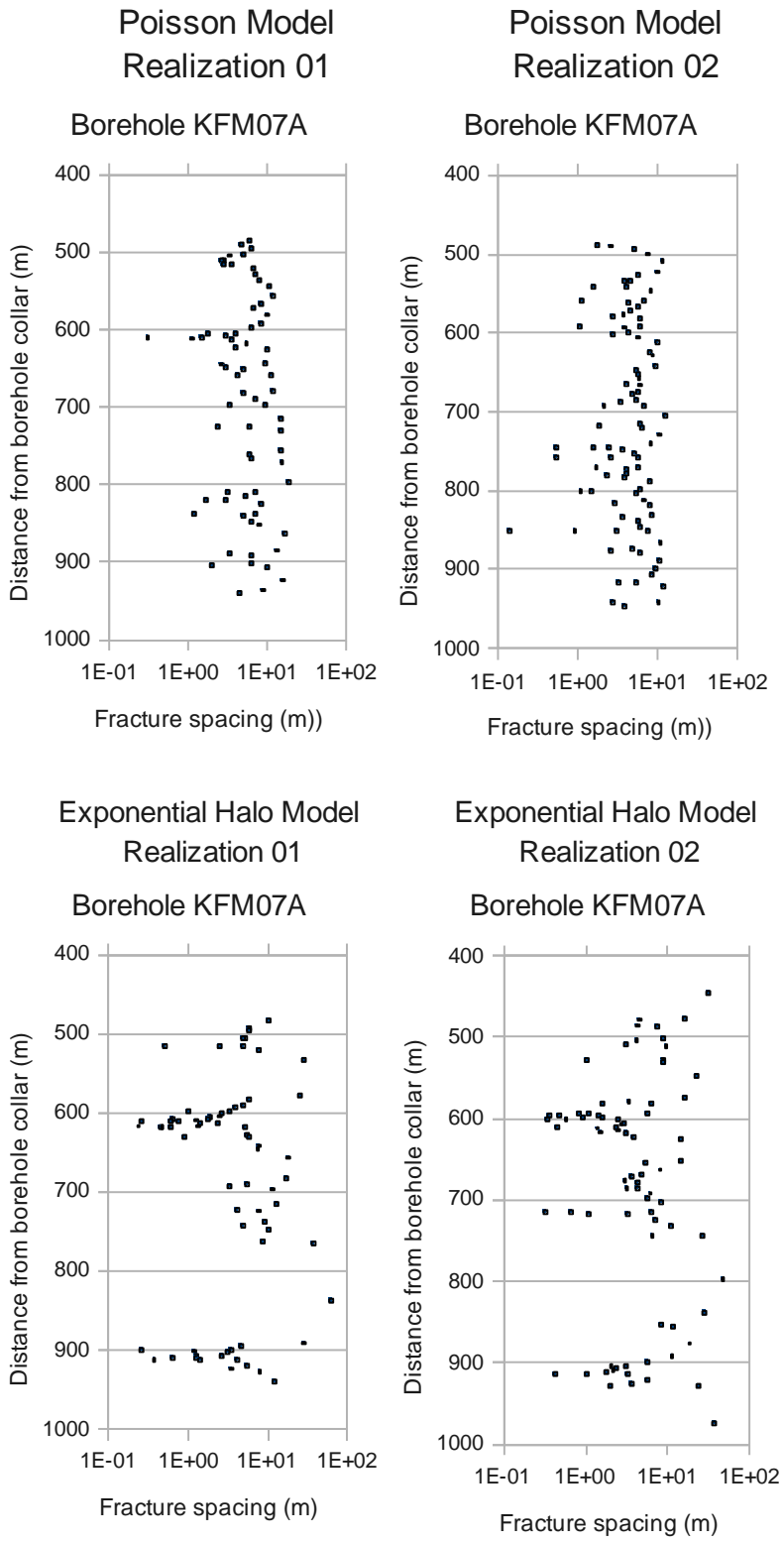
Figure 5.3 Simulated fracture logs for Fracture Domain FFM01, Borehole KFM07A.

The cumulative density functions for fracture spacing (Figure 5.4) also show substantial distinctions between the two models, as well as between two realizations of a given model. A Kolmogorov-Smirnov test comparing the halo model to the Poisson model (comparing the closest realizations of each) yields a probability of only 0.08% that the spacing samples are drawn from the same parent distribution; in other words this hypothesis can be rejected at a significance level of 99.9%.

The corresponding probability for the observed difference between realizations of the Poisson model is 40%. The probability for the observed differences between realizations of the halo model is 35%. Thus the differences between realizations of a given model are much less significant than the difference between models. This result suggests that comparison of fracture spacing distributions could be a way to distinguish between these two models based on borehole data.

However, fracture spacing distributions calculated from actual borehole data from Fracture Domain FFM0, as also shown in Figure 5.4, show large differences with both the Poisson model and the exponential halo model. This is true regardless of whether fracture spacings are calculated based on (1) all fractures, (2) only fractures that were characterized either as open or partly open/partly sealed, or (3) only open fractures. Possible explanations for this large discrepancy are discussed in the following section.
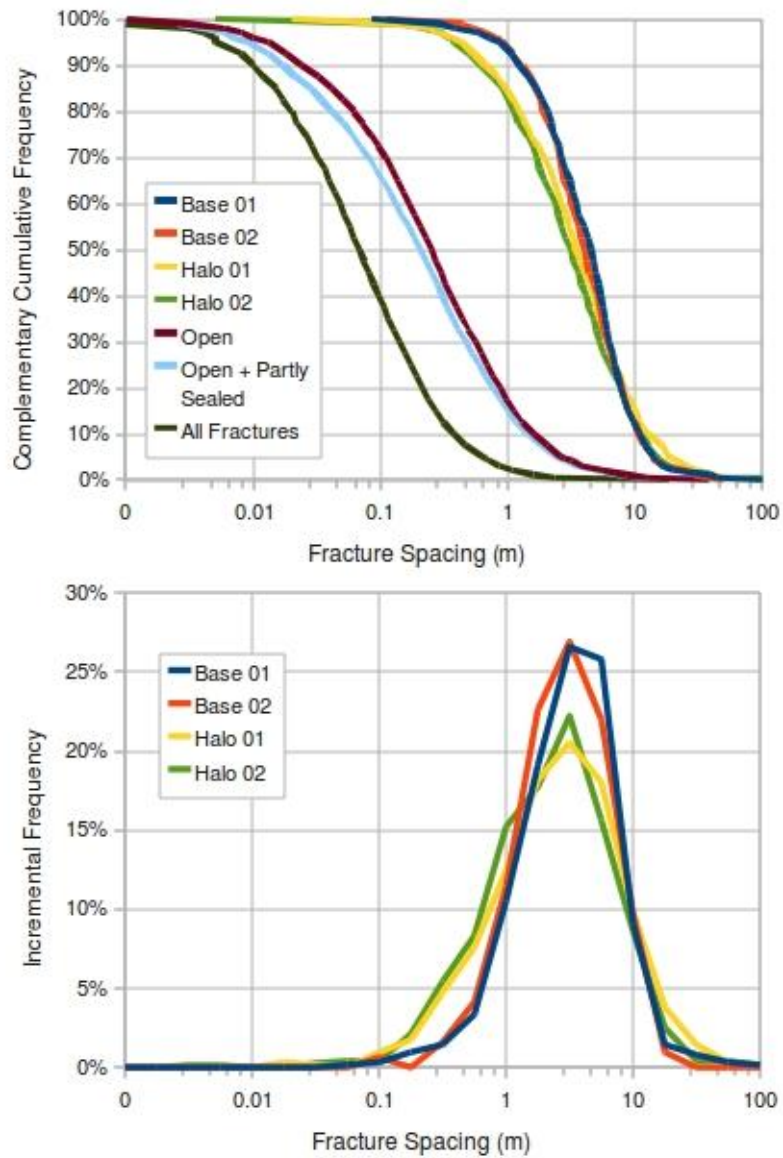
Figure 5.4 Comparison of two realizations of the base case (Poisson process) vs. two realizations of the exponential-halo model in terms of the cumulative and incremental frequency of simulated fracture spacing, for Forsmark fracture domain FFM01. Each data point on the incremental plot represents the fraction of the points that are within a bin covering 1/4 order of magnitude on the logarithmic scale. Also shown for comparison on the first plot are the measured cumulative distributions of fracture spacing in borehole sections that are within FFM01, for three different classifications of these fractures: open fractures only, open fractures plus partly sealed fractures, and all fractures (including sealed fractures).

Discussion

Simulations of borehole sampling in Fracture Domain FFM01 show that the base-case (Poisson) model should be distinguishable from the exponential halo model, for this idealized type of sampling. The main differences are that exponential halo model shows longer intervals of borehole with no conductive fractures, as well as intervals of closely spaced fractures, which at least qualitatively corresponds to a recognized characteristic of the Forsmark site. The possibility that clustering of fractures in the halo model is significant for large-scale connectivity and groundwater flow is explored by site-scale modelling in Chapter 8.

However, simulated borehole sampling for both models shows large discrepancies with actual fracture spacing data from core-drilled holes in FFM01. This is true even when only fractures mapped as "open" are considered. The simulated spacing distribution for the exponential halo model is marginally closer to the curves for the actual data than the simulated spacing distribution for the Poisson model, but the discrepancies are so large for both models that that not much meaning can be attached to this observation.

One explanation for these large discrepancies is the practical necessity to use a finite, minimum fracture size in the simulated sampling. The simulations include only fractures with radii of 0.5 m or larger. According to the fitted power-law model for fracture size, there should be vast numbers of smaller fractures that are still larger than the borehole radius (on the order of 10 cm). This is only partly compensated for by the fact that smaller fractures have lower probabilities of intersecting a borehole.

This appears to be a practical difficulty in comparing borehole data with simulations of borehole sampling. Unless the simulations are extended to include very small fractures down to the scale of 10 cm – which requires much longer computation times -- comparison between actual and simulated datasets in terms of fracture spacing might not be meaningful. Spacing data are also sensitive to the classification of fractures during borehole mapping (i.e. as sealed vs. open), and to the treatment of intensively fractured zones. Mapping of fractures in underground tunnels (considered in the next section of this report) may be a more favourable situation for comparing models to data, since there is the possibility to limit the size range of fractures that enter into spacing calculations.

Based on comparison of borehole sampling simulations to actual borehole data there appears to be no reason to favour the Poisson model over the exponential halo model; if anything, the exponential halo model is marginally better. Thus it appears useful to propagate this model further to analyse its consequences for repository performance.

6. Potential to distinguish alternatives in repository tunnels

This chapter addresses the research question:

- To what extent can data obtained in the repository construction phase reasonably be expected to limit uncertainties with regard to DFN size distributions and spatial/structural relationships among fractures, for the rock at repository depth?

This question is addressed by means of simulated sampling along tunnels based on SKB's most recently proposed repository layout. Comparisons are made with respect to alternative DFN models proposed by SKB (SKB 2008; Munier, 2010), and an additional alternative model (exponential halo model) that is based on the same borehole data analysed by SKB, but which produces stronger clustering of small fractures around major and minor deformation zones.

The method of investigation is based on simulated sampling along tunnels (based on SKB's most recently proposed repository layout) to evaluate the likelihood of being able to discriminate among viable alternative DFN models during the construction phase.

The first stage of analysis tests the potential for underground observations to discriminate between alternative models for the spatial organization of fractures. This is done by sampling fracture intersections along the tunnel axes, and comparing between models in terms of the spacing distribution. From previous work (Geier, 2010d and preceding chapters of this report) this was expected to be an effective way for discriminating between SKB's model based on a Poisson process for fracture location, and a proposed alternative based on the exponential halo model.

The second stage of analysis tests the potential for fracture sampling along tunnel walls to distinguish between alternative assumptions regarding the DFN size distribution. In this case, the comparison is among alternative models that were developed by SKB (SKB 2008; Munier, 2010). The basic procedure was to generate stochastic realizations of the fracture population, calculate the intersections with tunnel walls, and compare the models in terms of the resulting distribution of trace lengths.

Analysis

Linear sampling to discriminate among spatial models

During repository tunnel construction, scan-line mapping will be possible along the direction of the tunnel axes. This will yield linear samples of the fractures, which can be used to evaluate fracture intensity and its inverse, fracture spacing, and then compared with models.

Linear samples of fracture spacing could also be obtained at an earlier stage, prior to excavation of individual tunnels, if pilot holes for the tunnels are drilled and mapped using methods similar to those used for surface-based exploration in core-drilled holes. However, pilot holes on the scale of centimeters will give much less information about the size of the intersected fractures than scan-line mapping on tunnel walls that are one a scale of meters.

These linear samples will differ from the information obtained during surface investigations, in that the directions of sampling will be mainly horizontal, in the plane of the repository, whereas data from surface-based investigations using boreholes is primarily vertical (the ventilation shafts and personnel shafts will provide some vertically oriented samples, but the net length of these shafts within the repository volume will be small compared with the total length of horizontal tunnels).

Another important difference is that the total length of sampling along tunnels will be much larger than the total length of surface-based boreholes in the pre-investigation stage, particularly the fraction within the repository host rock. This implies a larger statistical sample that can be used to discriminate among alternative discrete-fracture network (DFN) models.

To evaluate the possibility for this additional information to allow discrimination among alternative models for fracture clustering, the *fracgen* module of the DFM package (version 2.4.0) was used to simulate linear sampling along the axes of the repository tunnels, according to the layout that SKB has developed for SR-Site. For practical purposes, the tunnel axes were treated as boreholes in order to utilize the existing borehole-sampling algorithm in *fracgen*.

From previous work as described in Chapter 5, this was expected to be an effective way for discriminating between SKB's models based on a Poisson process for fracture location, and a proposed alternative based on the exponential halo model. The ability to assess fracture size (or at least find a lower bound on a scale of meters) from scan-lines on fracture walls could help to avoid the problems that were discussed in the comparison of borehole spacing data with simulated borehole data.

The tunnel coordinates were converted to a sampling program input file consisting of boreholes, using the script *make_tunnelbhs*, which uses an AWK

language script *tunnels_to_samprog.awk* to parse the coordinates into the required format for *fracgen* input.

Stochastic realizations of SKB's base-case GeoDFN model and the alternative (exponential halo) model were then generated, using the table in Appendix 3 of Munier (2010) as the source of parameters for SKB's GeoDFN model (base-case model, "r_0-fixed" model). As a simplification, fracture domain FFM06 was simulated using the same statistics as fracture domain FFM01, so that comparisons could be made between statistically homogeneous domains covering the entire repository.

Only fractures of radius larger than 2.88 m (*i.e.*, the size range considered by Munier (2010) as exceeding the tunnel dimension) were simulated, so the spacing data generated correspond to the spacings between larger (tunnel-scale) fractures. A smaller minimum fracture radius corresponding to a minimum trace length of 0.5 m was tested, but the simulation time and number of fractures generated in the repository volume was found to be excessive. Note that the model includes all fractures, not just the transmissive fractures that would need to be retained for hydrogeological modelling, and the full repository volume considered here is much larger than that modelled by Munier (2010) who considered individual tunnels.

For each model and realization, intersections with the hypothetical boreholes along the tunnels were calculated using the *fracgen* sampling option and stored to a sampling log file. Fracture intensities and spacings along the tunnel axes were then obtained by sorting the sampling log file (by tunnel ID and position).

Figure 6.1 shows examples of the results for the entire repository layout. The cumulative distributions of fracture spacings along tunnel axes for the two different models are compared in Figure 6.2.

Using the Kolmogorov-Smirnov test for comparison of cumulative distributions (Table 6.1), the null hypothesis that the fracture spacing samples are drawn from the same distribution is rejected at a significance level of 0.01(or lower). Thus these two models are expected to be distinguishable with high confidence, based on the quantity of fracture spacing data that can be obtained by scan-line mapping along the repository tunnels.
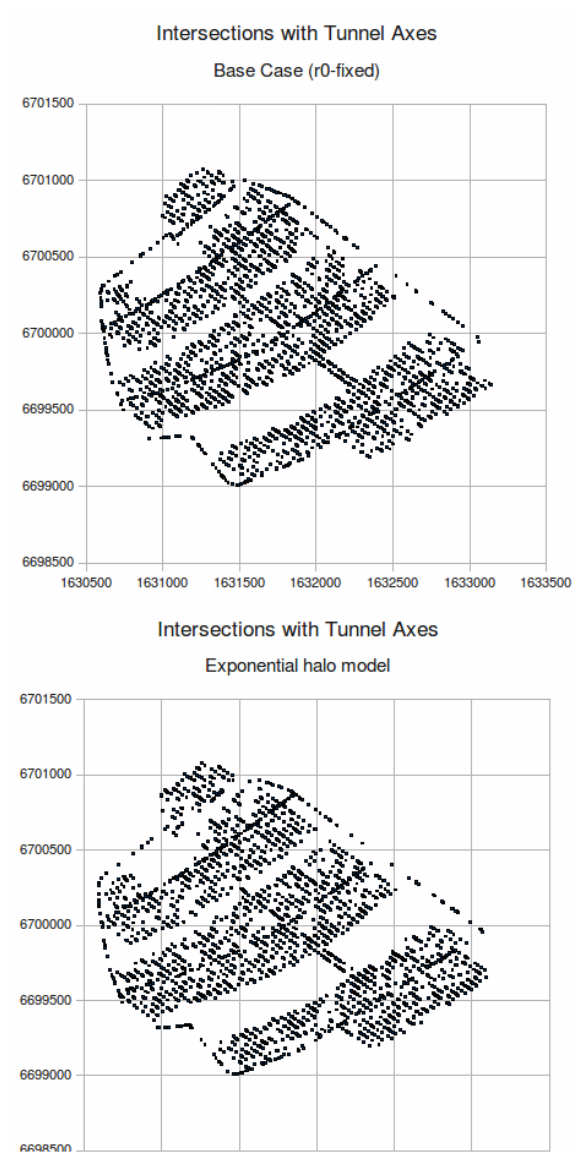
Intersections with Tunnel Axes

Base Case (r0-fixed)

Intersections with Tunnel Axes

Exponential halo model

Figure 6.1 Intersections between pilot holes for the repository tunnel system and fractures (larger than 2.88 m radius), for the base case and exponential halo model.
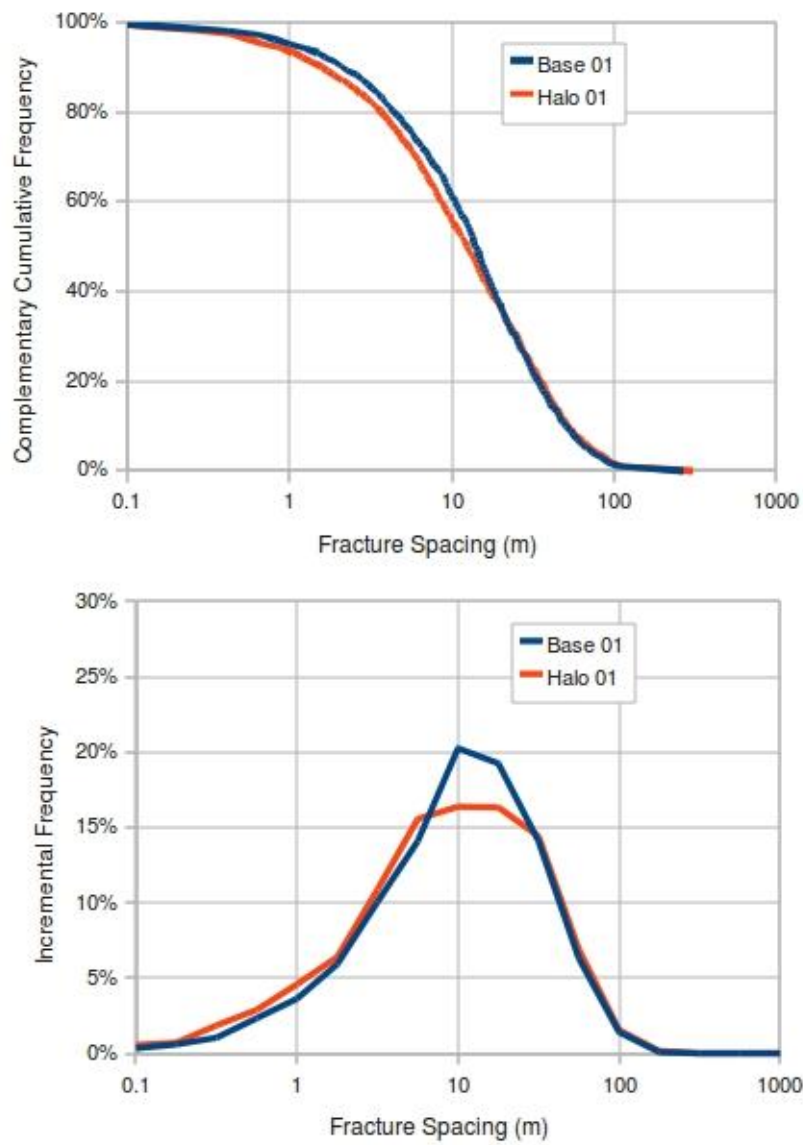
Figure 6.2 Cumulative and incremental frequencies of fracture spacing along tunnels axes in the simulated repository layout at Forsmark, comparing a single stochastic realization of the base case Poisson process, r_0-fixed model (Base 01) with a single realization of the exponential halo model (Halo 01). Each data point on the incremental plot represents the fraction of the points that are within a bin covering 1/4 order of magnitude on the logarithmic scale.

36

Table 6.1 Statistical comparison between the base case (Poisson, r0-fixed) model and alternative (exponential halo) model in terms of spacing of large (radius > 2.8843 m) fractures along the axes of deposition and access tunnels in the repository layout used in SR-Site. The null hypothesis that the two simulated spacing samples are from the same parent distribution is rejected with high confidence.

Calculation case	Poisson (SDM-Site r_0-fixed variant)	Exponential Halo
Realization	1	1
N	2707	2707
Minimum spacing (m)	<0.01	<0.01
1st quartile (m)	5.70	4.79
Median spacing (m)	14.02	12.56
3rd quartile	28.91	29.54
Maximum spacing (m)	265.94	320.68
Kolmogorov-Smirnov statistic D	0.0635	
Kolmogorov-Smirnov probability	3.59E-05	

Area sampling to discriminate among size models

In addition to fracture spacing and fracture intensity data, mapping of fractures along the tunnel walls will also yield fracture trace length distributions which are related to the fracture size distribution. SKB has suggested that these data will help to reduce the acknowledged high uncertainty regarding the fracture size distribution, particularly the frequency of large fractures which is a key uncertainty both for assessing risks associated with earthquake scenarios (*i.e.* possibility for shearing of canisters along large fractures) and for hydrogeologic connectivity.

Since tunnel widths and heights are small compared to the scales for which fractures are regarded as having potential to pose a seismic risk, the question is whether tunnel mapping data will be adequate to distinguish between alternative models for the fracture size distribution.

To address this question, the *fracgen* module of the DFM package was also used to simulate area mapping along tunnel surfaces, within the layout that SKB has developed for SR-Site. For practical purposes, in this step the tunnels were treated as having a rectangular cross-section, with along the two vertical sides, the roof, floor, and two vertical sides.

The tunnel faces were produced using the *repository* module of the DFM package, then converted to a sampling program format with the AWK language script *reptunnels_to_samprog.awk* for *fracgen* input.

Stochastic realizations were produced for all three major variants of SKB's GeoDFN model:

- r_0-fixed (base-case) alternative
- tectonic-continuum (TCM, k_r-fixed) alternative
- outcrop-scale/tectonic-fault (OSM + TFM) alternative

using the table in Appendix 3 of Munier (2010) as the source of parameters. The exponential halo model was also compared, although it was expected to produce similar data to the base case since it uses the same fracture size distribution. As a simplification, fracture domain FFM06 was simulated using the same statistics as fracture domain FFM01, so that comparisons could be made between statistically homogeneous domains covering the entire repository.

Only fractures of radius larger than 2.88 m (*i.e.*, the size range considered by Munier (2010) as exceeding the tunnel dimension) were simulated, so this analysis is focused on the distribution of fracture trace lengths that are on the tunnel scale or larger. Spacing data generated correspond to the spacings between larger (tunnel-scale) fractures.

For each model and realization, the endpoints of intersections with the tunnel mapping surfaces (roof, floor, or walls) were calculated using the *fracgen* sampling option and stored to a sampling log file. Trace lengths were calculated as the Cartesian distance between endpoints on each mapping surface. For traces that intersected more than one mapping surface, the trace length was calculated as the sum of the lengths on the individual surfaces. Thus in the case of a fracture that produces a full-perimeter intersection, the trace length would be calculated as the trace that would be measured all the way around the tunnel's perimeter.

The results for the different models and realizations are summarized in Figure 6.3 and Tables 6.2 through 6.4.

Due to the large number of traces sampled per realization (over 28,000 for all cases), the cumulative density functions for different realizations of a given model are indistinguishable on this plotting scale. Also, as expected, the exponential halo model is indistinguishable from the two realizations of the base case. However, the two alternative models considered by Munier (2010) do yield significant differences both in the numbers of traces in this size range, and in their normalized distribution. Thus data from mapping fracture traces on repository tunnels should be adequate to distinguish among these alternative models for the fracture size distribution.

The peaked form of the incremental frequency plots in Figure 6.3 is apparently real rather than an artefact of bin resolution. The peak frequency is at 5.5 m to 5.6 m for all cases, which is approximately equal to the tunnel diameter. This indicates a dominating influence of observation scale for fracture trace-length distributions in tunnels.
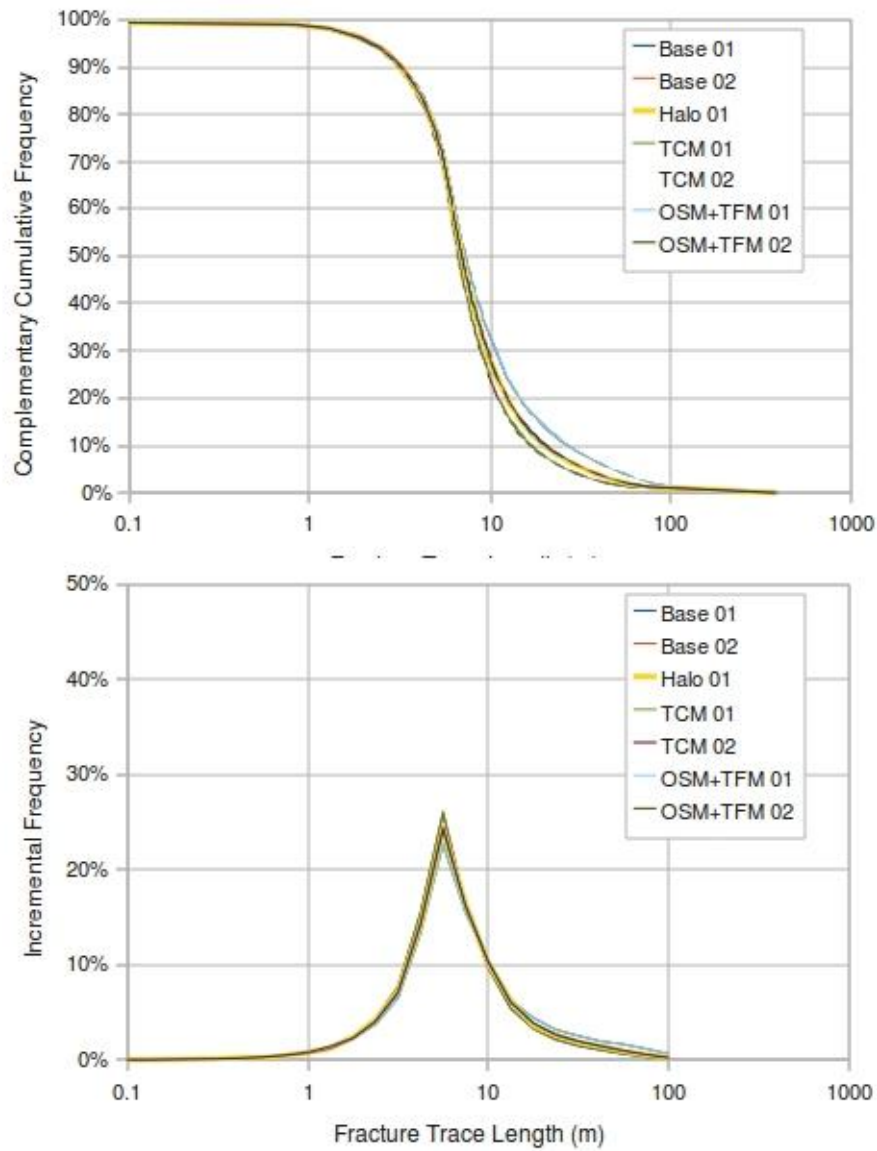
Figure 6.3 Fracture trace length distributions for the simulated repository layout at Forsmark, comparing two stochastic realizations of the base case Poisson process, r_0-fixed model (Base 01 & 02) vs. a single realizations of the exponential halo model (Halo 01), and two realizations each of SKB's alternative tectonic-continuum (TCM 01 & 02) and outcrop-scale/tectonic-fault (TFM 01 & 02) models. Note that the curves for different realizations of a given model are indistinguishable on this scale. Also the curve for the exponential halo model is indistinguishable from the two realizations of the base case. Each data point on the incremental plot represents the fraction of the points that are within a bin covering 1/8 order of magnitude on the logarithmic scale. Note that this is a higher resolution than used in Figure 6.2, in order to check if the sharply peaked form is an artefact of bin size.

39

Table 6.2 Statistical comparisons between two realizations of the base case (Poisson, r_0-fixed) model, and between one realization of this model and the alternative (exponential halo) model, in terms of trace length for large (radius > 2.8843 m) fractures along the deposition and access tunnels in the repository layout used in SR-Site. Parameter values for deformation-zone influenced fracture intensity model for Forsmark fracture domains. The null hypothesis that the simulated trace length samples are from the same parent distribution is accepted with high confidence in both cases.

Calculation case	Poisson (SDM-Site r_0-fixed variant)		Exponential Halo
Realization	1	2	1
N	28997	28821	29000
Minimum trace length (m)	<0.01	<0.01	<0.01
1st quartile (m)	5.09	5.12	5.08
Median trace length (m)	6.97	6.96	6.95
3rd quartile	10.80	10.81	10.76
Maximum trace length (m)	396.94	399.29	386.83
Kolmogorov-Smirnov statistic D	−	0.0053	0.0065
Kolmogorov-Smirnov probability	−	0.81	0.57

Table 6.3 Statistical comparisons between two realizations of the tectonic continuum (TCM), kr-fixed variant base case, and between one realization of this model and one realization of the base-case (r0-fixed) model, in terms of trace length for large (radius > 2.8843 m) fractures along the deposition and access tunnels in the repository layout used in SR-Site. Parameter values for deformation-zone influenced fracture intensity model for Forsmark fracture domains. The null hypothesis that the simulated trace length samples for the two different realizations of the TCM model are from the same parent distribution is accepted with high confidence. The null hypothesis that the simulated trace length samples from the TCM base-case models is rejected with high confidence. Note that the number of intersections is also much higher in the TCM case.

Calculation case	Poisson (TCM k_0-fixed variant)		Poisson (SDM-Site r_0-fixed variant)
Realization	1	2	1
N	117633	117181	28997
Minimum trace length (m)	<0.01	<0.01	<0.01
1st quartile (m)	4.95	4.93	5.09
Median trace length (m)	6.65	6.65	6.97
3rd quartile	9.86	9.81	10.80
Maximum trace length (m)	403.15	326.25	396.94
Kolmogorov-Smirnov statistic D	–	0.0033	0.0438
Kolmogorov-Smirnov probability	–	0.56	3.73E-39

Table 6.4 Statistical comparisons between two realizations of the outcrop-scale + tectonic-fault model (OSM + TFM), and between one realization of this model and one realization of the base-case (r_0-fixed) model, in terms of trace length for large (radius > 2.8843 m) fractures along the deposition and access tunnels in the repository layout used in SR-Site. Parameter values for deformation-zone influenced fracture intensity model for Forsmark fracture domains. The null hypothesis that the simulated trace length samples for the two different realizations of the TCM model are from the same parent distribution is accepted with high confidence. The null hypothesis that the simulated trace length samples from the TCM base-case models is rejected with high confidence.

Calculation case	Poisson (OSM+TFM k_0-fixed variant)		Poisson (SDM-Site r_0-fixed variant)
Realization	1	2	1
N	37390	37575	28997
Minimum trace length (m)	<0.01	<0.01	<0.01
1st quartile (m)	5.26	5.25	5.09
Median trace length (m)	7.30	7.27	6.97
3rd quartile	12.17	12.06	10.80
Maximum trace length (m)	383.47	422.53	396.94
Kolmogorov-Smirnov statistic D	−	0.0060	0.0449
Kolmogorov-Smirnov probability	−	0.51	5.47E-29

Discussion

Simulated sampling of fractures in the planned repository tunnels at Forsmark show that:

1) Fracture spacing data from scan lines along the length of the tunnels should be adequate to distinguish between two alternative models for fracture location (Poisson vs. exponential-halo models).

2) Fracture trace length data from mapping of the tunnel surfaces should be adequate to distinguish among SKB's main alternative models for fracture size distribution.

The second result is obtained despite that the larger fractures that account for most significant differences between these models are generally on a scale larger than the tunnel cross-section. However, it is also noted that the scale of tunnel cross-sections has a dominating effect on the observed distribution of trace lengths.

Additional possibilities for discrimination may be offered by correlating large fractures between tunnels. The additional information to be obtained from this possibility has not been evaluated in the present exercise, but could be assessed by further analysis of the simulated trace maps that were obtained here.

A practical question for review of a repository application is, at what point in excavation in repository excavation would there be sufficient data to distinguish between the two spatial models considered here? Considering the very high confidence levels for a comparison based on the full repository, and considering that the Kolmogorov-Smirnov statistic is a function of the square root of the number of data points, such a conclusion could perhaps be reached after excavating one or two panels (sections) of the repository. A quantitative assessment of this question could be made by supplementary analysis of the data from these simulations.

7. Deposition hole utilization for alternative models

Analysis

Simulation of fracture sets

To evaluate the impact of the alternative (exponential halo) model on the degree of utilization for deposition tunnels, fracture populations simulated with the alternative model were compared with simulations of SKB's GeoDFN model as used by Munier (2010). The GeoDFN model must be used for this comparison rather than the HydroDFN model, as non-transmissive fractures excluded from the HydroDFN model of Follin (2008) can affect utilization due to seismic risk, even if they are not considered to be relevant for hydrogeologic analysis.

The statistical models for the fracture sets were the same as used for simulated borehole sampling, as described in Chapter 5. Here as a base case for reference, we again compare with the r_0-fixed case, which produces the highest degree of utilization according to the calculations by Munier (2010). Calculations are performed only for fracture domain FFM01, which is the main fracture domain that intersects the planned locations of the repository tunnels; the other fracture domain of concern, FFM06, yields similar utilization factors according to Munier (2010).

Figures 7.1 and 7.2 show horizontal cross-sections through the two DFN models, in the plane of the repository. The main qualitative difference is seen as a more heterogeneous distribution of the smaller fractures, in the exponential-halo model, with a tendency toward clustering along larger features, and larger areas of "good rock" with few or no fractures.
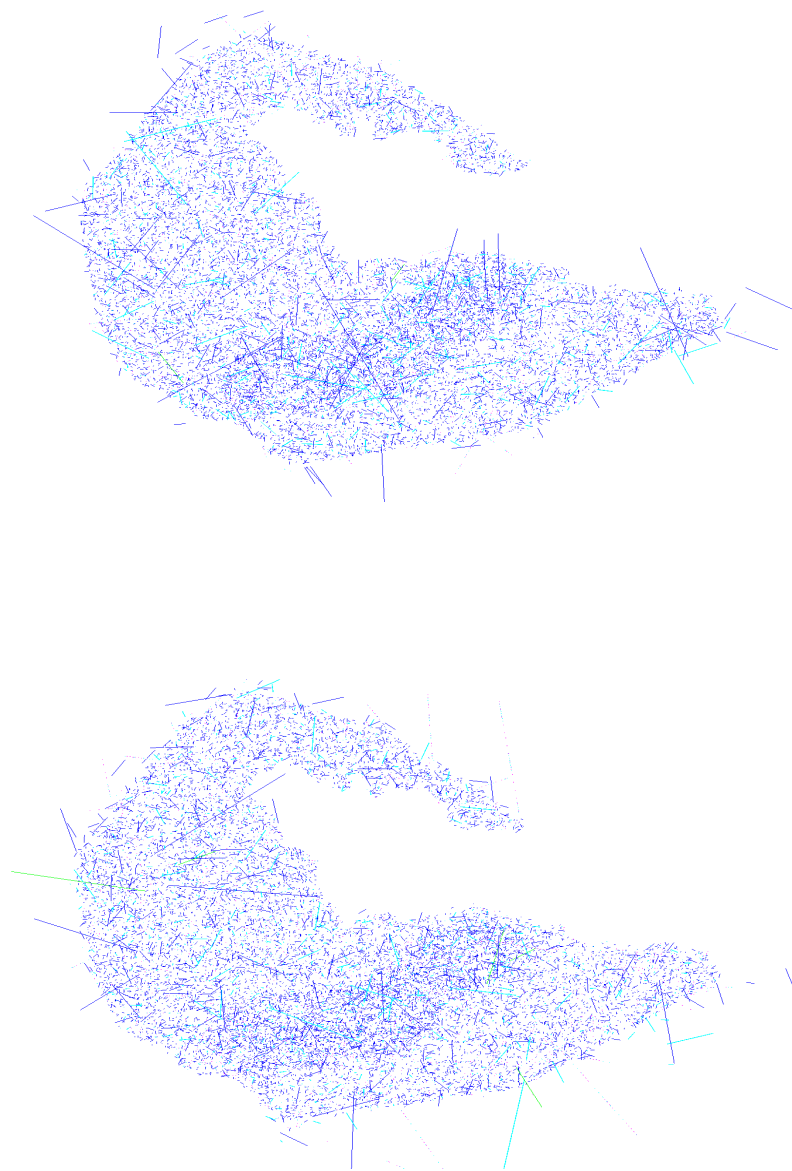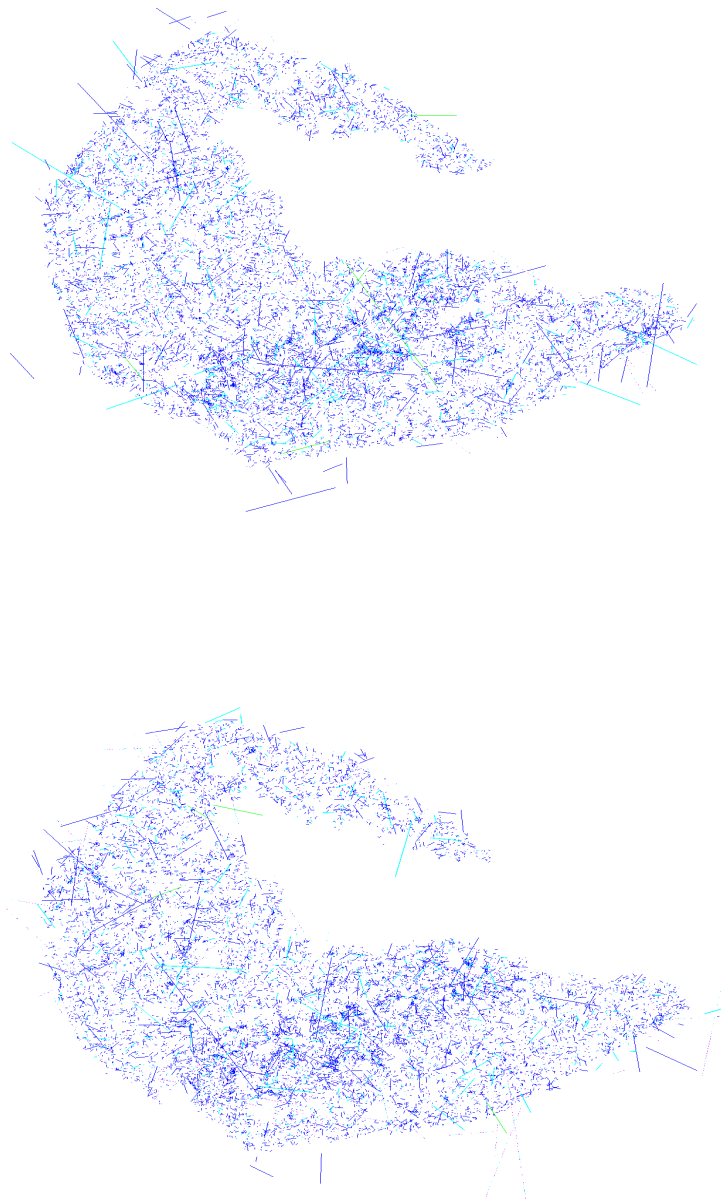
Figure 7.1 Horizontal cross sections through two different realizations of the GeoDFN model for fracture domain FFM01, base case model (Poisson process), in the plane of the repository (z = -468 m). The area of the plots is approximately 4 km x 4 km. The open area in the right-centre part of the cross-section is part of fracture domain FFM06, which is not simulated in this analysis. Colour of fracture traces represents simulated values of transmissivity, for illustrative purposes (note that a transmissivity distribution is not defined for the GeoDFN). Fractures are not truncated at domain boundaries, so some fracture traces extend into other domains (including in the third dimension, outside of this cross-section, which accounts for the few fracture traces that appear to be entirely outside of fracture domain FFM01 in this cross-section).

Figure 7.2 Horizontal cross sections through two different realizations of the alternative exponential-halo DFN model for fracture domain FFM01, in the plane of the repository (z = -468 m). The area of the plots is approximately 4 km x 4 km. Colour of fracture traces represents simulated values of transmissivity, for illustrative purposes (note that a transmissivity distribution is not defined for the GeoDFN).

Utilization of deposition holes

Degree of utilization of deposition tunnels (expressed as a percentage) is defined by Munier (2010) as:

$$DoU = 100\frac{Number\ of\ accepted\ positions}{Planned\ number\ of\ positions}\%$$

Although not explicitly stated by Munier (2010), here the "planned number of deposition holes" is assumed to mean the number of deposition holes that could be placed in a given array of deposition tunnels, taking into account the required spacing between deposition holes due to thermal requirements (a function of rock type), within the total usable length of tunnel which is calculated as:

$$L_{usable} = \sum_i \left(l_i - l_{plug(i)} - l_{end(i)} \right)$$

where:

l_i = length of the ith deposition tunnel

$l_{plug(i)}$ = length reserved for a plug at the entrance to the ith deposition tunnel

$l_{end(i)}$ = Minimum allowable distance from the edge of a deposition hole to the blind end of the ith deposition tunnel.

In the present analysis, it is assumed that $l_{plug(i)}$ and $l_{end(i)}$ are the same for all deposition tunnels, with values as specified for the SR-Can safety assessment:

$l_{plug(i)}$ = 8 m
$l_{end(i)}$ = 20 m

If the minimum allowed spacing s_{min} between canisters is constant (as is specified by the design for a given rock type at Forsmark, according to Munier, 2010), then the degree of utilization can be approximated as:

$$DoU = \frac{N_{accepted}}{\sum_i \text{int}\left(\dfrac{l_i - l_{plug(i)} - l_{end(i)}}{s_{min}} \right)} \approx \frac{N_{accepted} s_{min}}{L_{usable}}$$

where the int() expression is due to the fact that only an integral number of deposition holes can be placed in a given drift, even if a fractional additional length is available. This formula has been used in the present analysis to evaluate *DoU* based on output from the *repository* module.

Tunnel axis coordinates for this analysis were taken from the D2 layout delivery as documented in Section 2 of this memorandum. No distinction was made between tunnels in fracture domain FFM06 vs. FFM01. Hence (since fractures were not simulated in FFM06 at the current stage), the degree of utilization is likely overestimated relative to estimates produced by Munier (2010). Likewise, this analysis only accounts for deposition-hole locations that are excluded based on the full-perimeter-intersection (FPI) criterion, not the extended criterion (EFPC) which also excludes deposition holes that are

intersected by fractures that pass through five or more successive canister positions. Hence it is expected that the utilization estimates produced here will be higher than those of Munier (2010),

The total usable tunnel length for all calculation cases is the same, $L_{usable} = $ 49,494.3 m out of a total deposition tunnel length of 55,290.3 m.

As shown in Table 7.1, the two models produce similar degrees of utilization (compared to the range of variation between realizations), though the mean value for the exponential halo model is about 0.6% higher than for the Poisson model. Thus in terms of utilization, the exponential halo model is essentially the same, or slightly better than the base case.

Note that all results are slightly higher than those obtained by Munier (2010, Figure 7-6). The mean DoU for the two realizations of the base case (r_0-fixed Poisson model) is 94.7%, which about 6.5% higher than the mean DoU for the same model, in the results of Munier (2010). This difference is attributed partly to the fact that no fractures are simulated in FFM06, and partly to the fact that the EFPC criterion was not included. The first factor is estimated to account for an approximately 1.5% increase in DoU (based on the cross-sectional area of FFM06 relative to FFM01 in the repository plane). The second factor can account for a 5% increase in utilization, judging from Munier (2010, Figure 6-2). Thus these differences in method are adequate to explain the quantitative differences with results of Munier (2010). This could be checked explicitly by further simulations that include both fracture domains (FFM01 and FFM06), and applying the EFPC criterion.

Table 7.1 Comparison of Poisson and exponential-halo parameters in terms of degree of utilization.

Calculation case	Poisson (SDM-Site r_0-fixed variant)		Exponential Halo	
Realization	1	2	1	2
Number of rejected positions (FPI criterion)	3477	2290	2588	2490
Degree of utilization	93.51%	95.93%	95.26%	95.49%

Discussion

Utilization factors obtained for the base-case DFN model are approximately the same as those obtained by Munier (2010) for the same DFN model, after accounting for omission of fracture domain FFM06 and the EFPC criterion in the current work. The alternative, exponential-halo model produces utilizations factors that are slightly higher (based on an average of two realizations), but the difference is of the same magnitude as variability between stochastic realizations.

Thus the alternative model does not imply any adverse effects on the repository, in terms of degree of utilization. The key question remaining is whether the alternative models is significant for large-scale connectivity. Site-scale hydrogeologic modelling will be needed to check this possibility.

8. Comparison in terms of flow and transport

This chapter describes flow and transport calculations based on a simplified and updated version of the Discrete Feature Model (DFM) of the Forsmark candidate repository site. This DFM model was developed from an earlier DFM model (Geier, 2010a), which was based on SKB's SDM-Site site descriptive model of Forsmark (SKB, 2008). Flow and transport calculations using this model provide an additional basis for comparisons of alternative concepts of the fracture statistical model around the repository.

The key simplifications in this model, as described in detail by Geier (2010b), include:

- Increased spacing (reduced resolution) of effective-conductivity grid features to represent the rock mass away from repository tunnels;
- Reduced resolution of the topographic surface;
- Simplified geometry of the large-scale deformation zones;

These calculations also use the new, D2 repository layout at the 465-468 m level, which is expected to form the basis for SKB's safety assessment calculations in SR-Site.

The results for this updated, simplified DFM model are presented in terms of the calculated hydraulic heads for various cross-sections through the model, distributions of flow rates to deposition holes, and advective-dispersive particle trajectories from deposition holes.

Modelling approach

The main steps in formulating and applying the discrete-feature model are essentially the same as those described for the previous DFM model based on SDM-Site data (Geier, 2010a):

- Adaptation of deterministic features (topography, deformation zones, and shallow-bedrock aquifer);
- Simulation of stochastic features (DFN-scale fractures);
- Adaptation of repository tunnels and deposition holes to stochastic features;
- Assembly of finite-element mesh representing all classes of features;
- Flow simulations;
- Advective-dispersive tracking of particles released from deposition holes.

These steps are described in the following sections.

Deterministic features

Topography

A DFM representation of the topographic surface was derived from SKB data delivery Elevation data 090821, after conversion to ESRI raster format by Geosigma AB, then converting to DFM panel format. The resolution of the topographic feature was 200 m. The resulting surface feature (based on the elevation data) is shown in Figure 8.1.

Figure 8.1 Surface feature for Forsmark after discretization, colored to show topographic/bathymetric eleva-

tions. Note that in this dataset, elevation data are missing from the NW portion of the area (west of the island of Gräsö) but this is outside the modelled region. The area of this plot covers RAK 1619990.000 E, 6714990.000 N (NW corner) to RAK 1649990.000 E, 6684990.000 N (SE corner). Triangles are 200 m high by 200 m wide, with additional refinement where the topographic surface intersects deformation zones. The area covered by the DFM model for flow and transport calculations is the rectangular area bounded by white. The colour scale represents elevation with respect to mean sea level as follows: dark blue, below -13.3 m; medium blue, -13.3 m to -6.7 m; pale blue, -6.7 m to 0 m; green, 0 m to +6.7 m; yellow, +6.7 m to +13.3 m; red, above +13.3 m.
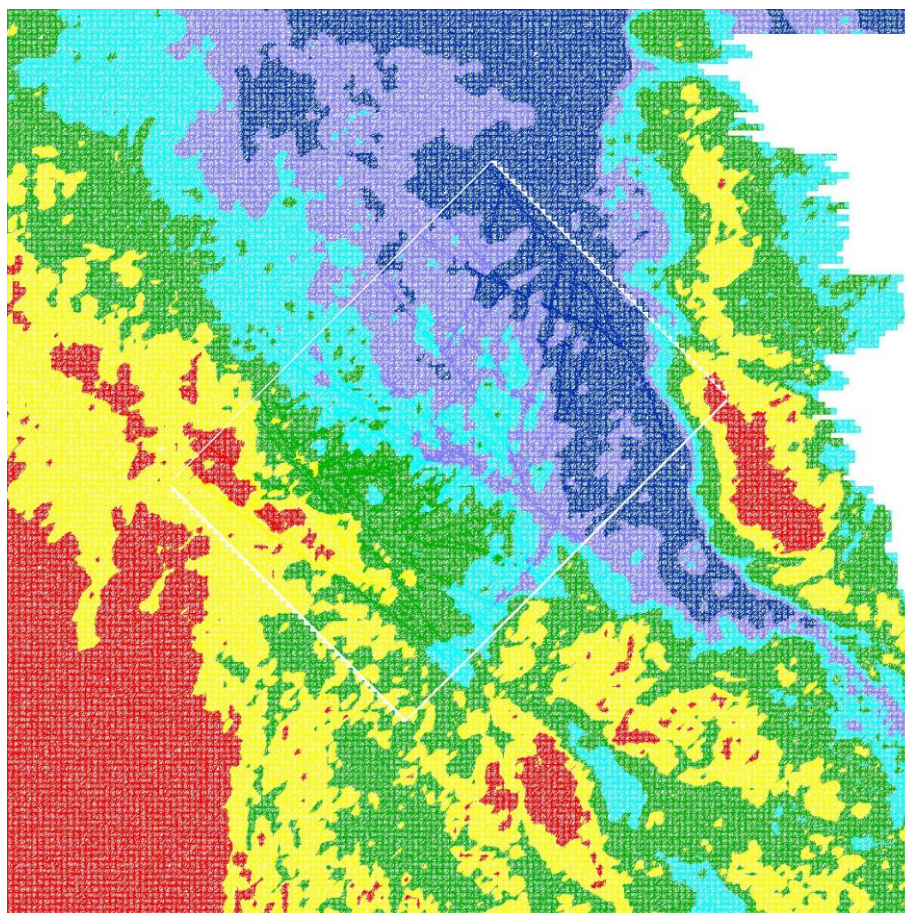
Deformation zones

Deformation zone geometry for the base case is based on SKB's May 2010 data delivery of deformation zone geometry (single-sided) as documented in Chapter 2. The files for local and regional deformation zones were translated to AutoCAD DXF format (by Geosigma AB), then converted to DFM panel files to represent the geometry of these features in the DFM model (Figures 8.2 and 8.3).

A variant of this sub-model that was used for some preliminary runs was based on an earlier SKB data delivery skb#09_04 (0:4) which had "double-sided" features (more properly, bounding surfaces enclosing the tabular volumes of the deformation zones, but appearing as double surfaces in some views, Figure 8.4).

In both cases, the provided data included truncated versions of some regional deformation zones within the local-scale model. These were deleted prior to mesh assembly, so that only the more extensive, regional-scale versions of these same deformation zones were included.

Also in both cases, conditioning to improve the triangulations of the surfaces defining deformation zones was done prior to mesh assembly. Details of the conditioning method are described by Geier (2010b).
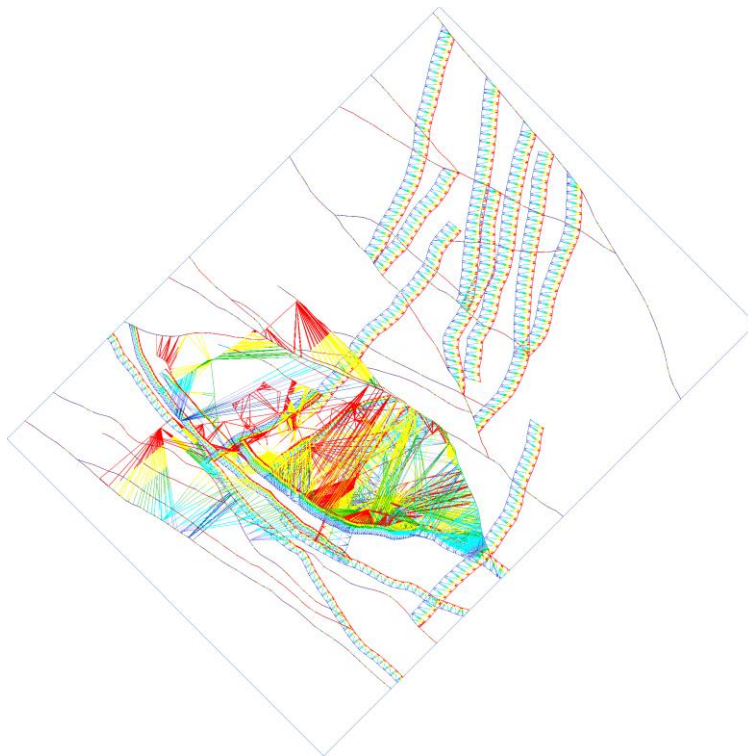
Figure 8.2 Plan view of triangular facets that form the boundaries of regional-scale deformation zones in the SDM-Site structural geological model (colour scale indicates elevation, ranging from deep blue at -2000 m to red near the ground surface).

Figure 8.3 Plan view of triangular facets that form the boundaries of the local-scale deformation zones in the SDM-Site structural geological model (colour scale indicates elevation, ranging from deep blue at -2000 m to red near the ground surface).
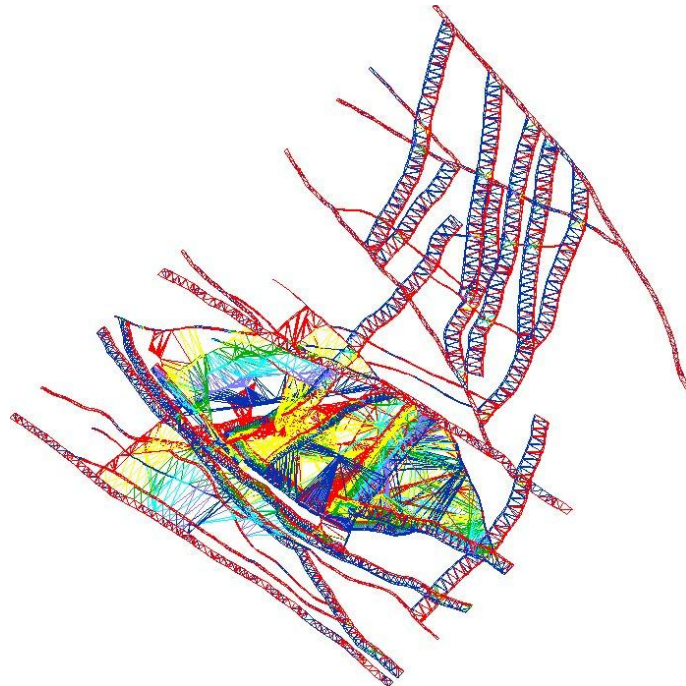
Figure 8.4 Plan view of triangular facets that form the boundaries of the "double-sided" deformation zones in the SDM-Site structural geological model, used for preliminary variants of the discrete feature model. Colour scale indicates elevation, ranging from deep blue at -2000 m to red near the ground surface.

Shallow bedrock aquifer

Three horizontal features are included to represent a "shallow bedrock aqui-fer" as suggested by Follin *et al.* (2008). These are placed at z = -25 m, z = -75 m, and z = -125 m. This implementation differs from SKB's in that the shallow bedrock aquifer features are at constant depth rather than parallel to the topography, and in that these features are rectangular in plan view (Table 8.1 and Figure 8.5). The coordinates are chosen to cover the same approxi-mate area as in SKB's model, and limit these features to an area in which they cannot outcrop. Differences due to this representation are expected to be minor.

Table 8.1: Corners of area covered by Forsmark shallow bedrock aquifer (RAK coordinate system). These coordinates are implemented in the DFM panel file FM23BedrockAquifer.pan.

Corner	X (easting)	Y (northing)
Southwest	1630000	6699000
Southeast	1633500	6699000
Northeast	1633500	6701500
Northwest	1630000	6701500
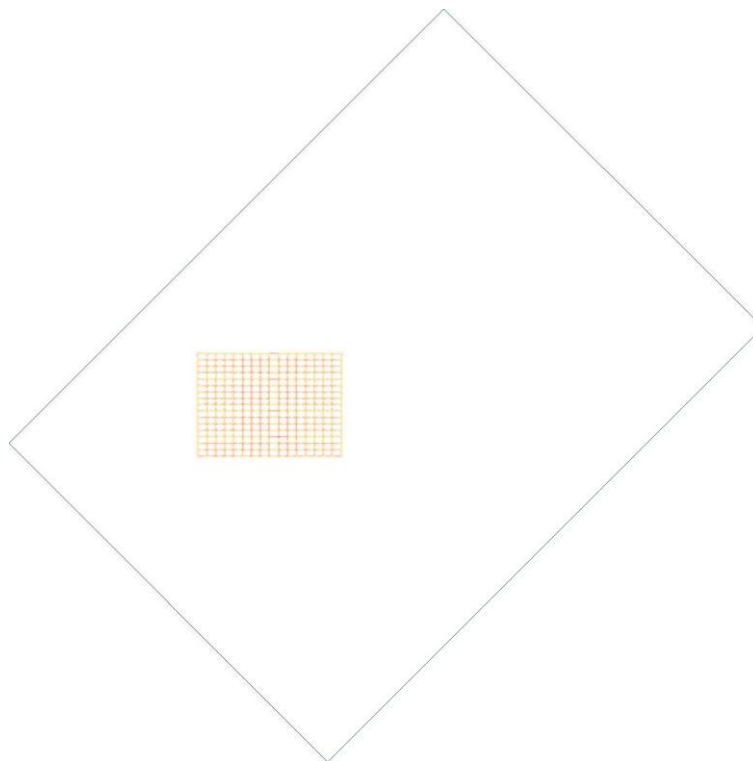
Figure 8.5 Plan view showing the uppermost feature of the shallow bedrock aquifer, relative to the regional model boundary. The two deeper features are directly below this one.

Regional conductivity grid

During this project it was observed that the regional deformation zone model has very poor connectivity in the SW-NE direction, in particular, but also in other directions because, outside of the fracture domains, no background conductivity is specified. To remedy this situation, an orthogonal lattice of planar transmissive features was introduced outside of the local portion of the site descriptive model (Figure 8.6). These features are intended, on a very coarse scale, to represent the background hydraulic conductivity of the rock excluding the regional deformation zones which are represented explicitly in the discrete-feature model.

The vertical features in this lattice are spaced 1500 m apart in the SW-NE direction and the SE-NW direction, with a rectangular gap around the local-scale portion of the model. The uppermost horizontal feature in the lattice is at 375 m below sea level. From there down to 3000 m below sea level, the horizontal features were spaced at even intervals of 375 m. This lattice of features is referred to as the "regional conductivity grid" or "regional K-grid" in this report, for the sake of brevity.
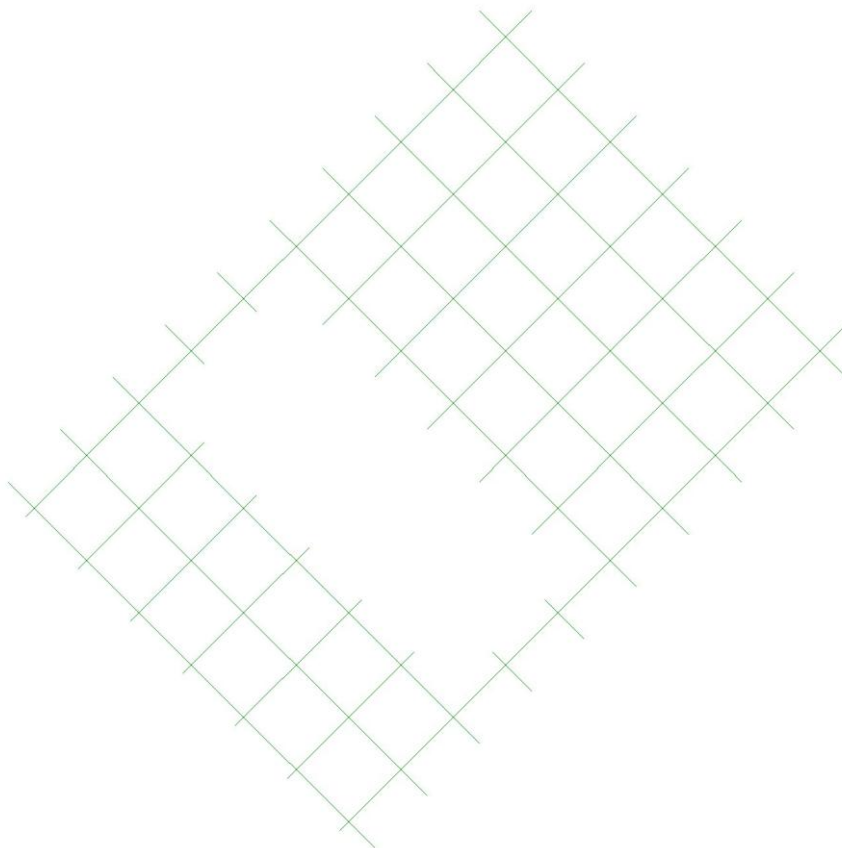
Figure 8.6 Plan view of orthogonal lattice of regional conductivity features ("regional K-grid").

Hydraulic properties of deterministic features

Surface feature

Base case: Transmissivity of this feature is uniformly set to $T = 10^{-5}$ m^2/s, and aperture is set to $b_T = 1$ cm. This transmissivity is chosen as a very rough value to represent the net transmissivity of the uppermost fractured bedrock, together with Quaternary deposits which are discontinuous over the site and vary in thickness and hydraulic conductivity. For comparison, the parameterization of these layers in the model of Bosson et al. (2008) yields an effective that varies from about $T = 2.5 \times 10^{-5}$ m^2/s in areas where coarse till is present, to about $T = 0.8 \times 10^{-5}$ m^2/s where till is absent. The aperture value for this layer has no effect on simulations since it affects only particle tracking to simulate solute transport, and particles are considered to discharge when they reach this feature.

Variants: None were evaluated. Regolith data have not been used in the present study, but could be used to assign spatially varying hydraulic properties.

Shallow bedrock aquifer

Base case: Finite elements derived from panels belonging to the shallow-bedrock aquifer are assigned transmissivity values equal to the closest borehole measurement point for the corresponding depth intervals in Table 3-11 of Follin et al. (2008).

Variants: None were evaluated.

Regional conductivity grid

Base case: Properties of the "background" rock on the regional scale are not clearly defined in the Site Descriptive Model for Forsmark (SKB, 2008). Follin et al. (2007) recommended a simplified approach using homogeneous properties based on water-supply well yields, which appears to have been implemented in the model presented by Bosson et al. (2008). Here for the DFM model, regional background hydraulic conductivity tensor components are assumed to be:

$$K = \begin{bmatrix} 1 & 0 & 0 \\ 0 & 1.1 & 0 \\ 0 & 0 & 1.1 \end{bmatrix} 10^{-9} \, m/s$$

where the principal directions are aligned with the NW-SE, SW-NE, and vertical directions. The magnitude is based on the range used by Bosson et al. (2008, p. 20-21 and Figure 2-6). The increase by a factor of 1.1 in the SW-NE and vertical

directions is simply to avoid numerical problems that can arise in solving for the equivalent transmissivity values to the panels that represent these features in the regional K-grid. Equivalent transmissivities are calculated based on the spacing of 1500 m and taking into account the fact that two sets of panels normally contribute to flow in a given principal direction; this yields panel transmissivities that are nominally equal to 7.5×10^{-7} m^2/s.

Variants: None were evaluated.

Deformation zones

Base case: Hydraulic properties for the deformation zones were assigned in essentially the same manner as described by Geier (2010a), following the algorithm described below. For the base case using single-surface deformation zones, transmissivities were used directly (i.e. without dividing by two), consistent with the single-surface representation.

Variants: For the preliminary variants using double-surface deformation zone geometries, the transmissivities and effective apertures were divided by a factor of two.

Hydraulic properties for the deformation zones in the base-case model were assigned based on SKB's Hydraulic Conductor Domain (HCD) model as described on p. 85 of SKB R-08-95 (Follin, 2008):

$$T(x, y, z) = \overline{T}_0 10^{z/k + N\left(0, \sigma_{\log T}\right)}$$

where:

$k = 232.5$ m
$\sigma_{\log T} = 0.632$

and where $\overline{T}_0$ is the geometric mean of the values of T_0 calculated as:

$$T_{F0_i} = T_F(z_i) 10^{-z_i/k}$$

giving:

$$\overline{T}_0 = \sqrt[n]{\prod_{i=1}^{n} T_F(z_i) 10^{-z_i/k}} = 10^{-\overline{z}/k} \sqrt[n]{\prod_{i=1}^{n} T_F(z_i)}$$

where $\overline{z}$ is the mean z coordinate for the measurements in the zone.

The effective transport aperture b_T and storativity S are assumed to be correlated to transmissivity as:

$$b_T = 0.5 \, T^{0.5}$$

$$S = 7 \cdot 10^{-4} T^{0.5}$$

consistent with Eq 8-9 and 8-11 in SKB R-05-18, which according to that report are based on analyses for modelling of the Äspö Hard Rock Laborato-

57

ry (Note that in SKB R-06-98, p. 58, the above expression is used for fractures in the hydraulic rock domains but it is increased by a factor of 10 for HCDs). These properties were assigned after mesh assembly and discretization.

For each borehole intercept x_i with a deformation zone, values of transmissivity $T_F(x_i)$ were taken from Table C1 of Follin *et al.* (2008) and assigned coordinates in the reference system based on borehole and deformation zone geometry. Values of T_0 are then calculated from these results.

For 60 of the deformation zones that are included as HCDs in the regional or local model, no transmissivity data are available from intersections with boreholes from the site characterization programme. These HCDs are assigned generic values of $T_0 = 1 \times 10^{-6}$ m^2/s.

Two other deformation zones are intersected by boreholes but transmissivity values were not included in Table C1 of Follin *et al.* (2008). One of these, ZFMNNW0404, is given the same generic value. The other, ZFMENE1061B, is assigned the same value used for the related zone ZFMENE1061A. Details are given by Geier (2010a).

Stochastic fractures

Stochastic fractures in the DFN portion of the model are generated within fracture domains based on statistical models for various fracture sets. Stochastic simulation is used to generate realizations of the fracture population, which are identified by the seed value used to initialize the random number generator for a given realization (01, 02, etc.).

A realization of all fractures on scales of more than a few centimetres, for the entire volume of the model, would require prohibitively large computer memory and run times. Therefore only the larger and more transmissive fractures are simulated explicitly, as a function of distance from the deposition tunnels, using the concept of "generation shells" as described in the DFM user documentation (Geier, 2008). The remainder of the fractures are considered to contribute to the background hydraulic conductivity, which is represented by a lattice of orthogonal features (local-scale conductivity grid).

Fracture domains

Fracture domain boundaries are based on SKB Data Delivery skb#09_04 (0:4), translated to AutoCAD DXF format as FD_PFM_v22.01 basemodel_joel (file translated by Geosigma), and subsequently converted to polyhedral domains in the required DFM input format, as described by Geier, 2010ab). Subdomains for different depths as specified in Table C-1 of SKB R-08-95 (Follin, 2008) were defined by clipping the polyhedral domains as detailed in Table 8.2.

Table 8.2 Definition of fracture sub-domains by depth. Note that the depth ranges for sub-domains in FFM06 are the same as for FFM01, and the depth ranges for sub-domains in FFM04 and FFM05 are the same as for FFM03.

Fracture Domains	Depth Sub-domain	*fracgen* clipping commands
FFM01 and FFM06	shallow	clipped below -200
	middle	clipped above -200 clipped below -400
	deep	clipped above -400
FFM02	shallow	(*none needed as FFM02 only exists above –200 m*)
FFM03, FFM04 and FFM05	shallow	clipped below -400
	deep	clipped above -400

Fracture set definitions

Each fracture set is defined in terms of a location model (Poisson process for the base case), a volumetric intensity P_{32}, an orientation distribution, a distribution for fracture size (radius), and distributions or correlation models for fracture hydraulic properties (transmissivity and aperture being the properties of concern for the steady-state flow models considered here).

Base case: Fracture set statistics for the base case are taken from the HydroDFN model as given by Follin (2008).

Halo model: Fracture sets for the exponential-halo model are developed as a modification from the base case, by splitting the fracture sets into separate sets according to fracture radius ($r > 100$ m and r < 100 m), as was done for the implementation of an exponential-halo variant of the GeoDFN in Chapters 5-7.

For all variants, a significant difference from previous implementations was that the power-law exponent in the DFM model was set to $b_r = k_r + 1$, where k_r is the power-law exponent used by Follin (2008). This was based on a new understanding of a difference in the mathematical notation used in SKB's models, versus that used in the DFM user documentation (Geier, 2008).

59

Fracture generation shells

The DFN sub-model would contain many millions of fractures if it were explicitly represented over the entire domain of the site-scale model, and this would lead to an intractably large network problem for numerical solution. In order to reduce the complexity of the problem, an equivalent conductivity grid composed of a lattice of orthogonal features is used to represent the contribution of smaller-scale fractures to large-scale flow.

The rules for retaining fractures as a function of distance from the deposition area are described in the DFM model in terms of "shells." Within each shell (range of distances from the deposition tunnels), fractures that should be represented explicitly in the model are identified as a site-specific function of fracture size, fracture transmissivity. The distance from a fracture to the deposition area is evaluated as d_{min}, the minimum three-dimensional distance from any point on the fracture to any point on a polygon in the plane of the repository, which circumscribes one of the deposition panels (Figure 8.7). Successively smaller and/or less transmissive fractures are retained explicitly for smaller values of d_{min}.

d_{min}(Fracture 1)

d_{min}(Fracture 3)

Polygon enclosing repository panel.
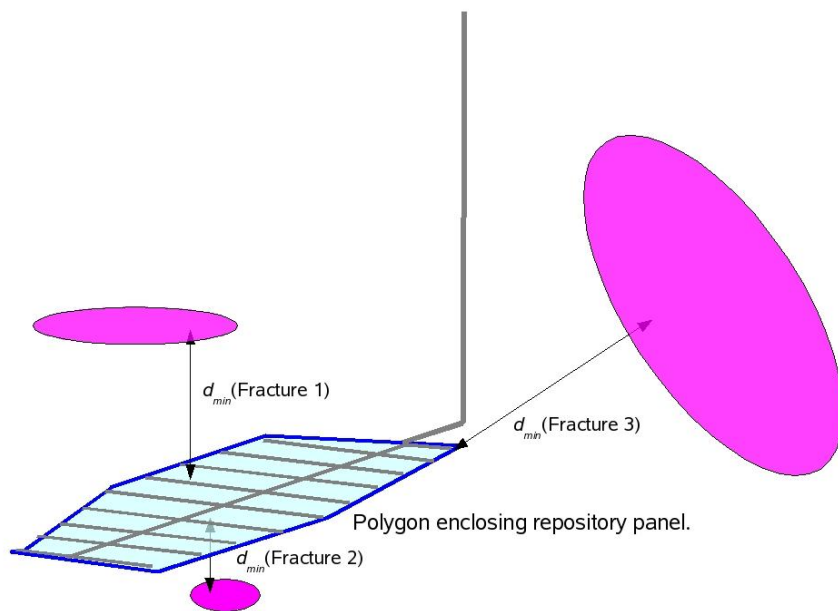
d_{min}(Fracture 2)

Figure 8.7 Illustration of the minimum distance d_{min} from a given fracture to the polygon enclosing a repository panel in the horizontal plane, which is used as criterion for deciding which fractures should be retained explicitly in the model, versus which fractures should be represented in terms of aggregate block-scale properties.

Two different sets of shell specifications were treated as variants: a base case and a "sparse" variant which retains fewer of the small-radius and low-transmissivity fractures in each shell. The shell specifications for these two cases are listed in Table 8.3.

Fractures that are not retained explicitly in the model are represented by their contribution to the equivalent conductivity of a regular grid of features, as described under the next heading below.

Table 8.3 Rules for explicitly retaining fractures of a given radius r_f and transmissivity T_f when d_{min} is the minimum distance from any point on the fracture to the polygon enclosing the portions of the repository being modelled. Note that no fractures are retained in the distance range specified for Shell 1, as the indicated values of r_f and T_f are never exceeded by the DFN statistical model. Shells are specified in terms of distance (shell radius) relative to polygons covering the area of the deposition tunnels at 468 m depth.

Shell	Distance range	Base case		Sparse variant	
		Retain if r_f is greater than:	and T_f is greater than:	Minimum fracture radius (m)	Minimum fracture transmissivity (m^2/s)
1	500 m < d_{min} ≤ 50000 m	10000 m	1x10^{10} m^2/s	10000 m	1x10^{10} m^2/s
2	200 m < d_{min} ≤ 500 m	100 m	1x10^{-12} m^2/s	250 m	1x10^{-5} m^2/s
3	100 m < d_{min} ≤ 200 m	50 m	1x10^{-12} m^2/s	100 m	3x10^{-6} m^2/s
4	50 m < d_{min} ≤ 100 m	20 m	1x10^{-12} m^2/s	50 m	1x10^{-6} m^2/s
5	20 m < d_{min} ≤ 50 m	10 m	1x10^{-12} m^2/s	20 m	1x10^{-7} m^2/s
6	10 m < d_{min} ≤ 20 m	5 m	1x10^{-12} m^2/s	10 m	1x10^{-8} m^2/s
7	5 m < d_{min} ≤ 10 m	3 m	1x10^{-12} m^2/s	5 m	1x10^{-9} m^2/s
8	d_{min} ≤ 5 m	1 m	1x10^{-12} m^2/s	2 m	1x10^{-10} m^2/s

Local-scale equivalent conductivity grid

Fractures that are not represented explicitly in the model are considered to contribute to the 3-D hydraulic conductivity tensor **K** of the rock block that contains them. The contribution of each fracture to the block-scale tensor **K** is calculated by the method of Snow (1969), which is defined for infinite fractures, normalized for the finite area of the fracture in relation to block volume.

Each rock block is then represented in the discrete-feature model by a set of three orthogonal features, which are divided into patches of different properties as illustrated in Figure 8.8. The transmissivities of the patches on the features that reproduce the diagonal components of the hydraulic conductivity tensor K_{11}, K_{22}, and K_{33} are calculated by an inverse method. Block-scale porosity is calculated as a scalar property by adding up the contributions due to the transport aperture and areas of individual fractures.

The resulting lattice of orthogonal features is referred to here as the local-scale equivalent conductivity grid (referred to for brevity as "local K-grid"). For mathematical details of this approach and a discussion of the simplifications and their consequences, see Geier (2008a,b).
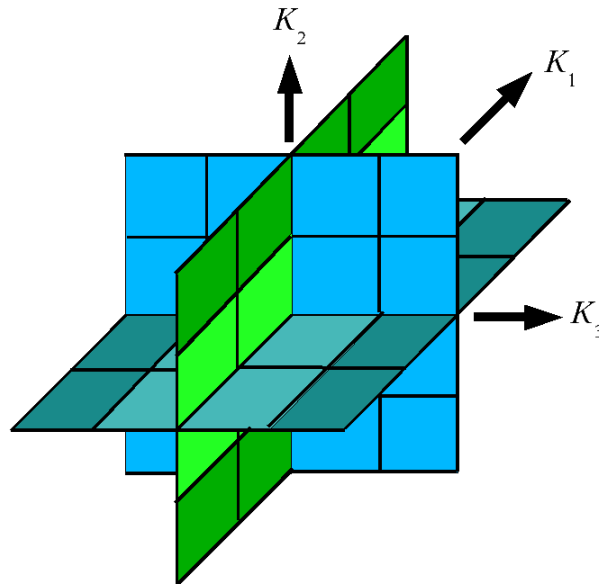
Figure 8.8 Representation of a rock block by three orthogonal features to represent block-scale hydrologic properties in the discrete-feature conceptual model.

The local K-grid covers the rectilinear domain bounded by:

- East side at X = 1 638 000 (RAK E)
- West side at X = 1 627 000 (RAK E)
- South side at Y = 6 697 000 (RAK N)
- North side at Y = 6 703 000 (RAK N)
- Upper boundary at Z = 30 m.a.s.l.
- Lower boundary at Z = -2 000 m.a.s.l.

A grid spacing of 500 m in the X (E-W) and Y (N-S) directions is used to separate the vertical panels that are used to represent block-scale hydraulic conductivity components. The spacing in the Z (vertical) direction is variable, with cell boundaries at -2000 m, -1500 m, -1000 m, -750 m, -520 m, -420 m, -260 m, -120 m, and 30 m.a.s.l. An example is shown in Figure 8.9.
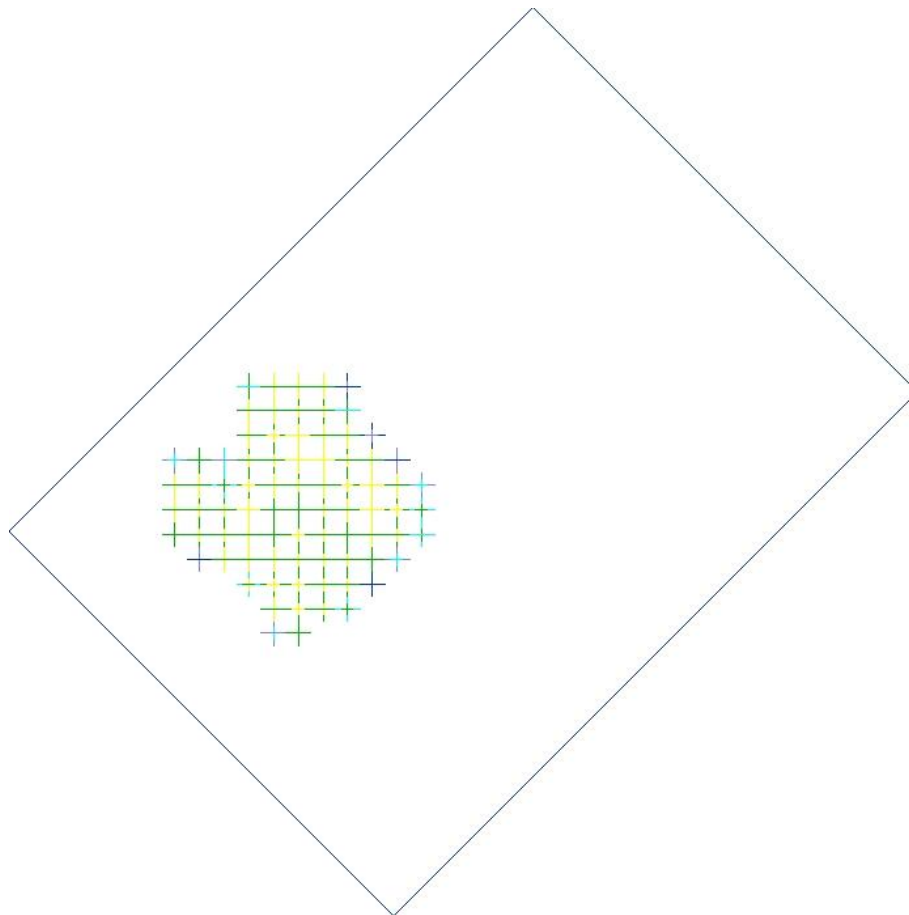
Figure 8.9 Plan view of the block-scale equivalent features representing fractures removed from the stochastic DFN portion of the model around the repository, for one realization of the base case. Fracture transmissivity is indicated by the colour scale, ranging from dark blue ($T_f < 10^{-10}$ m^2/s) to red ($T_f > 10^{-4}$ m^2/s). For blocks that contain no transmissive fractures from the DFN realization, the block-scale equivalent features are omitted.

Repository features

Primary data for the repository layout at the new 468 m nominal depth were obtained in SKB delivery 2010-06-02. The layout is three-dimensional in that transport and deposition tunnels axes are inclined, rather than horizontal. Due to limitations of the DFM *repository* module (Version 2.4.0), the inclined tunnels are represented as perfectly horizontal in the current DFM model, with tunnel floor at -465 m. This results in vertical errors in tunnel position of up to 3 m, depending on lateral position within the repository. The configuration of the tunnels in the model is shown in Figures 8.10 and 8.11.

Features to represent the disturbed-rock zone (DRZ) around repository transport tunnels and deposition tunnels, and the deposition holes, are produced by conditional simulation for a given realization of the DFN component, using parameters as listed in Table 8.4. An example of the resulting positioning of deposition holes along the tunnels is shown in Figure 8.12.
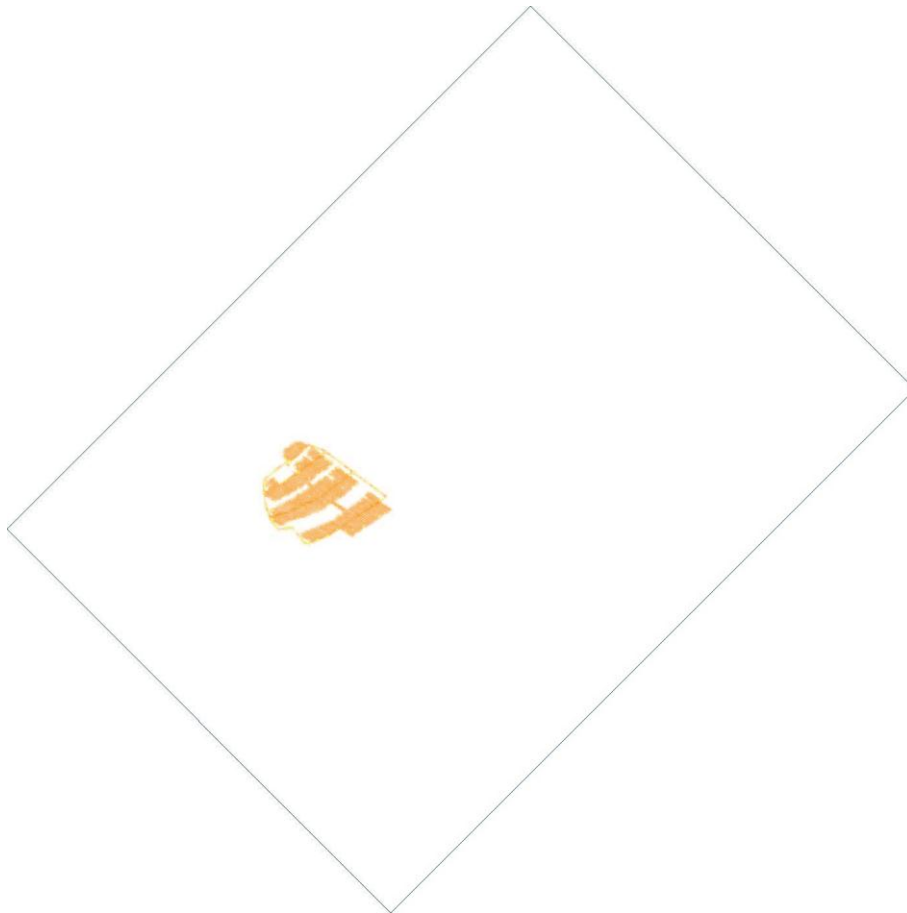
Figure 8.10 Plan view of repository layout with respect to the regional model boundary.

Table 8.4 Deposition hole parameters for the model.

	Parameter value	Justification
Deposition hole sides	6	Hexagonal approximation to circle
Deposition hole radius	0.88 m	SR-Can Initial State Report (SKB TR-06-21), Figure 5-3
Deposition hole depth	7.83 m	SR-Can Initial State Report (SKB TR-06-21), Figure 5-3
Canister radius	0.53 m	SR-Can Initial State Report (SKB TR-06-21), Figure 5-3
Canister length	4.83 m	SR-Can Initial State Report (SKB TR-06-21), Figure 5-3
Canister top	2.5 m	SR-Can Initial State Report (SKB TR-06-21), Figure 5-3
Distance between holes $L_{spacing}$	7.8 m	Based on D1 repository design (Brantberger et al., 2006)
Distance from drift end	20 m	Deep Repository, Underground Design Premises D1/1 (SKB R-04-60)
Distance from drift start L_{plug}	8 m	Deep Repository, Underground Design Premises D1/1 (SKB R-04-60)
Minimum step distance L_{step}	1 m	Assumed generic value
Pilot hole transmissivity	1×10^{-5} m^2/s	Assumed generic value
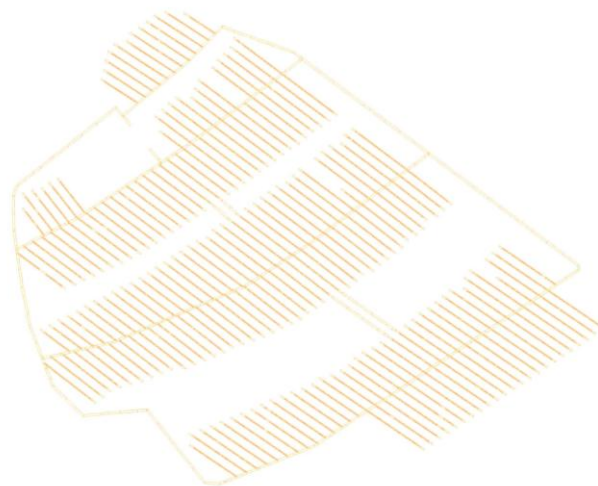
Figure 8.11 Plan view of repository layout (plot of area within a 3 km square area from X = 1630500 m, Y= 6698500 m to X = 1633500 m, Y = 6701500 m).

65
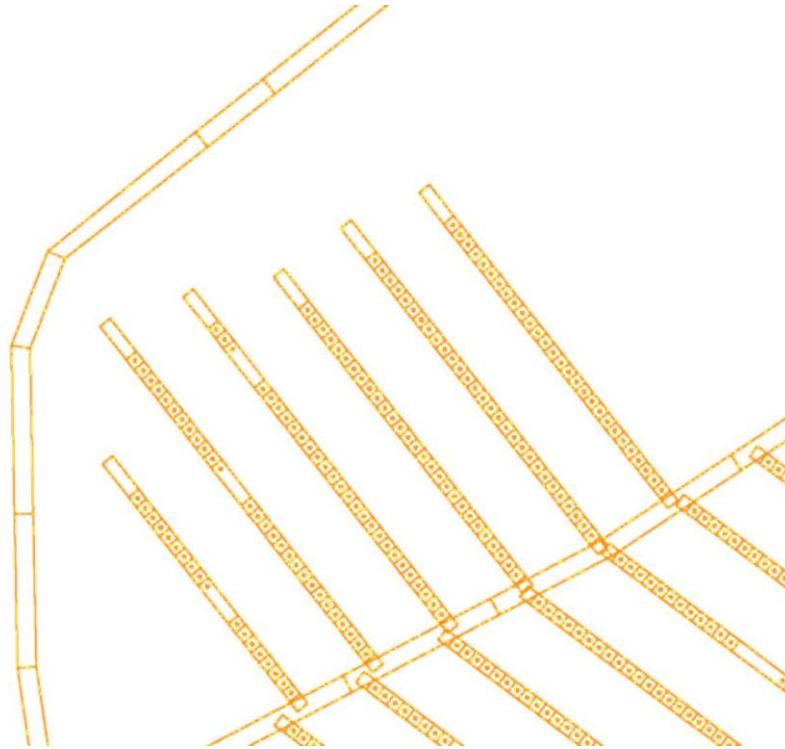
Figure 8.12 Detail view of western corner of repository layout adapted to a realization of the base-case DFN. Segments with dots indicate deposition tunnel segments with canister Note that the three tunnels farthest to the left have open segments without deposition holes, due to application of the FPC criterion for an intersecting feature.

Mesh assembly

Mesh generation followed essentially the same procedures as for previous versions of the DFM model for Forsmark. For each realization and geometric variant, panel files representing deterministic and stochastic features, along with repository components, were assembled and then discretized into a finite-element mesh such as shown in plan view in Figure 8.13.

The hydraulic properties of regional and local deformation zones were assigned stochastically to each triangular element belonging to a given deformation-zone feature, based on the correlation model described previously. This approach was chosen due to practical advantages of implementation, versus the alternative of assigning these properties prior to discretization. However, a consequence is that the deformation-zone hydraulic properties for a given realization are not independent of the realization of the DFN component.
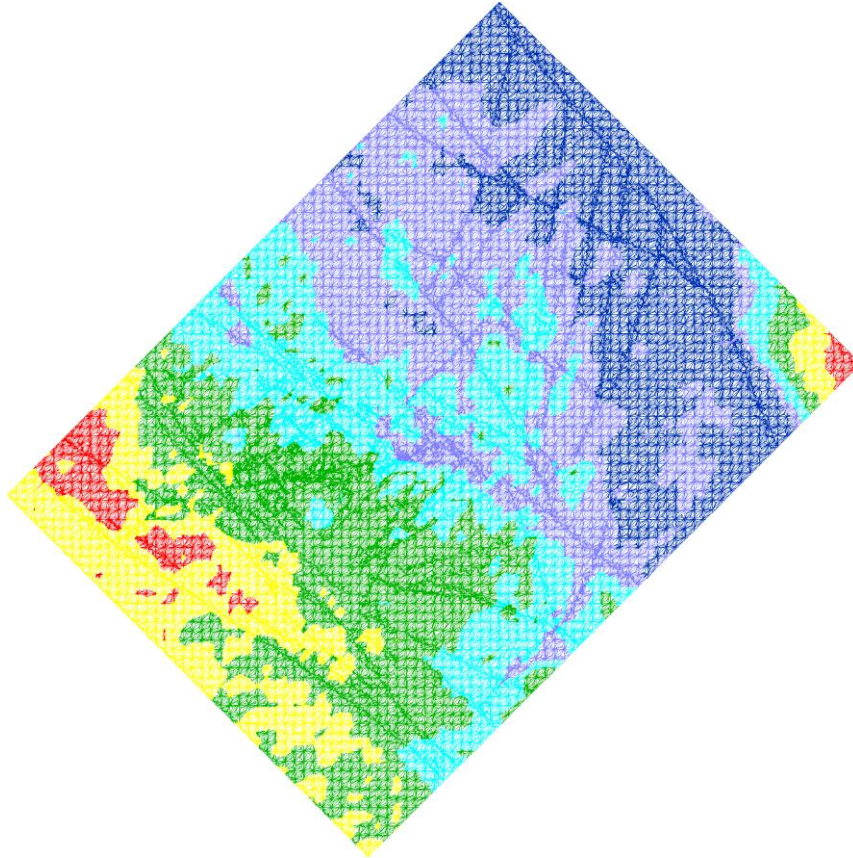
Figure 8.13 Plan view of surface feature for Forsmark in the final mesh, coloured to show topographic/bathymetric elevations. The colour scale represents elevation with respect to mean sea level as follows: dark blue, below -13.3 m; medium blue, -13.3 m to -6.7 m; pale blue, -6.7 m to 0 m; green, 0 m to +6.7 m; yellow, +6.7 m to +13.3 m; red, above +13.3 m. Intersections with regional and local deformation zones are visible as lines cutting across the otherwise regular triangular grid.

Boundary conditions for flow simulations

Base-case boundary conditions (Table 8.5) were chosen to approximate a situation similar to the present day at Forsmark.

For portions of the topographic upper surface that are at or above sea level, the head is set equal to equal to the elevation *Z*.

For portions of the topographic surface that are below sea level, a fixed head is assigned equal to zero (the present-day mean sea level, used as a datum). Note that this approach will somewhat exaggerate the pressure gradients (modelled as equivalent freshwater head gradients) through the model, since in reality the groundwater pressures at the seabed will be higher due to the salinity of the water column. The resulting head values at boundary nodes are plotted in Figure 8.14.

67

Linearly varying heads to approximate the topographic gradient are applied along each of the lateral boundaries (based on a linear fit to the topography along that edge of the model), with a restriction that the head must be at least equal to sea level.

A no-flow condition is implicitly specified at the base. This is consistent with a hypothesis that the bedrock becomes extremely low in permeability at depth.

A variation of these boundary conditions using the preliminary version of the structural model replaced the boundary conditions along the southeast and northwest sides with a no-flow ($q = 0$) condition.

Table 8.5 Summary of boundary conditions for flow model.

| Boundary	Boundary Condition Type	Value
Seafloor	Specified head	$h = 0$
Land surface	Specified head	$h = \max(0, Z)$
Bottom	Specified flux	$q = 0$
Southwest side	Specified head	$h = \max(0, -0.000505\,X + 0.000505\,Y - 2549.53\text{ m})$
Southeast side	Specified head	$h = \max(0,\ 0.000806\,X + 0.000806\,Y - 6713.51\text{ m})$
Northeast side	Specified head	$h = \max(0,\ 0.000041\,X - 0.000041\,Y + 217.95\text{ m})$
Northwest side	Specified head	$h = \max(0, -0.000445\,X - 0.000445\,Y + 3716.48\text{ m})$
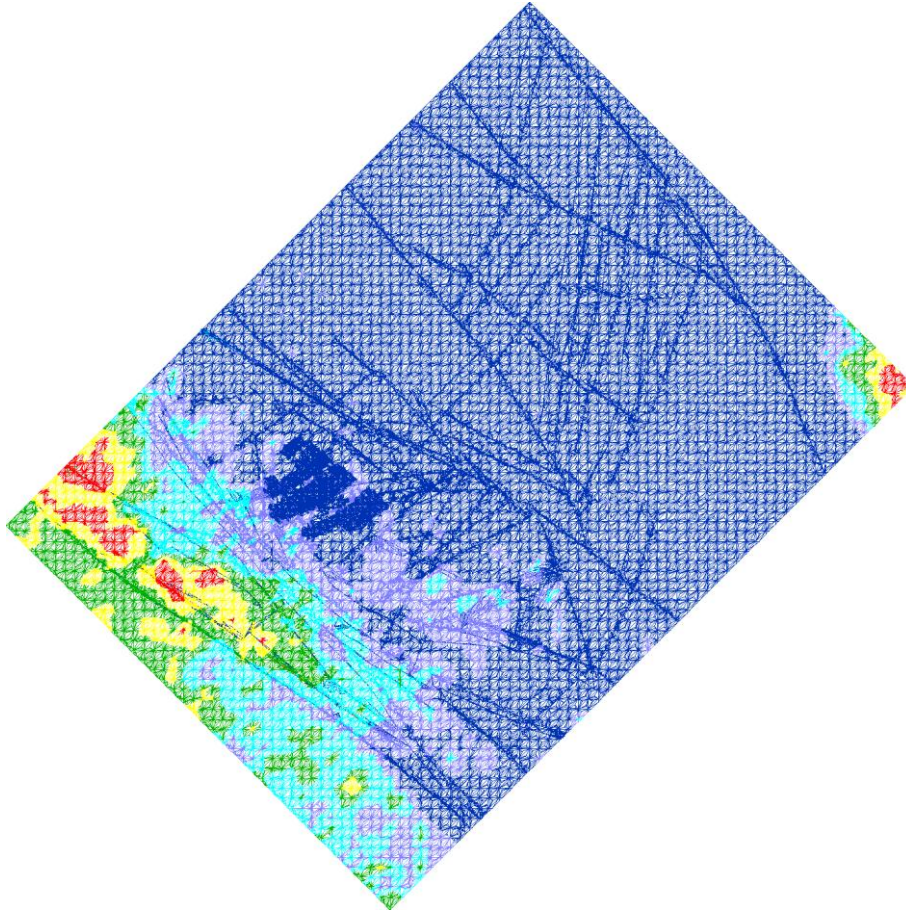
Figure 8.14 Boundary nodes in the base-case model (view from above), coloured to show head values. The colour scale represents heads with respect to mean sea level as follows: dark blue, 0 m mean sea level; medium blue, 0 m to 5 m above mean sea level; pale blue, 5 m to 10 m; green, 10 m to 15 m; yellow, 15 m to 20 m; red, above 20 m. The repository deposition holes (treated as internal, zero-net-flux boundaries) are visible as an aggregation of dark-blue points just left of the centre of the plot.

Summary of model variants

Results were obtained for the following model variants with respect to the DFN component:

- Base case: Poisson model with denser DFN (two realizations),
- Sparse variant: Poisson model based on same DFN statistical model as base case, but excluding the smaller and less transmissive fractures as a function of distance from the repository (one realization)
- Exponential halo model (two realizations).

One variation in boundary conditions was also tested:

- Regional flow/decreased topographic influence variant: Head increases toward base of model on SW boundary (to represent hypothetical effects of

regional flow), while influence of local topography is reduced by reducing the head values specified on the land surface to just 80% of the topographic elevation (to represent a hypothetically reduced water table under hills).

Additional variations in boundary conditions were explored in an earlier stage of this work (Geier, 2010g) using a preliminary model that used a different representation of the deformation zones and did not include the regional conductivity grid. Although these variants have not been updated with regard to other aspects of the model, they help to inform the discussion regarding the relative significance of uncertainty in boundary condition vs. uncertainty in other aspects of the model.

The suite of variants considered is summarized in Table 8.5.

Table 8.5 Summary of evaluated DFM model variants (* = same as base case).

Name	Deterministic sub-model	Stochastic DFN sub-model	Shell options	Boundary conditions
Base case	Single-surface deformation zones + regional conductivity grid	Poisson model (SDM-Site r_0-fixed variant)	Higher density	Specified-head on all lateral boundaries, no-flow at base of model, head equal to topographic elevation on land surface, head equal to sea level on sea-floor.
Sparse variant	*	*	Lower density	*
Halo model	*	Exponential halo model	*	*
Regional flow	*	*	*	Increasing head at depth on SW boundary, reduced influence of topography on land, otherwise same as base case.
Preliminary fixed-head	Double-surface deformation zones, no regional conductivity grid	*	*	*
Preliminary no-flow	Double-surface deformation zones, no regional conductivity grid	*	*	No-flow on SE and NW boundaries, otherwise same as base case.

Flow simulations

Groundwater flow equations

Within each planar segment of a feature, groundwater flow is governed by the 2-D transient flow equation:

$$S \frac{\partial h}{\partial t} - \nabla \cdot (T \nabla h) = q(\xi)$$

where S and T are respectively the local storativity and transmissivity, h is hydraulic head, t is time, and q is a source/sink term which is zero everywhere except at the specified boundaries. In the present work, S and T are assumed to be homogeneous within a given triangular segment. Conservation of mass and continuity of hydraulic head are required between segments, and at intersections between features.

All cases modelled in this study are for steady-state flow, in which case the time derivative is zero and the local flow equation simplifies to:

$$\nabla \cdot (T \nabla h) = -q(\xi)$$

Finite-element approximation

The steady-state groundwater flow equation is applied to the discrete geometry represented by the computational mesh, by use of the Galerkin finite-element method. This leads to a system of linear algebraic equations of the form:

$$Ah = q$$

where **A** is a sparse, diagonally dominant, banded matrix with coefficients depending only upon the transmissivity and geometry of each triangular element, *h* is a column vector of steady-state head values at the element vertices, and *q* is a column vector of unbalanced flux values at the vertices, equal to zero except at physical boundaries where inflow or outflow occurs. Mathematical details are given by Geier (2005).

Features that are not connected to a specified-head boundary (either directly or indirectly via connections with other features and/or net-specified-flux boundaries) are indeterminate and are not represented in the matrix equations. These features constitute hydraulically isolated networks.

Solution of flow equations

Solutions to the systems of linear algebraic equations for the steady-state case are obtained using a standard sparse-matrix method, conjugate-gradient method preconditioned by simple diagonal scaling, to minimize a global error measure.

Experience with solving flow equations on discrete-feature networks has shown that iterative solvers can give locally poor results for branches of a network that are isolated from the main flowing branches by tight (low-

transmissivity) sections that function as "bottlenecks." A multi-step solution approach was therefore used, in which each step consisted of the following two substeps:

- Conjugate-gradient minimization of global error measure.
- Local smoothing by iteratively boosting heads of internal nodes that are surrounded by nodes with higher heads.

The local-smoothing method is implemented in the *dfm* module of the *DFM* toolkit, Version 2.3.2 and subsequent versions (Geier, 2010h).

Calculation of flows and velocities to canister positions

Flows to canister positions are calculated as the sum of all positive flows into the deposition hole (generally balanced by outflows).

The water velocity in the fractures intersecting the deposition holes is of interest for bentonite erosion modeling as well as for radionuclide transport. The mean velocity at the *i*th deposition hole was calculated as:

$$\bar{v}_i = \frac{\sum\limits_{j \in i} Q_j}{\sum\limits_{j \in i} L_j b_{Tj}}$$

where:

Q_j = flowrate across the *j*th element edge [L^3/T],

L_j = length of *j*th edge, and

b_{Tj} = transport aperture at *j*th edge.

and where the sums are taken over all element edges *j* that intersect the *i*th deposition hole.

Transport simulation

Advective-dispersive transport of non-sorbing solute through the 3-D network (neglecting matrix diffusion) is modelled by the discrete-parcel random walk method (Ahlstrom et al., 1977). This approach represents local, 2-D advective-dispersive transport within each fracture plane. 3-D network dispersion, due to the interconnectivity among discrete features, arises as the result of local dispersion in combination with mixing across fracture intersections.

For mathematical details and definition of parameters see Geier (2005; 2008b). The algorithm assumes complete mixing at fracture intersections; this is a reasonable approximation for the low advective flow velocities expected in a post-closure repository, as discussed by Geier (2008a).

Particles are initiated from source locations, which in the present study comprise the intersections of transmissive features with the perimeters of the deposition holes. For each canister position that is intersected by a transmissive feature, 100 particles are released. Transport parameters used in this step are summarized in Table 8.6.

Table 8.6 Parameters for advective-dispersive particle tracking.

Parameter	Feature Category	Feature Set(s)	Value
Molecular diffusion coefficient	All	1 to 68	2.0×10^{-9} m^2/s
Ratio of transverse dispersivity to longitudinal dispersivity	All	1 to 68	0.1
Longitudinal dispersivity	Major deformation zones	1	10 m
	Shallow bedrock aquifer	2	10 m
	Quaternary deposits	3	5 m
	Repository tunnels	4	1 m
	Single fractures	5 to 68	1 m

Results

The principal results are obtained in the form of calculated head distributions at repository depth, flow rates to deposition holes, and transport paths as represented by advective-dispersive particle trajectories.

Hydraulic head distribution at repository depth

The resulting head field in the plane of the repository for the base case and main variants is shown in Figures 8.15 through 8.18.

All cases show a broadly similar pattern of heads variation at this depth, with a NW-SE trending "ridge" of relatively high heads along the deformation zones that border the "shear lens" just to the SW of the repository, with head decreasing both immediately to the SE (where another deformation zone connects to topographic lows at the SE edge of the model) and NW toward the sea.

The two different realizations of the base-case model (Figure 8.15) show differences in hydraulic head of up to 0.5 m for a given point in the repository. However, the difference in head from SW to NE across the area occupied

by the deposition tunnels is similar, from about 1 m to 1.2 m. Thus the average horizontal head gradient through the deposition area is of similar magnitude for both realizations. The differences between realizations may be due to stochastic variation of hydraulic properties in the deformation zones, as well as difference between realizations of the DFN component.

The sparse-DFN variant is compared with one realization of the base case in Figure 8.16. The differences in hydraulic head at a given point in the repository are again typically less than 0.5. The head difference across the repository is slightly higher for the sparse variant (about 1.3 m) than for the base case. Again, the differences between these cases may be due to stochastic variation of properties in the deformation zones, as well as difference between realizations of the DFN component.

The two realizations of the exponential-halo variant (Figure 8.17) show a stronger difference in gradient across the repository, from 0.8 m to 1.3 m. As for the base-case, the difference between realizations can include effects of stochastic variation in deformation zone properties, as well as in the DFN.

The regional-flow/reduced topographic heads variant, which uses exactly the same mesh as base case realization 01 (Figure 8.18) shows a nearly uniform reduction in head within the repository, by about 0.3 m, with a very slight decrease in gradients. The decreased heads indicate that the reduction in topographic heads has a greater influence than the increased head at the base of the inland (SW) boundary, in this variant.
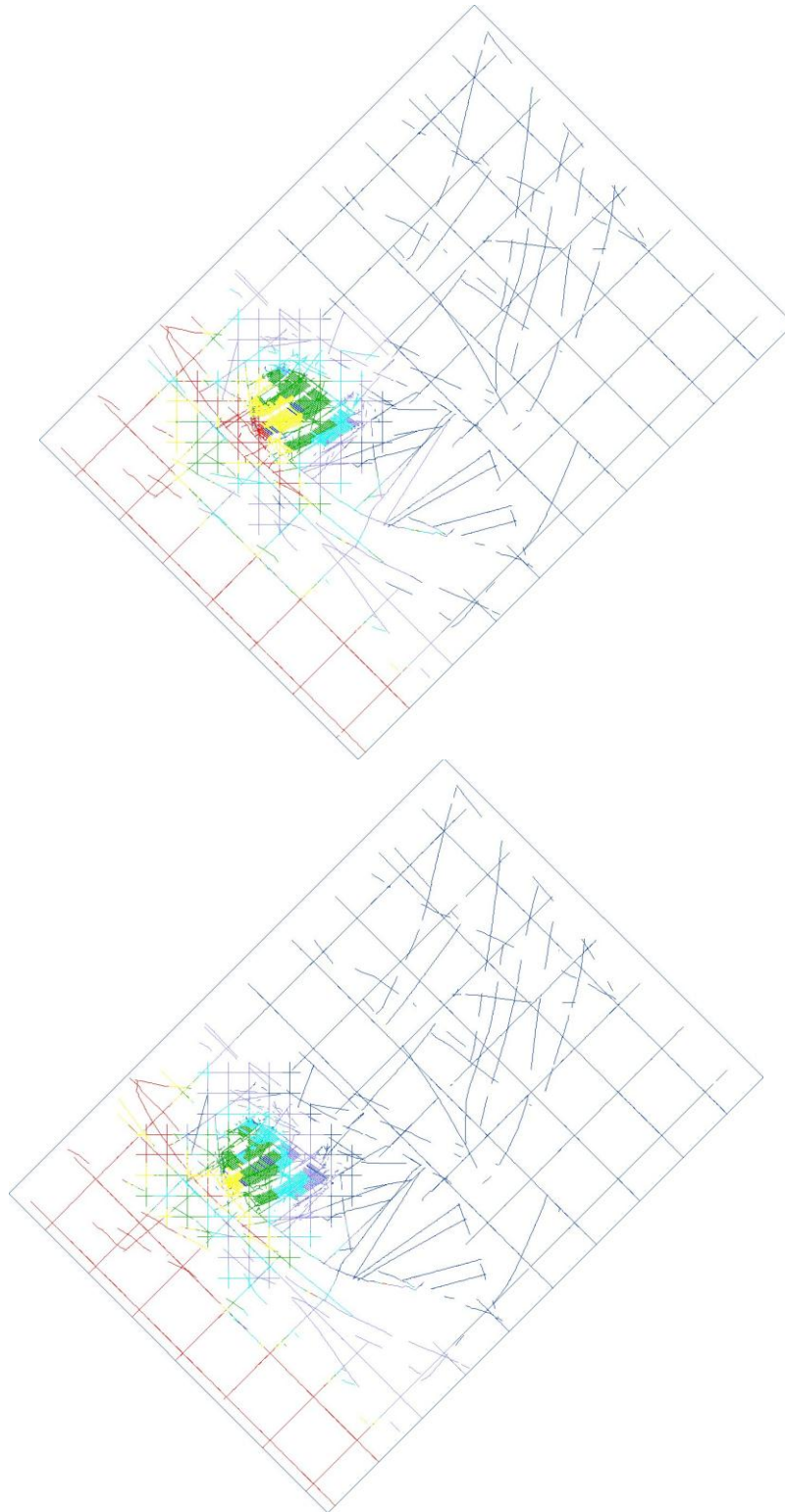
Figure 8.15 Horizontal section through repository area of mesh at Z = -460 m, base case, realizations 01 (top) and 02 (bottom). The colour scale indicates the calculated heads along the discrete features that intersect the plane of the section; dark blue indicates h < 0.33 m; medium blue, 0.33 m to 0.67 m; pale blue, 0.67 m to 1.0 m; green, 1.0 m to 1.33 m; yellow, 1.33 m to 1.67 m; red, h > 1.67 m.
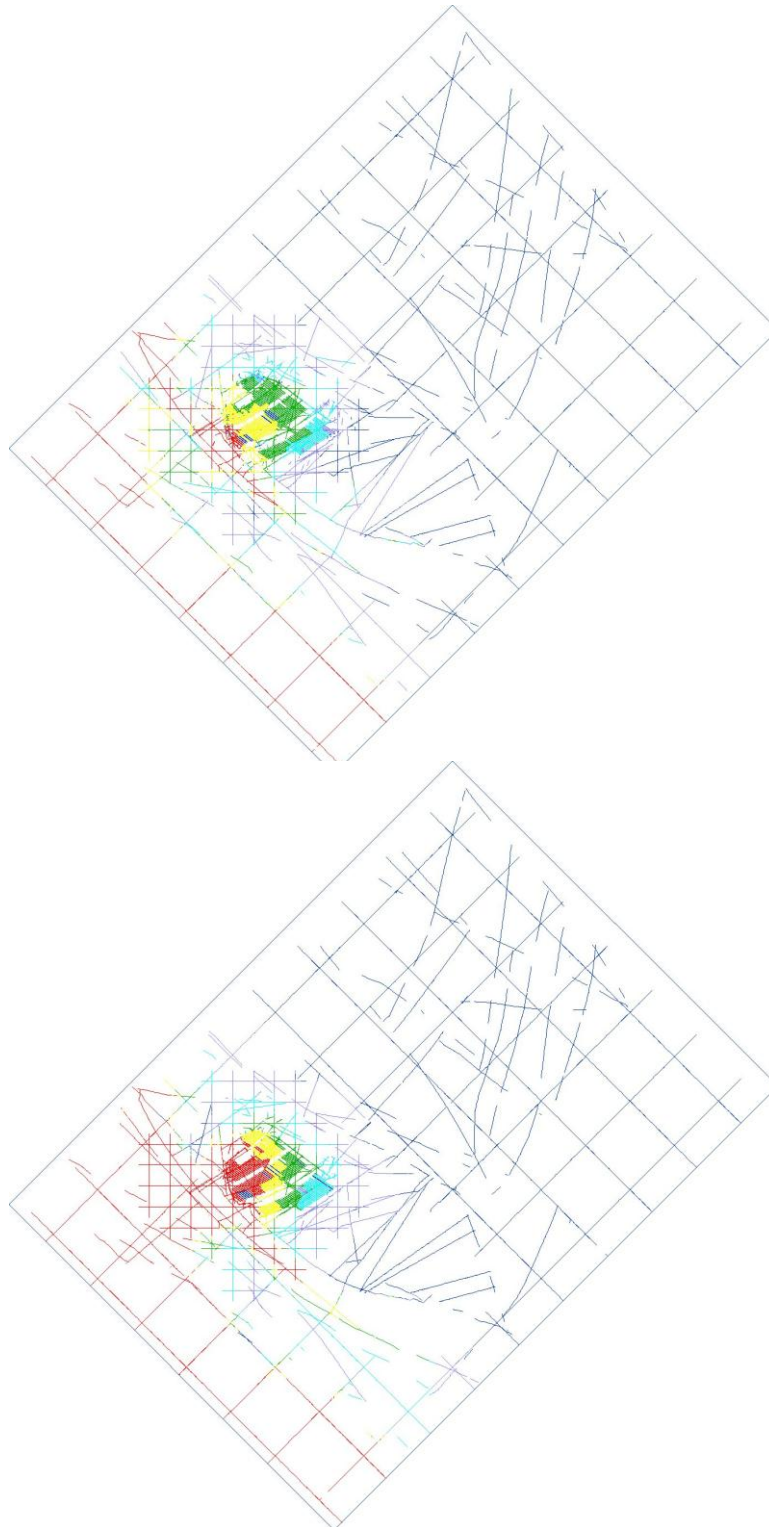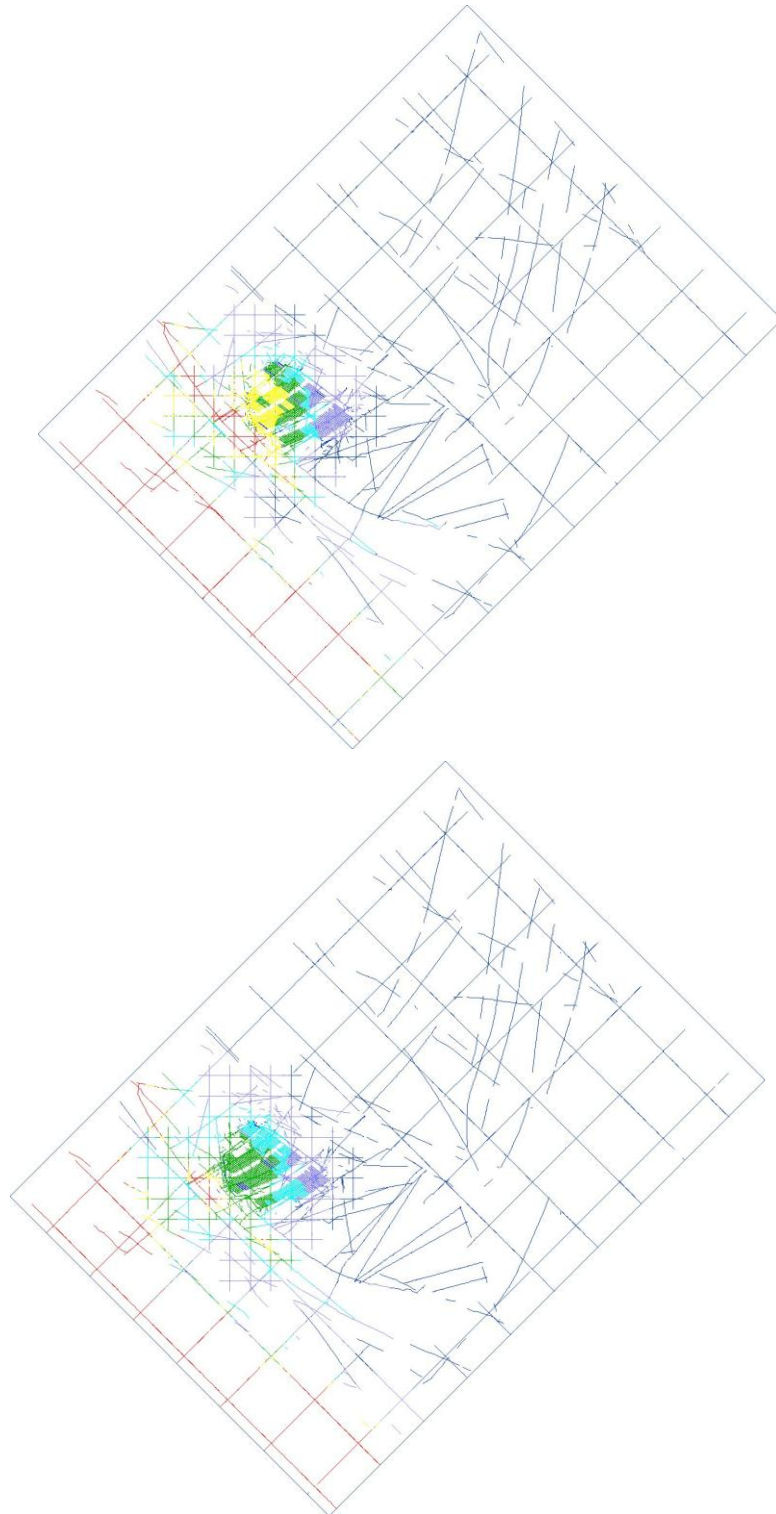
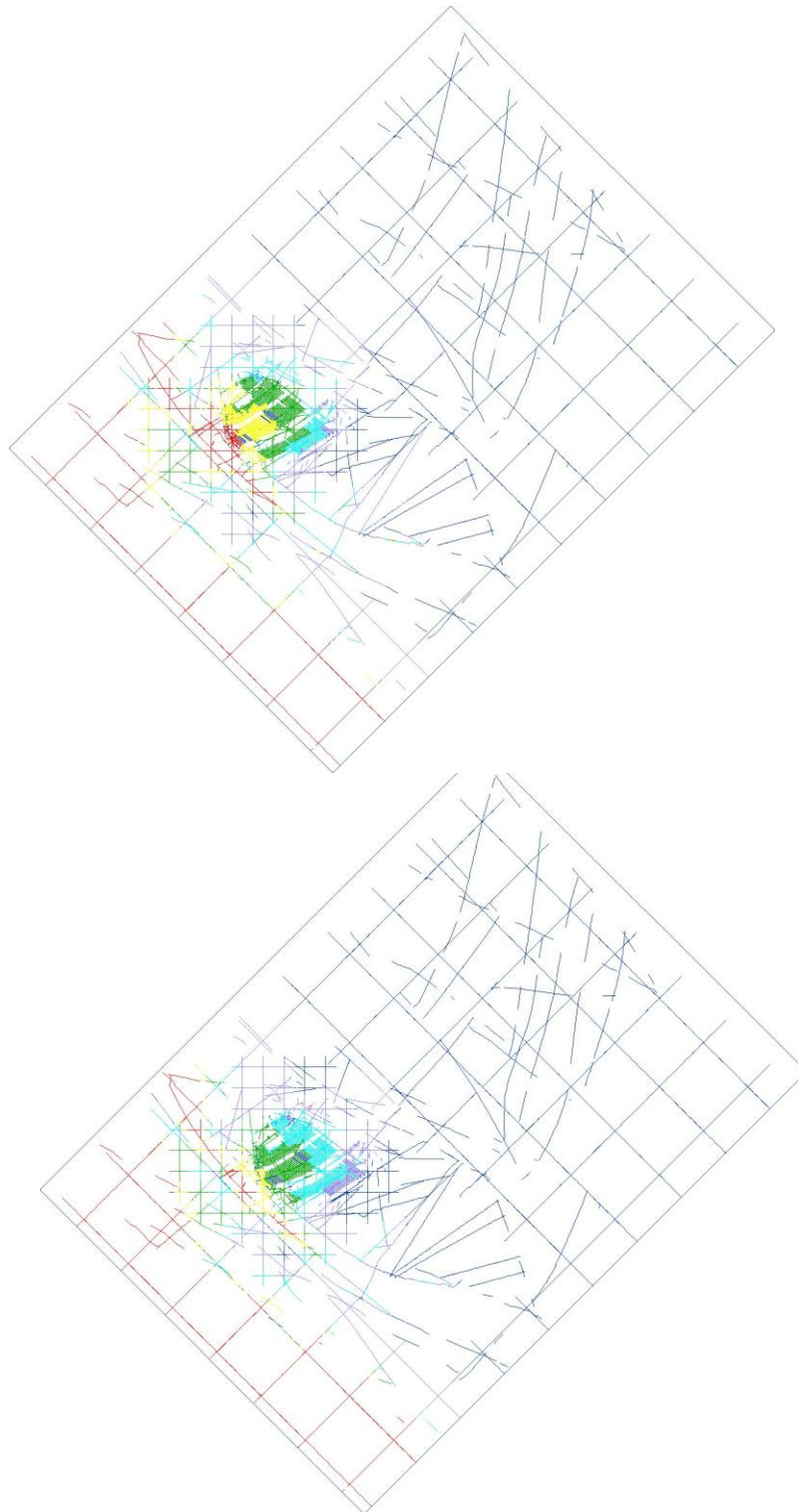**Figure 8.16** Horizontal sections through repository area of mesh at Z = -460 m, comparing base case, realization 01 (top) with sparse variant, realization 01 (bottom). The colour scale indicates the calculated heads along the discrete features that intersect the plane of the section; dark blue indicates h < 0.33 m; medium blue, 0.33 m to 0.67 m; pale blue, 0.67 m to 1.0 m; green, 1.0 m to 1.33 m; yellow, 1.33 m to 1.67 m; red, h > 1.67 m.

Figure 8.17 Horizontal section through repository area of mesh at Z = -468 m, exponential halo variant, realizations 01 (top) and 02 (bottom). The colour scale indicates the calculated heads along the discrete features that intersect the plane of the section; dark blue indicates h < 0.33 m; medium blue, 0.33 m to 0.67 m; pale blue, 0.67 m to 1.0 m; green, 1.0 m to 1.33 m; yellow, 1.33 m to 1.67 m; red, h > 1.67 m.

Figure 8.18 Horizontal section through repository area of mesh at Z = -468 m,comparing base case, realizations 01 (top) with the same realization of the regional-flow/reduced topographic influence variant (bottom). The colour scale indicates the calculated heads along the discrete features that intersect the plane of the section; dark blue indicates h < 0.33 m; medium blue, 0.33 m to 0.67 m; pale blue, 0.67 m to 1.0 m; green, 1.0 m to 1.33 m; yellow, 1.33 m to 1.67 m; red, h > 1.67 m.

Flow to deposition holes

Flow rates to deposition holes are shown in Figure 8.19 for the main variants including:
- Two realizations of the Poisson model (base case),
- One realization of the sparse variant, and
- Two realizations of the exponential halo model.
- One realization of the regional flow/reduced topographic effect variant.

All variants and realizations yielded similar numbers of acceptable canister deposition sites based on FPC criterion, ranging from 8196 to 8300 (about a 1% range).

Differences between realizations of the base case are statistically significant with a Kolmogorov-Smirnov statistic (as a test of the null hypothesis that the flow rates for the two realizations are drawn from the same distribution) as high as 0.08. However the maximum difference in the cumulative distribution of flow rates between the two realizations, for any given percentile above the median, is less than a factor of 2. Thus the difference between realizations appears to be of minor practical importance, even if statistically significant.

The sparse DFN variant (labeled as "higher r_{min}" in the figure) yielded the highest percentage of deposition holes for which flow rates were 0.01 liters/year or less (8% vs. a mean of 4% for the two base-case variants). Thus excluding these smaller and lower-transmissivity fractures has an impact on the estimated number of deposition holes with very low flow rates. However, the effects of excluding these fractures are practically indistinguishable from the base case, for deposition holes with flows greater than 10 liters/year.

Both realizations of the exponential-halo model show an increase in the proportion of deposition holes that carry flows higher than 100 liters/year, relative to the base case. In terms of these higher-flow holes, there is also high variability between realizations of the exponential-halo model. At the low end of the flow range, the differences with the base case are minor relative to the differences between realizations.

The regional-flow/reduced-topographic-heads variant produces only minor differences with the equivalent realization of the base case, with a very slight reduction in the proportion of holes with higher flow rates.

An additional evaluation of boundary-condition effects was carried out using the preliminary version of the structural model, which did not include a regional conductivity grid. The use of no-flow rather than fixed-head conditions along the NW and SE sides of the model produced a reduction of about half an order of magnitude in the median flow rates, but with similar variability of flow rates (as measured by the span between the 10th and 90th percentiles, on a log scale). Both of these preliminary calculation cases yielded lower flows than the base case, presumably due to reduced connectivity on the regional scale.
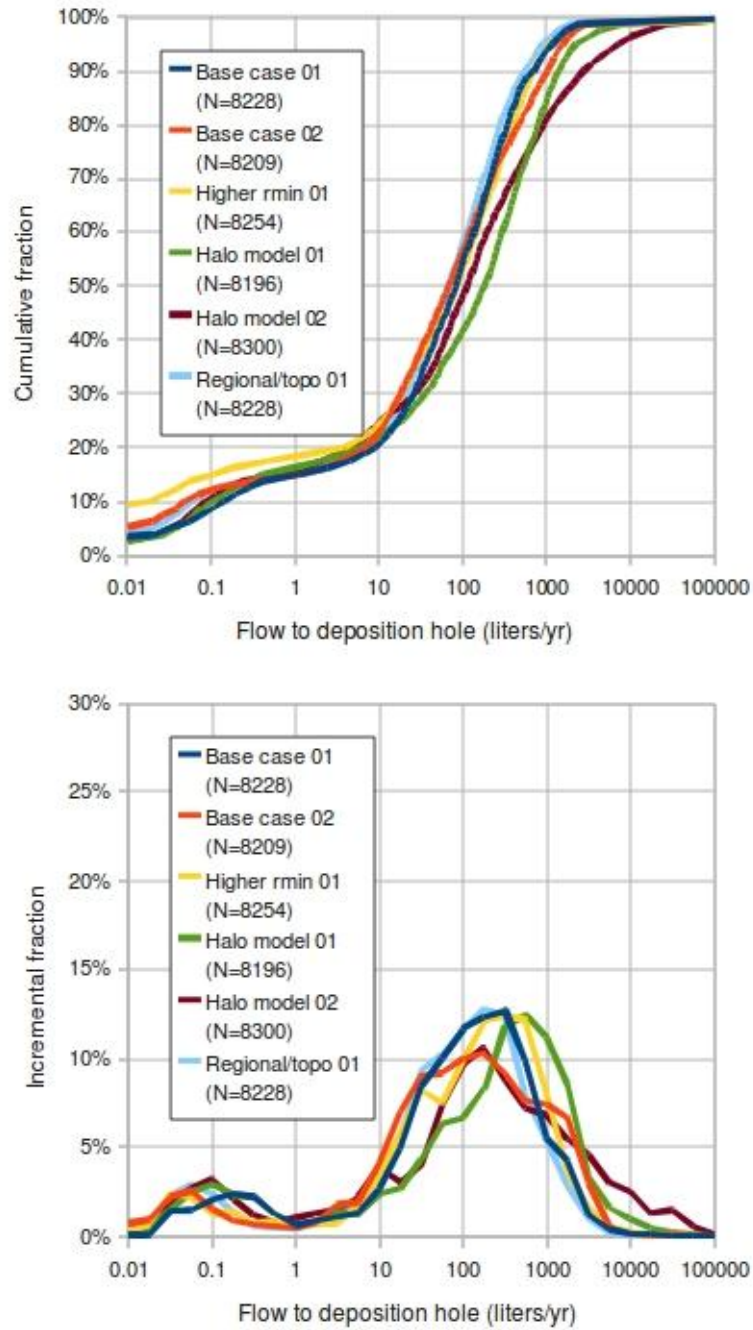
Figure 8.19 Cumulative and incremental distributions of flow rates through deposition holes in litres per year, for the main model variants considered in this project. Each data point on the incremental density plot represents the fraction of the points that are within a bin covering 1/4 order of magnitude on the logarithmic scale.
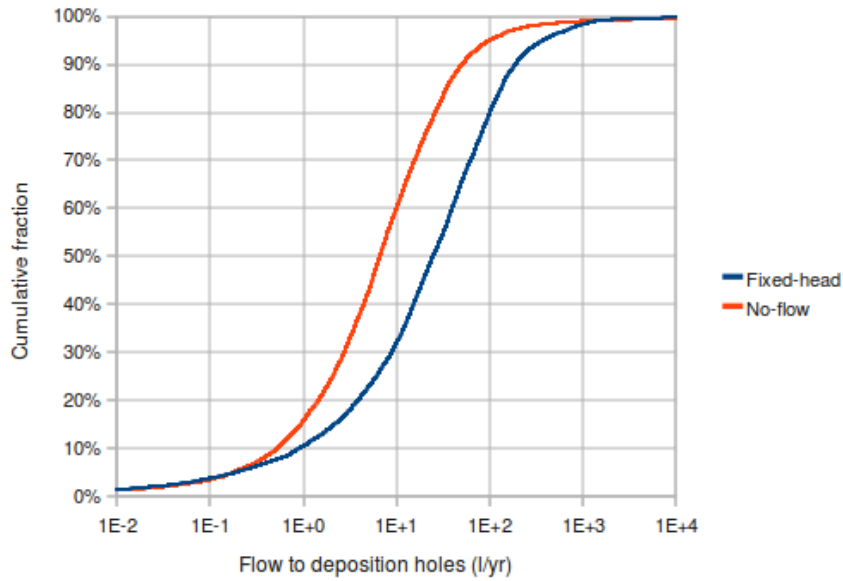
Figure 8.20 Cumulative distributions of flow rates through deposition holes in litres per year, for the two pre-liminary variants to test the effects of boundary conditions (fixed-head along NW and SE boundaries, vs. no-flow along these boundaries). These results are based on a discrete-feature model that used the "double-sided" deformation zones and did not include the regional conductivity grid.

Velocities in fractures at deposition holes

Water velocities to the deposition holes for the base case and exponential-halo model are summarized in Table 8.7, and shown in Figure 8.21. Consistent with the higher flow rates in the exponential halo variant, this variant also produces higher velocities to deposition holes. The highest velocities presumably represent flow bottlenecks in the near field that do not persist over long distances.

Table 8.7 Water velocities to deposition holes.

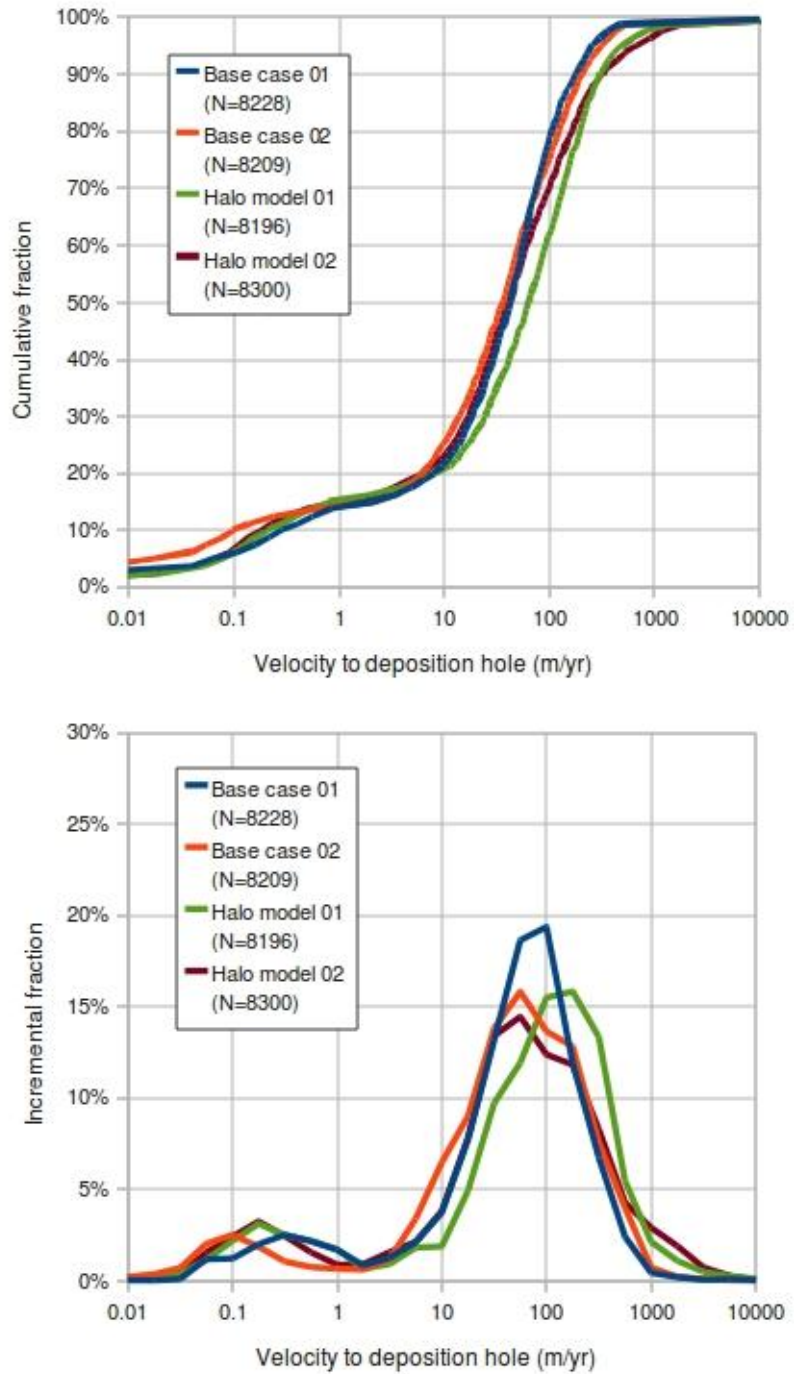| Model variant	Realiza-tion	10th Percentile	Median	90th Percentile	99th Percentile
Base case	1	0.29 m/yr	43 m/yr	180 m/yr	480 m/yr
	2	0.10 m/yr	36 m/yr	200 m/yr	550 m/yr
Exponential halo	1	0.21 m/yr	64 m/yr	300 m/yr	1350 m/yr
	2	0.18 m/yr	41 m/yr	320 m/yr	1700 m/yr

81

Figure 8.21 Cumulative and incremental distributions of water velocities to deposition holes in litres per year, for two realizations each of the base case and exponential-halo model variant. Each data point on the incremental density plot represents the fraction of the points that are within a bin covering 1/4 order of magnitude on the logarithmic scale.

Transport results

Particle trajectories for the base case, exponential-halo variant, and the regional-flow/reduced-topographic-heads variant are illustrated in Figures 8.22 through 8.25.

Most of the particles released from deposition holes ended up either at other deposition hole positions (which is expected in many cases, due to the fact that tunnel features are a primary transport path), or else became stuck in far-field features. The latter results (stuck particles in apparently stagnant elements) are interpreted as an artefact of locally poor mesh geometries and poor connectivity in the deformation zones and fractures. This limits the quantitative usefulness of the results, but some qualitative observations can be made.

The direction of particle movement from the repository is in most cases initially downward, and northward before turning upward along one of the deformation zones that connect to low head areas at the surface. However the initial direction of movement varies depending on the initial position within the repository and the local fracture geometry, which in turn depends on the realization.

As seen from Figure 8.22 and 8.23, different realizations can yield very different patterns for the base case model. In realization 01, nearly all particles released from the NW section of the repository move northward in a broad plume. In realization 02, particles segregate into two distinct plumes, one of which heads west while the other goes north before reaching the series of NW-SE trending deformation zones along the NE side of the shear lens (Singö Zone and related deformation zones). The influence of the local conductivity grid is apparent in Figure 8.23.

Similarly strong differences in the release pattern are seen between realizations of the exponential halo variant (Figures 8.24 and 8.25). In contrast, the release pattern for the regional-flow/reduced-topographic-heads variant is practically identical to that for the same realization of the base case (Figure 8.26). This suggests that the details of the DFN component around the repository, possibly together with stochastic variability of hydraulic properties in the deterministic deformation zones, is the main determining factor for release pattern, rather than boundary conditions.
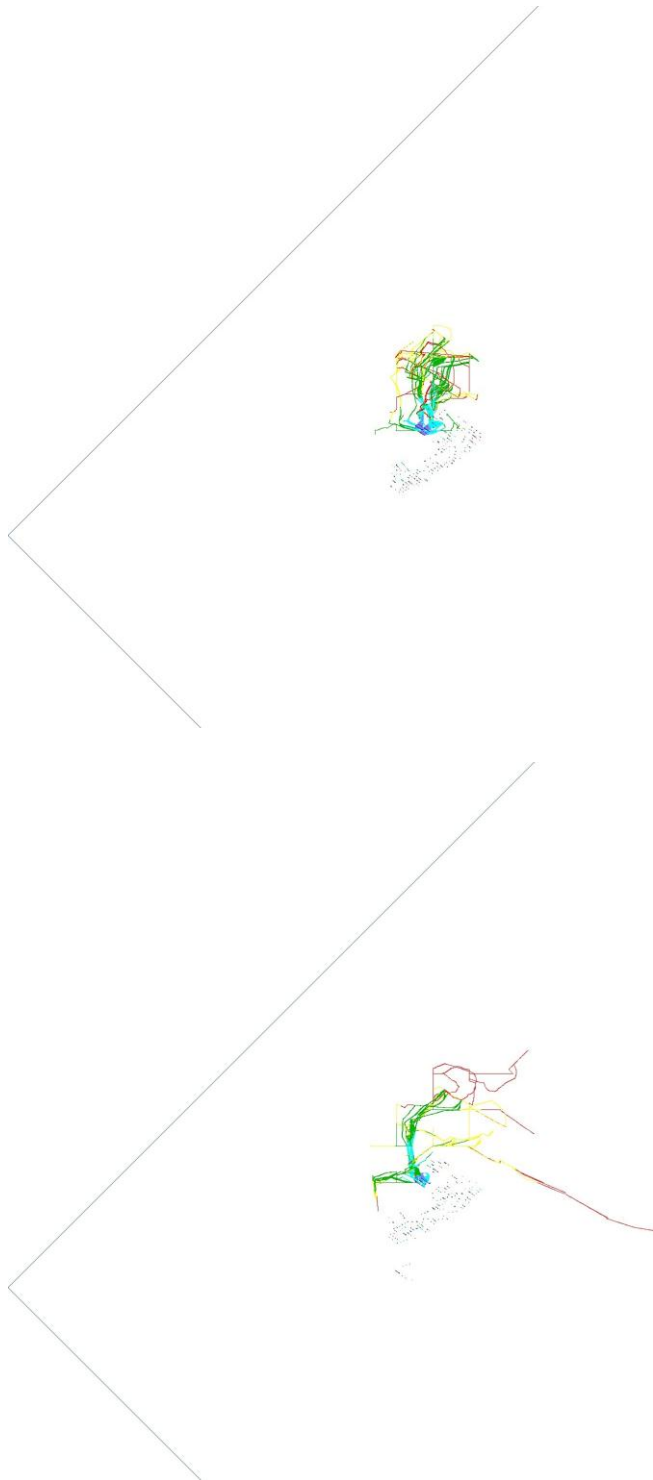
Figure 8.22 Advective-dispersive particle trajectories for a portion of the repository, base case, realization 01 (top) and realization 02 (bottom). The colour scale indicates the age of the particle as it travels along the trajectory; dark blue indicates t < 0.5 day; medium blue, 0.5 to 2.5 days; pale blue, 2.5 to 11 days; green, 11 to 53 days; yellow, 53 to 250 days; red, >250 days (>0.68 years). Most particle trajectories terminated at depth so end points do not necessarily represent discharge points in the biosphere.
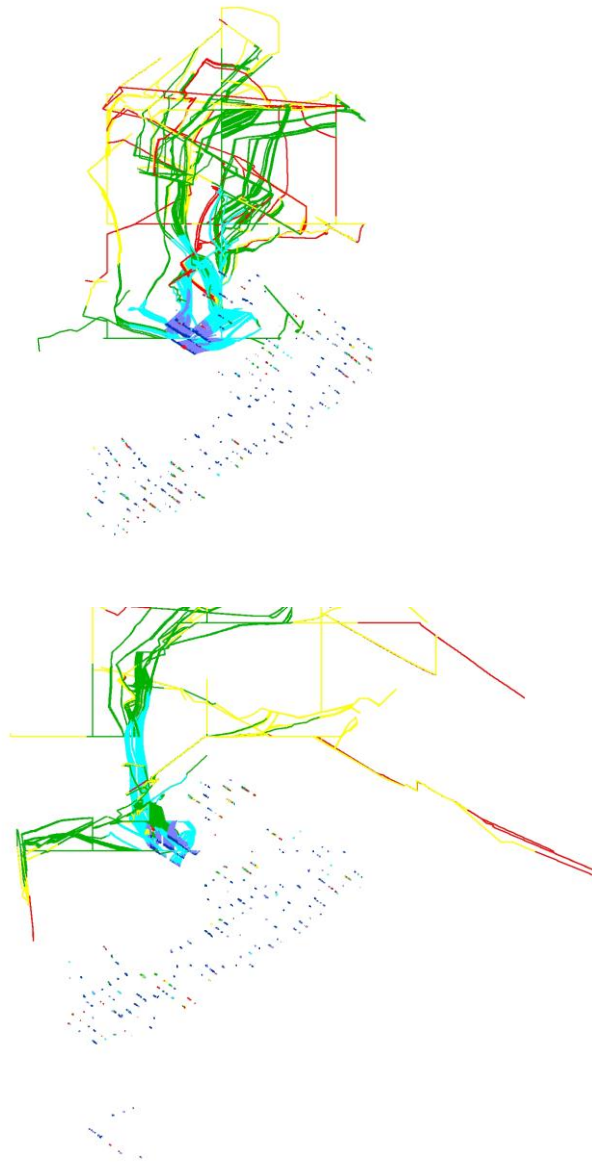
Figure 8.23 Expanded views of advective-dispersive particle trajectories for a portion of the repository, base case, realization 01 (top) and realization 02 (bottom), using the same colour scale as for the plots on the preceding page.
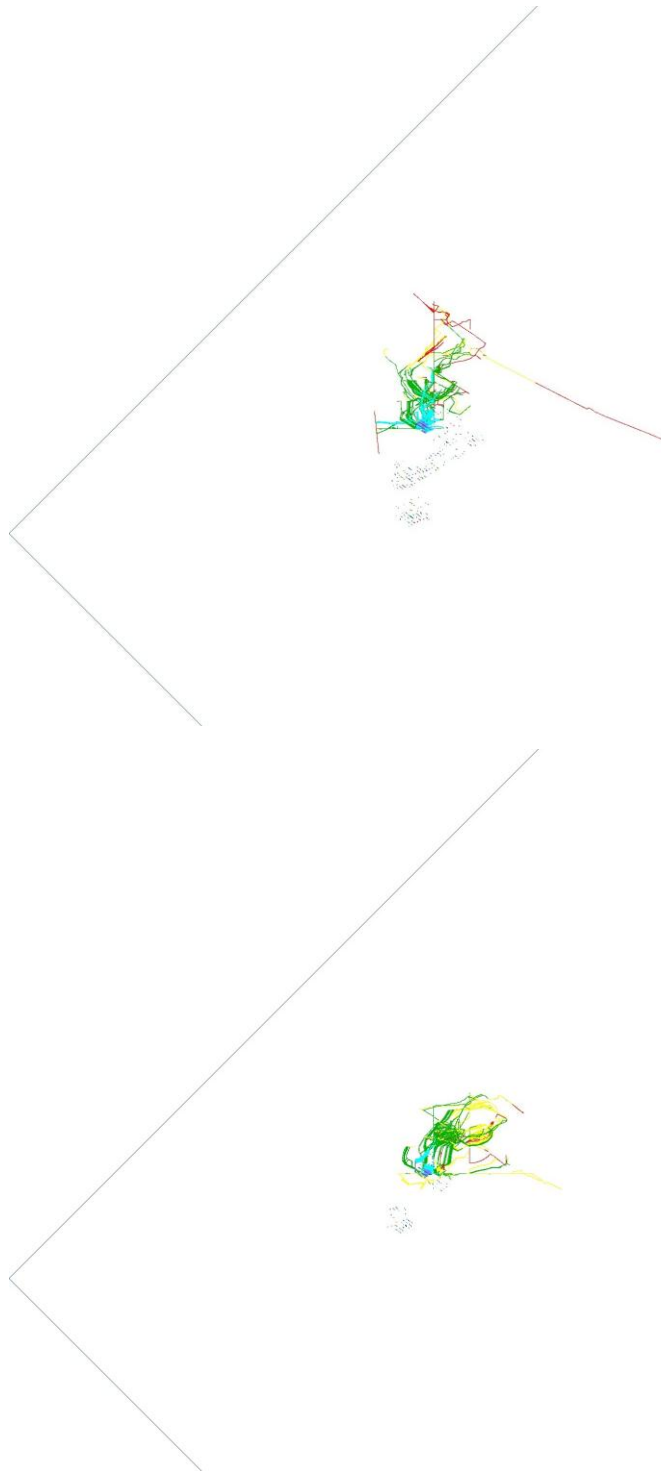
Figure 8.24 Advective-dispersive particle trajectories for a portion of the repository, exponential halo model, realization 01 (top) and realization 02 (bottom). The colour scale indicates the age of the particle as it travels along the trajectory; dark blue indicates $t < 0.5$ day; medium blue, 0.5 to 2.5 days; pale blue, 2.5 to 11 days; green, 11 to 53 days; yellow, 53 to 250 days; red, >250 days (>0.68 years). Most particle trajectories terminated at depth so end points do not necessarily represent discharge points in the biosphere.
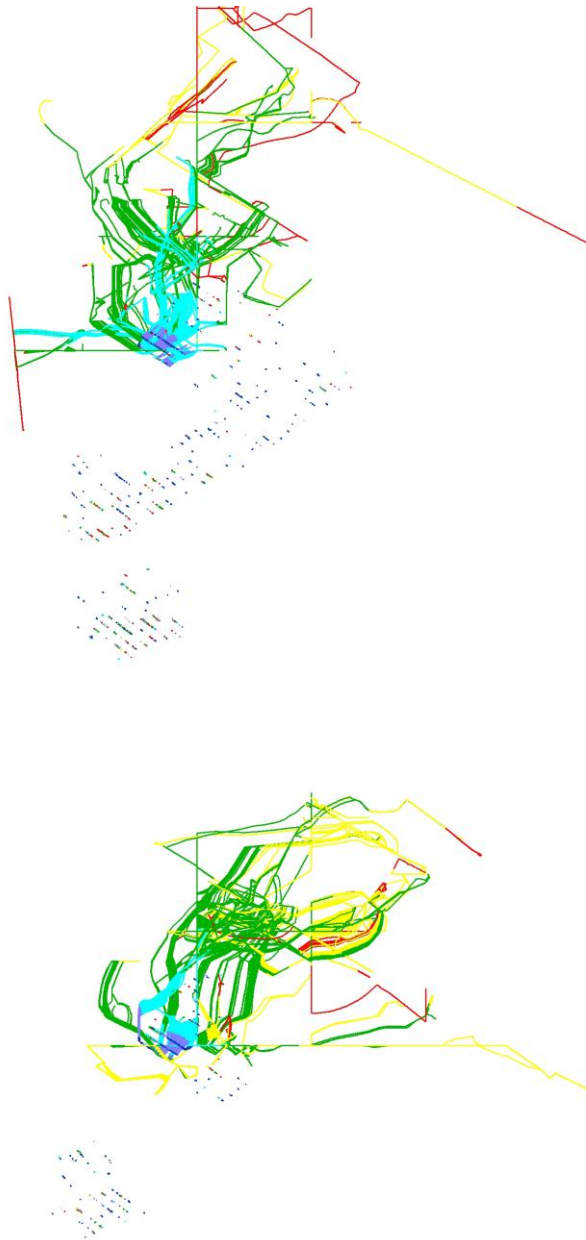
Figure 8.25 Expanded views of advective-dispersive particle trajectories for a portion of the repository, exponential-halo variant, realization 01 (top) and realization 02 (bottom), using the same colour scale as for the plots on the preceding page.
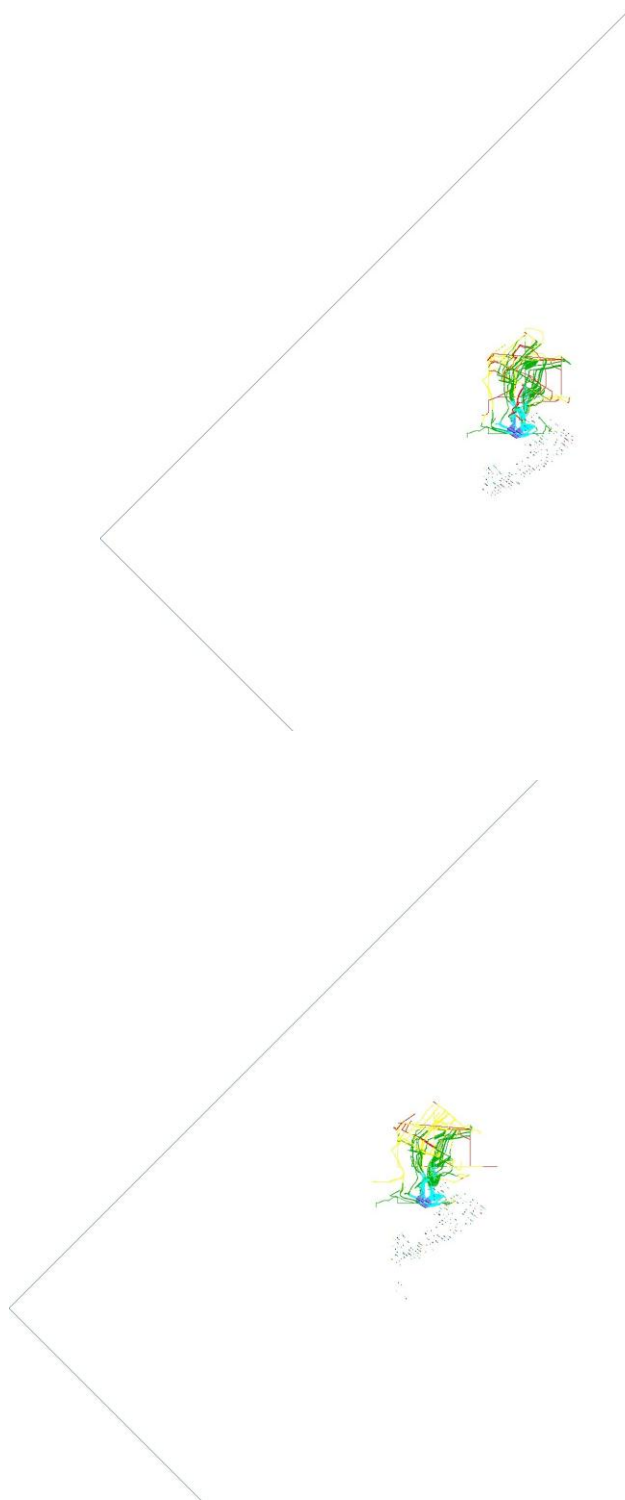
Figure 8.26 Advective-dispersive particle trajectories for a portion of the repository, comparing the base case, realization 01 (top) with the same realization of the regional-flow/reduced topographic influence variant (bottom). The colour scale indicates the age of the particle as it travels along the trajectory; dark blue indicates $t <$ 0.5 day; medium blue, 0.5 to 2.5 days; pale blue, 2.5 to 11 days; green, 11 to 53 days; yellow, 53 to 250 days; red, >250 days (>0.68 years). Most particle trajectories terminated at depth so end points do not necessarily represent discharge points in the biosphere.

Discussion

The predicted groundwater flow rates and velocities to deposition holes indicate that the DFN conceptual-model uncertainty, as represented by the exponential-halo model, is significant for repository safety.

The calculated groundwater velocities for the base case model are approximately the same as SKB has used for bentonite erosion modelling (SKB, 2008), but the exponential-halo model leads to predictions of substantially higher velocities for the most critical, higher-flow fraction of deposition holes. These higher velocities apparently result from improved connectivity of the DFN, which is expected from the spatial relationship of small fractures to larger fractures in the exponential-halo model.

Gradients through different parts of the repository, as evident in Figures 8.15 through 8.18, show some noticeable differences among different model variants and realizations. In realization 01 of the base case, relatively focused high gradients occur near the east side of the repository, with lower gradients elsewhere, while realization 02 has more uniform gradients throughout. Similarly, realization 01 of the sparse variant (Figure 8.16) shows high gradients in the middle section of the repository (from east to west), with lower gradients elsewhere. A similar pattern is shown by realization 01 of the halo model, although realization 02 of the same model shows more evenly distributed gradients.

These differences in gradient patterns do not translate obviously into flow results. Realization 02 of the base case has more high-flow canister positions, despite the apparently more uniform gradients through the repository. The same is true for realization 02 of the halo model. A possible explanation is that the highest-flow positions are controlled more by high-transmissivity fractures and connectivity leading to pathways with low net transmissivity, than by locally high-gradient situations. The single realization of the sparse variant is intermediate to the two realizations of the base case, in terms of flow results, so no clear conclusions can be drawn regarding the influence of a reduced resolution of the DFN.

Effects of stochastic variation in the different components of the DFM models are difficult to ascertain due to the simulation methodology. The stochastic component of hydraulic conductivity values was applied to deformation zone segments *after* discretization, so this cannot be entirely separated from the DFN component. However, an inference can be drawn assuming that the effects of stochastic hydraulic-property variability in the regional and local deformation zones should be similar for both DFN variants (base-case and exponential halo). The greater variability in head gradients with the exponential-halo model suggests that the influence of the DFN component is of comparable magnitude to the influence of DZ variation.

Particle tracking in the predicted flow fields was reasonably successful in the near-field portion of the model (close to deposition holes), but encountered

severe problems with stuck particles in the far field deformation zones. Further work is needed to improve the conditioning of the far-field finite-element mesh to reduce this problem. Alternatively, a pipe-flow concept being developed concurrently may provide a way of sidestepping this problem, while maintaining the concept of a discrete medium for groundwater flow and solute transport.

9. Conclusions

Based on an alternative evaluation of fracture data from core-drilled boreholes, an alternative model for the discrete-fracture network component of the Forsmark site models is proposed, with small fractures correlated in terms of location to larger fractures or deformation zones.

The alternative model, referred to herein as the "exponential halo" model, is likely just one of multiple alternatives that could be explored. It is derived primarily from surface-based data borehole data, so may need to be modified if and when additional data are available from underground. Based on simulated sampling in boreholes, there is no reason to exclude this model, and it may in fact be preferable to the uniform Poisson-process models considered heretofore by SKB (SKB, 2008).

Simulated sampling along tunnels in the proposed repository layout for the Forsmark site indicates that underground data should be sufficient to distinguish between the Poisson-process model and the exponential-halo model, likely at an early stage of the underground construction.

Simulations of trace lengths along tunnels also illustrate the profound effect of tunnel cross-section scale on these distributions. This may limit the potential to discriminate among alternative size distribution models based on underground data. Simulations indicate that statistically significant differences are expected, despite this profound effect, between the different size-distribution models that SKB has proposed. However, these differences are predicated upon idealized models and sampling circumstances that might not be realized underground, and rely upon small differences in the tails of the observed distributions. Whether or not these differences are robust with respect to non-ideal sampling situations is an open question.

The alternative exponential-halo model does not significantly affect repository utilization, based on the criteria that SKB has proposed for deposition-hole acceptance. However, flow simulations based on this model indicate a likelihood of elevated flow rates and groundwater velocities to deposition holes, relative to the Poisson-process model that SKB has considered.

The calculated flow rates and groundwater velocities for the base case model (corresponding to SKB's Poisson-process model) are approximately the same as SKB has obtained. The higher flow rates and velocities for the exponential-halo model apparently result from improved connectivity of the DFN, and illustrate the potential importance of alternative spatial models for fractures that have not been considered in SKB's analysis.

10.   References

Ahlstrom, S. W., Foote, H. P., Arnett, R. C., Cole, C. R., and Serne, R.J., 1977. Multicomponent mass transport model. Theory and numerical implementation (discrete parcel random walk version), Battelle report BNWL for ERDA, Columbus, Ohio.

Billaux, D., Chiles, J. P., Hestir, K., and Long, J. C. S., 1989. Three-dimensional statistical modeling of a fractured rock mass – an example from the Fanay-Augeres Mine. *International Journal of Rock Mechanics, Mining Science and Geomechanics Abstracts*, v. 26, p.281-299.

Brantberger, M., Zetterqvist, A., Anbjerg-Nielsen, Olsson, T., Outters, N., and Syrjänen, P., 2006. Final repository for spent nuclear fuel: Underground design Forsmark, Layout D1. SKB Report R-06-34, Swedish Nuclear Fuel and Waste Management Co., Stockholm.

Caine, J. S., 1999. The architecture and permeability structure of brittle fault zones. Ph.D. thesis, Department of Geology and Geophysics, University of Utah, 134 p.

Dershowitz W., Lee G., Geier J., Foxford T., La Pointe P., Thomas A., 1998. FRACMAN Interactive discrete feature data analysis, geometric modeling and exploration simulation. User documentation, version 2.6. Golder Associates, Inc., Redmond, Washington, USA.

Follin, S., Levén, S, Hartley, L., Jackson, P., Joyce, S., Roberts, D., and Swift, B., 2007. Hydrogeological characterisation and modelling
 of deformation zones and fracture domains, Forsmark modelling stage 2.2. SKB Report R-07-48, Swedish Nuclear Fuel and Waste Management Co., Stockholm.

Follin, S., Hartley, L., Marsic, N., 2008. Hydrogeological conceptual model development and numerical modelling using CONNECTFLOW, Forsmark modelling stage 2.3. SKB R-08-23, Swedish Nuclear Fuel and Waste Management Co., Stockholm.

Follin, S., 2008. Bedrock hydrogeology Forsmark . Site descriptive modelling, SDM-Site Forsmark . SKB Report R-08-95, Swedish Nuclear Fuel and Waste Management Co., Stockholm.

Fox A., La Pointe, P., Hermanson, J., and Öhman, J., 2007. Statistical geological discrete fracture network model. Forsmark modelling stage 2.2. SKB Report R-07-46, Swedish Nuclear Fuel and Waste Management Co., Stockholm.

Geier, J.E., 2005. Groundwater flow and radionuclide transport in fault zones in granitic rock. Ph.D. Thesis, Geosciences Department, Oregon State University, 262 p.

Geier, J. (2008a). Discrete-feature modelling of groundwater flow and solute transport for SR-Can review. SKI Report 2008:11, Swedish Radiation Safety Authority, Stockholm.

Geier, J., 2008b. Discrete Feature Model (DFM) user documentation. SKI Report 2008:57, Swedish Radiation Safety Authority, Stockholm.

Geier, J., 2010a. Discrete-feature model implementation of SDM-Site Forsmark. SSM Report 2010:05, Swedish Radiation Safety Authority, Stockholm.

Geier, J., 2010b. Simplification and refinement of discrete-feature model for Forsmark. SSM project memorandum, SSM 2010/465, March 16, 2010.

Geier, J., 2010c. Alternative fracture network models for Forsmark. SSM project memorandum , SSM 2010/465,April 9, 2010.

Geier, J., 2010d. Evaluation of alternative fracture network models for Forsmark using simulated sampling in surface-based boreholes. SSM project memorandum, SSM 2010/465, May 7, 2010.

Geier, J., 2010e. Deposition-hole utilization for an alternative fracture network model of Forsmark . SSM project memorandum , SSM 2010/465, July 14, 2010.

Geier, J., 2010f. Simulated sampling in repository tunnels to distinguish among alternative fracture network models for Forsmark. SSM project memorandum, SSM 2010/465, July 27, 2010.

Geier, J., 2010g. Flow and transport calculations with updated discrete-feature model of Forsmark. SSM project memorandum, SSM 2010/465, September 12, 2010.

Geier, J., 2010h. Discrete Feature Model (DFM) user documentation Version 2.4.0 , SSM project memorandum, SSM 2010/465.

Hedin, A., 2007. Semi-Analytic Stereological Analysis of Waste Package/Fracture Intersections in a Granitic Rock Nuclear Waste Repository Math Geosci DOI 10.1007/s11004-008-9175-3 , International Association for Mathematical Geology.

Munier, R., 2006. Using observations in deposition tunnels to avoid intersections with critical fractures in deposition holes. SKB Report R-06-54, Swedish Nuclear Fuel and Waste Management Co., Stockholm.

Munier, R., 2010. Full perimeter intersection criteria. Definitions and implementations in SR-Site. SKB Technical Report TR-10-21, Swedish Nuclear Fuel and Waste Management Co., Stockholm.

Olofsson, I., Simeonov, A. Stephens, M., Follin, S., Nilsson, A-C., Röshoff, K., Lindberg, U., Lanaro, F., Fredriksson, A., and Persson, L., 2007. Site descriptive modelling Forsmark, stage 2.2. A fracture domain concept as a basis for the statistical modelling of fractures and minor deformation zones, and interdisciplinary coordination. SKB Report R-07-15, Swedish Nuclear Fuel and Waste Management Co., Stockholm.

SKB, 2006a. Long-term safety for KBS-3 repositories at Forsmark and Laxemar area -- a first evaluation. SKB Technical Report TR-06-09, Swedish Nuclear Fuel and Waste Management Co., Stockholm.

SKB, 2006b. SR-Can Data Report. SKB Technical Report TR-06-25, Swedish Nuclear Fuel and Waste Management Co., Stockholm.

SKB, 2008. Site description of Forsmark at completion of the site investigation phase . SKB Technical Report TR-08-05, Swedish Nuclear Fuel and Waste Management Co., Stockholm.

Snow, D. T., 1969. Anisotropic permeability of fractured media. *Water Resources Research* 5(6):1273-1289.

Stephens M B, Fox A, La Pointe P, Simeonov A, Isaksson H, Hermanson J, Öhman J, 2007. Geology Forsmark. Site descriptive modelling, Forsmark stage 2.2. SKB R-07-45. Svensk Kärnbränslehantering AB.

Stephens M B, Simeonov A, Isaksson H, 2008. Bedrock geology Forsmark, Modelling stage 2.3. Implications for and verification of deterministic geological models based on complementary data. SKB R-08-64, Svensk Kärnbränslehantering AB.

2011:13

The Swedish Radiation Safety Authority has a comprehensive responsibility to ensure that society is safe from the effects of radiation. The Authority works to achieve radiation safety in a number of areas: nuclear power, medical care as well as commercial products and services. The Authority also works to achieve protection from natural radiation and to increase the level of radiation safety internationally.

The Swedish Radiation Safety Authority works proactively and preventively to protect people and the environment from the harmful effects of radiation, now and in the future. The Authority issues regulations and supervises compliance, while also supporting research, providing training and information, and issuing advice. Often, activities involving radiation require licences issued by the Authority. The Swedish Radiation Safety Authority maintains emergency preparedness around the clock with the aim of limiting the aftermath of radiation accidents and the unintentional spreading of radioactive substances. The Authority participates in international co-operation in order to promote radiation safety and finances projects aiming to raise the level of radiation safety in certain Eastern European countries.

The Authority reports to the Ministry of the Environment and has around 270 employees with competencies in the fields of engineering, natural and behavioural sciences, law, economics and communications. We have received quality, environmental and working environment certification.